Master Thesis, s011427

Acoustic radiation in microfluidic systems

Thomas Glasdam Jensen

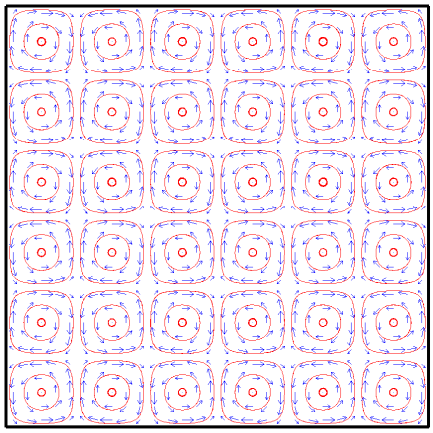

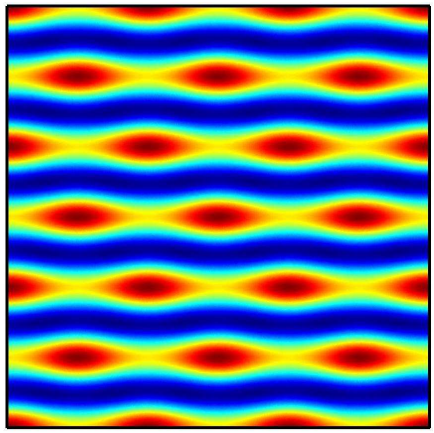

Supervisor: Henrik Bruus

MIC – Department of Micro and Nanotechnology
Technical University of Denmark

2 April 2007

Abstract

As the Lab-On-a-Chip systems becomes increasingly sophisticated, so does the demands to the embedded tools. This is why acoustic manipulation gain increasingly attention around the microfluidic community. Recent research have shown that carefully designed acoustic actuators can be used for both particle handling and mixing. Most research in the micro-acousto-fluidic field is base on trial and error, as no well-developed theory exists in this area.

In this thesis we use perturbation theory to investigate the theory behind the acoustic radiation force, and the equations describing the acoustic streaming flow-patterns. It shows that the absolute amplitude of the acoustic radiation force is difficult to determine. However, the calculated shape of the force corresponds very well to what have been reported by experimentalists. The same thing is the case for the calculated streaming-patterns. The shape of the patterns match the experimental ones very well, but the amplitude becomes several magnitudes larger than physical possible.

Resumé

Efterhånden som Lab-On-a-Chip systemerne bliver mere advancerede, øges kravene til de indbyggede redskaber også. Derfor er interessen for manipulation ved hjælp af akustik stigende i de mikrofluide kredse. Nylig forskning har vist, at man kan bruge nøje designede akustiske resonnatorer til både håndtering af partikler samt til at mixe. Den primære forskning på det mikro-akustik-fluide område er baseret på 'trial and error'-metoden, da der ikke eksisterer nogen fyldestgørende teori på området.

I denne rapport gør vi brug af perturbations teori for at undersøge teorien bag den akustiske strålingskraft og ligningerne, der beskriver de akustiske strømningsmønstre. Det viser sig, at den absolutte størrelse på strålingskraften er svær at finde, men den beregnede form på kraften ligner den, eksperimentalisterne har fundet. Det samme gør sig gældende for de beregnede strømningsmønstre. Formen passer godt med den eksperimentielt fundne, men amplituderne bliver så mange størelsesordner højere, at de ikke længere giver fysisk mening.

Preface

The thesis, hereby presented is titled "Acoustic radiation in microfluidic systems", it has been submitted in order to obtain 50 ECTS points and the Master of Science degree at the Technical University of Denmark (DTU).

This project was carried out within the Microfluidic Theory and Simulation (MIFTS) group at the Department of Micro- and Nanotechnology (MIC), DTU. The thesis was written during the period from April 2006 to April 2007 under supervision by Henrik Bruus and in close collaboration with Ph.D. student Melker Sundin.

The purpose of this work have been to theoretically calculate the acoustic radiation force and the acoustic streaming patterns observed during experiments performed in a earlier course. As this work is the first acoustic-related subject in the MIFTS-group, it has been emphasized to derive the acoustic equations from the bottom, instead of acquiring these from textbooks.

Finally I would like to thank my supervisor Henrik Bruus for his inspiring support and for many fruitful discussions. And secondly, a thank to Melker Sundin for providing the experimental basis, from which this project was inspired. I would also like to thank the entire MIFTS-group for always being able to find a solution to (or way around) any problem encountered.

Thomas Glasdam Jensen
MIC – Department of Micro and Nanotechnology
Technical University of Denmark
2 April 2007

Contents

List of figures **xiv**

List of tables **xv**

List of symbols **xvii**

1 Introduction **1**
1.1 The acoustic radiation force . . . 1
1.2 Acoustic streaming . . . 2
1.3 Experimental background . . . 3
1.3.1 The experimental setup . . . 3
1.3.2 The experimental results . . . 4
1.4 Material parameters . . . 5

2 Periodic motion in incompressible liquids **7**
2.1 Dimensionless equations . . . 7
2.2 Perturbation in P_e for $Re = 0$ . . . 8
2.2.1 Quasi-stationary Stokes flow; $P_e = 0$ . . . 8
2.2.2 Stokes flow; $P_e \neq 0$ . . . 10
2.2.3 Finding the full solution for $Re = 0$; $P_e \neq 0$ . . . 12
2.3 Perturbation in Re . . . 13
2.3.1 The quasi-stationary case, $P_e = 0$ . . . 14
2.3.2 The Navier-Stokes case; $P_e \neq 0$ . . . 17
2.3.3 Solution for $\mathcal{O}(P_e^n)$ and $\mathcal{O}(Re^1)$ . . . 19
2.4 Comparing analytical and numerical solutions . . . 19
2.5 High-order terms . . . 21
2.5.1 Determination of $\mathbf{u}_{1n}$ and p_{1n} . . . 21
2.5.2 Re to second order . . . 23
2.5.3 Determination of $\mathbf{v}_3^{DC}$ . . . 24
2.6 Concluding remarks . . . 25

3 Sound absorption in compressible liquids **27**
3.1 Acoustic perturbation theory . . . 27
3.2 The non-viscous case . . . 28

3.2.1 Zeroth-order perturbation . . . 28
3.2.2 First-order perturbation . . . 28
3.2.3 Second-order perturbation . . . 30
3.3 The viscous case . . . 31
3.3.1 Zeroth-order perturbation . . . 31
3.3.2 First-order perturbation . . . 31
3.3.3 Second-order perturbation . . . 33

4 Planer sound waves **35**
4.1 Wave-emission from an oscillating wall . . . 35
4.2 Wave propagation through a single interface . . . 36
4.3 Wave propagation through multiple interfaces . . . 38
4.4 Acoustic Resonances . . . 41
4.4.1 Unattenuated waves . . . 41
4.4.2 Attenuated waves . . . 42

5 Numerical simulations in COMSOL **43**
5.1 The Acoustic module in COMSOL . . . 43
5.1.1 The eigenfrequency solver . . . 43
5.1.2 Example: Pseudo-one-dimensional . . . 44
5.1.3 The time harmonic solver . . . 49
5.2 General PDE formulation for COMSOL . . . 51
5.3 Executing a COMSOL-script . . . 52

6 The acoustic radiation force **53**
6.1 The force in one dimension . . . 53
6.2 The force in more dimensions . . . 54
6.3 Dimensional analysis; from 3D to 2D . . . 55
6.3.1 Validation of the 2D approximation . . . 55
6.3.2 Density of states . . . 56
6.4 The symmetric chamber model . . . 58
6.5 Breaking of symmetry . . . 60
6.6 Concluding remarks . . . 63

7 Examples of sound absorption in liquids **65**
7.1 Analytic Example 1: plane traveling wave . . . 65
7.1.1 First order pressure, p_1, and velocity u_1 . . . 65
7.1.2 Second order pressure, p_2'', and velocity u_2'' . . . 66
7.2 Analytic Example 2: Wave resonance, 1D . . . 69
7.2.1 First order pressure, p_1, and velocity u_1 . . . 69
7.2.2 Second order pressure, p_2'', and velocity u_2'' . . . 70
7.3 Numeric Example 3: Wave resonance, 2D . . . 73
7.3.1 First order pressure, p_1, and velocity u_1 . . . 73
7.3.2 Second order pressure, p_2'', and velocity $\mathbf{u}_2''$ . . . 75

8 Comparing theory and experiments **79**
8.1 Simulated streaming patterns 79
8.2 Simulated radiation force 81

9 Conclusion **83**

10 Outlook **85**

Appendices **87**

A COMSOL-script; Periodic motion in incompressible liquids **87**

B COMSOL-script; Wave propagation through interfaces **91**

C COMSOL-script; The symmetric chamber model **93**

D COMSOL-script; Numeric Example 3 **95**

List of Figures

1.1 Chip-geometry used in experiments . . . 3
1.2 Chip photo . . . 4
1.3 Experimental results for large particles . . . 4
1.4 Experimental results for small particles . . . 5

2.1 Contour plot of ψ_{qua} . . . 9
2.2 Contour plot of ψ_{sto} . . . 13
2.3 Contour plot of $\psi_{P_e=0}$ . . . 17
2.4 Contour plot of ψ . . . 18
2.5 Plot of AAV, $Re = 10\ P_e$ . . . 20
2.6 Error plot, $Re = 10\ P_e$ . . . 20
2.7 Plot of AAV, $Re = 2\ P_e$ . . . 21
2.8 Error plot, $Re = 2\ P_e$ . . . 21

4.1 A planar wave . . . 36
4.2 A wave passing multiple interfaces . . . 38
4.3 Particle velocity and pressure, on and off-resonance . . . 40

5.1 Pseudo-1D geometry . . . 45
5.2 Mesh for Pseudo-1D geometry . . . 45
5.3 Plot of pressure at eigenfrequency . . . 48
5.4 Numeric validation (resonance) . . . 50
5.5 Errorplot(resonance) . . . 50
5.6 Numeric validation (non-resonance) . . . 51
5.7 Errorplot(non-resonance) . . . 51

6.1 Cell seperation . . . 54
6.2 3D sorted eigenfrequencies . . . 56
6.3 3D sorted eigenfrequencies . . . 56
6.4 Density of states . . . 57
6.5 Analytical density of states . . . 58
6.6 The chamber model geometry . . . 59
6.7 Exampels of eigenmodes . . . 60
6.8 Sketch of asymmetric models . . . 61

6.9 Comparison of asymmetric patterns 62

7.1 Acoustic radiation force - 1D 71
7.2 First order pressure, $\tilde{p}_1$ - 2D 74
7.3 Time averaged first order flux 75
7.4 Divergence of second order velocity, S - 2D 76
7.5 Force density, F_x'' and F_y'' - 2D 77
7.6 Numeric results - 2D 78

8.1 Vortices - 6×6 and 2×2 80
8.2 Acoustic radiation force; vector-plot 81
8.3 Acoustic radiation force; cross-section 82

List of Tables

1.1 Material parameters 6

2.1 Numerical simulation parameters 19

5.1 Domain groups 46
5.2 Boundary groups 47

List of symbols

Symbol	Description	Unit
ρ_0	Mass density	kg m^{-3}
η	Viscosity	Pa s
Y	Young's modulus	GPa
c_s	Speed of Sound	m s^{-1}
$\mathbf{a}_n$	Inward Acceleration	m s^{-2}
ℓ	Piezo amplitude	m
ω	Angular frequency.	rad s^{-1}
λ	Wave length	m
k_0	Wave number	m^{-1}
f	Frequency	Hz
F	Force or Force density	N or N m^{-3}
$\mathbf{u}$	Velocity vector	m s^{-1}
$u,\ v,\ w$	x-, y- and z-velocity component	m s^{-1}
p	Pressure	Pa
ψ	Stream function	m^2 s^{-1}
φ	Flow potential	m^2 s^{-1}
$\mathbf{J}$	Mass-flux	kg m^{-2} s^{-1}
$\mathbf{d}_w$	Displacement; Wall	m
$\mathbf{u}_w$	Velocity; Wall	m s^{-1}
$\mathbf{a}_w$	Acceleration; Wall	m s^{-2}
Z	Acoustic impedance	kg m^{-2} s^{-1}
A_l,B_l,C_l,D_l,	Amplitude of left-going wave in domain A,B,C and D	m^2 s^{-1}
A_r,B_r,C_r,D_r,	Amplitude of right-going wave in domain A,B,C and D	m^2 s^{-1}
i	Imaginary unit	
λ_e	Eigenvalue	
γ	Damping parameter	
$\mathbf{e}_x,\ \mathbf{e}_y,\ \mathbf{e}_z$	Unit vectors	
P_e	Péclet number	
Re	Reynolds number	
$\mathbf{n}$	Normal vector	
ν	Poisson's ratio	

Chapter 1

Introduction

One of the rare instances where the non-linear inertia term $\rho(\mathbf{u}\cdot\boldsymbol{\nabla})\mathbf{u}$ plays a significant role in microfluidics relates to acoustic radiation in liquids. The non-linearity of the term makes the existence of a non-zero time-averaged velocity component possible for a system where harmonically oscillating acoustic waves has been emitted into the liquid. Thus acoustic radiation may be the source of a direct-current liquid flow field[1]. The non-linear term might also result in non-zero time-averaged pressure field, which can be used for particle manipulation. This thesis will study both the flow-patterns induced by an acoustic field, and on the acoustic radiation force affecting any suspended particles.

1.1 The acoustic radiation force

In many μTAS applications there is a need for sorting or separating the input particles. This could for instance be an input consisting of different biological molecules or cells. If the concerning analysis is only to be conducted on one type of particles, then it is sometimes necessary to remove the other particles from the sample. There are several very different methods of separating particles. One of the most obvious methods is the bumper-array[2], which sorts the particles by size. By making a fine grid inside the channels, the larger particles is forced towards a different outlet than the smaller ones. Another way of separating particles is by exploiting that particles with different electrical charge will move with different speed when placed in an electric field. This technique is known as electrophoresis[3, 4, 5]. A third method is dielectrophoresis, which will work on charge neutral particles. Dielectrophoresis works if there is a difference between the dielectric constant of the of a particle and the liquid surrounding it[6, 7]. A fourth separation technique is magnetophoresis, where magnetic micro beads, coated with appropriate antibodies, bind to the targeted particles[8, 9].

The fifth method is by use of the acoustic radiation force. If the density and compressibility of the suspended particles and the surrounding fluid has a given ratio, then it is possible to control the particles. In 1935 L. V. King [10] calculated the acoustic effects on hard circular discs. The theory was further developed by Yosioka and Kawasima[11] in 1955. The theory is however only derived for a planar wave system, and have not been considerably improved since. Hence, to this day scientists[12, 13, 14, 15, 16, 17] must

suffice with the planar wave theory, when explaining their results. During this thesis we shall develop a method for calculating the shape(only relative amplitudes) of the acoustic radiation force in three dimensions. The use of acoustic forces in microfluidic systems is a relatively new idea, and only a few applications have been presented.

The article by H. Li and T. Kenny[17] points out that one of the greater challenges when developing a handheld portable blood diagnosis device, is the separation of the blood constituents. They propose a device based on separation using acoustic radiation as a possible solution.

Another application is presented by Jonsson, H *et al.*[18]. They argue that the embolic load experienced by patients undergoing cardiac surgery, can be greatly reduced by using acoustic radiation to remove lipid particles from the recirculating blood.

One of the expected strengths of these acoustic applications is the ability to handle living cells without harming them.

1.2 Acoustic streaming

In microfluidic systems the flow velocity is often very low and as result thereof the flow becomes laminar. As the word 'laminar' implies, the fluid consists of layers, which almost does not mix. Due to the laminar nature(compared to turbulent) mixing is only caused by diffusion[19]. Even though the length scales in microsystem are very small the diffusion is often too slow to provide sufficient mixing. The easiest way to achieve a good mixing is to make the fluidic channel so long that diffusion has time enough to perform the mixing. The long channels are often constructed in meander-shapes. Of other methods for mixing laminar fluids we can mention oscillatory pumping of either the main inlet/outlet or a secondary pair of inlets [20]. Another method is designing a chamber were the inlets creates an unbalanced driving force, making the liquid swirl around[21, 22]. A slightly more complex method is that of electro-osmotic induced mixing[23], where the oscillating charge on the chamber walls create a non-zero slip velocity. A fifth possibility is to use acoustic streaming. Acoustic streaming is the name of the flow induced in a fluid by an acoustic source.

Acoustic streaming was first described by Lord Rayleigh in the late 1880'ies. It was further developed by C. Eckart[24] in 1947, J. Markham[25] in 1951 and by W. Nyborg[26] in 1952. The results from these three articles have been used as inspiration for developing the equations in Chapter 3. The use of acoustic streaming have been very limited, it has mainly been used for teaching purposes in form of the kundt's tube. Only recently, as the lab-on-chip systems becomes more sophisticated the need of effective mixing has increased and the first applications are being developed.

In December 2005 the EU-funded project SMART-BioMEMS started[27]. The project evolves around testing for generic mutation. During the sample handling, mixing is required. According to plan, the mixing should be achieved by acoustic streaming, induced by a piezo-element.

1.3 Experimental background

In the early spring 2006, I participated in an experimental special-course with the purpose of investigating the acoustic radiation force and acoustic streaming experimentally. The coursed was supervised by Jörg Kutter and Melker Sundin at MIC, DTU. Due to the poor understanding of the experimentally achieved results, I started the work on this Master thesis. Hence, the workload for this thesis has been solely theoretical, all references to experimental work, is refereing to work earlier performed and already credited, or to experimental work performed by Melker Sundin.

1.3.1 The experimental setup

The chip, which was use in the experiments, consists of three layers. The chip is sketched in Fig. 1.1. The lower layer consists of silicon with etched holes for in- and outlet. The middle layer also consists of silicon, in this layer channels have been etched. During the experiments, these channels were filled with water, in which particles were suspended. The upper layer is a pyrex plate. This is used to seal of the channels, while providing optical access. In reality the two lower layers in Fig. 1.1 are actually only one layer. However, to clarify the description these are shown separated. The silicon wafer were 500 μm thick, and the channel were etched to have a depth of 200 μm. Hence, the bottom layer has a thickness of 300 μm, and the middle layer is 200 μm. The top layer has the thickness of a pyrex wafer, 500 μm. The width of the chip is 15 mm and the length is 47.2 mm. The entire length of the channel is 25 mm and the chamber measures 2×2 mm. Notice that the chip depiction in Fig. 1.1 only sketches the geometry, objects are plotted with different length scales. A photo of the real chip is shown in Fig. 1.2

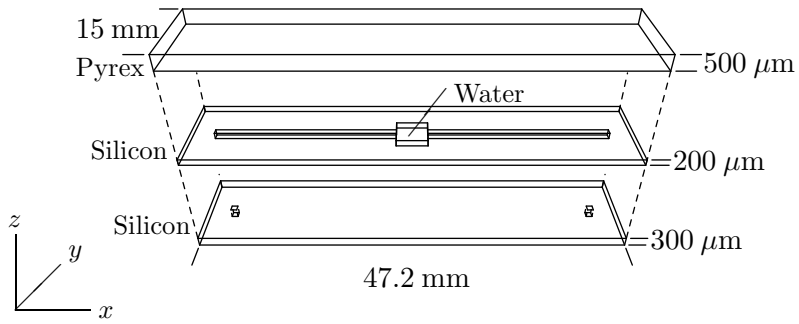

Figure 1.1: The chip layout, divided into three layers.

Experiments were also conducted on a similar chip, but with a round chamber with a diameter of 2 mm. Two different types of particles were used in the experiments. The first kind was polystyrene beads with a diameter of 10 μm, these beads were chosen since they have similar physical properties as red blood cells. The second type of particles were diluted milk containing lipid-particles of approximately 1 μm diameter. When the experiments were conducted, the microscope was located above the chip, looking down

through the pyrex layer, into the chamber. To obtain a view of the entire 2 mm × 2 mm chamber a rather low magnification were used, which resulted in a large depth of field. The large field depth did not allow us to determine the z-position of the particles. Hence, the position is only known in the xy-plane. The acoustic field was induced by placing a piezo-electric crystal against the bottom silicon layer. The piezo-element was about 2 cm wide, Hence the entire chamber was easily covered. The piezo-element was connected to a 10 Volt tone generator, on which the frequency could be tuned.

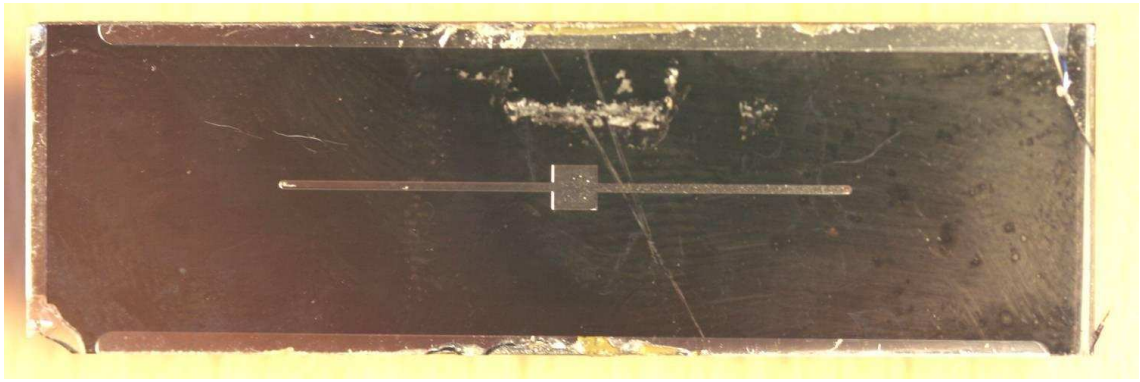

Figure 1.2: This photo shows the chip with the square chamber. Courtesy Melker Sundin.

1.3.2 The experimental results

The experimental results can be divided into two groups, one for large particles ($\approx 10\ \mu$m) and one for small particles ($\approx 1\ \mu$m). The large particles accumulated in specific patterns at different frequencies, see Fig. 1.3.

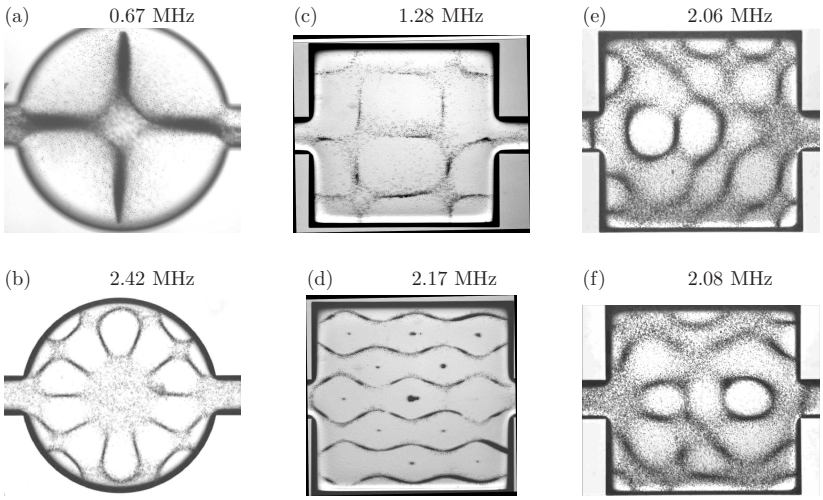

Figure 1.3: The large particles accumulate at specific patterns for different frequencies. Panel (b), (e) and (f) courtesy Melker Sundin.

while the small particles follow the flow-pattern of the fluid.

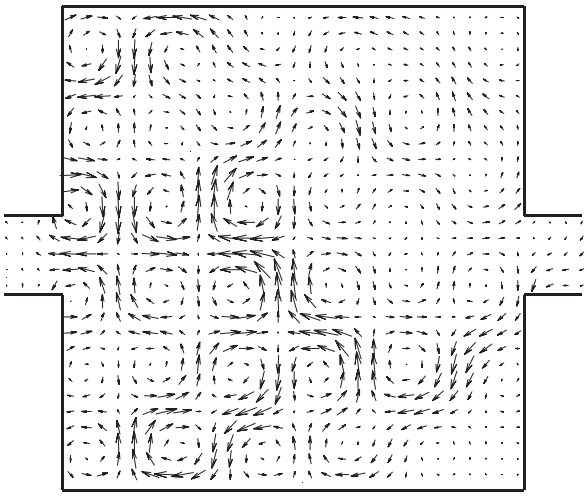

Figure 1.4: A PIV-image, showing the steady state velocity(≈ 0.5 mm/s) of the particles at 2.17 MHz. Courtesy Melker Sundin

We notice that that for the a frequency of 2.17 MHz, we see two different results for particles of different size.

The rest of this thesis will be an attempt to theoretically explain how and why these patterns exists.

1.4 Material parameters

Before we calculate any thing, we are going to need some material parameters. In acoustics the important parameters are the density, ρ_0, and the speed of sound, c_s. In solids the speed of sound has two different definitions. One for objects with dimensions close to the wavelength, and another for larger objects. For small objects c_s is defined as

$$c_s = \sqrt{\frac{Y}{\rho_0}}, \tag{1.1}$$

where Y is Young's modulus. This is the equation we will use when performing calculations on microsystems. The sound velocity for Silicon and PMMA in Table 1.1 is calculated using this. For structures much larger than the wavelength the definition must also include the Poisson's ratio ν. We notice that that for Silicon the Young's modulus is lattice dependant. We shall however assume that Silicon is an isotropic material and hence, use the average modulus instead.

Material		Silicon	Water	Pyrex	Air	PMMA
Density $\left[\frac{\text{kg}}{\text{m}^3}\right]$	ρ_0	$2331^{[a]}$	$998.2^{[a]}$	$2230^{[b]}$	$1.161^{[a]}$	$1190^{[b]}$
Young modulus [GPa]	Y	$168^{[b]}$	-	-	-	$3^{[c]}$
Sound velocity $\left[\frac{\text{m}}{\text{s}}\right]$	c_s	8490	$1483^{[a]}$	$5640^{[a]}$	$343.4^{[a]}$	1588
Acoustic impedance $\left[\times 10^6 \frac{\text{kg}}{\text{m}^2\text{s}}\right]$	Z	19.8	1.48	12.6	0.0004	1.89

Table 1.1: Material parameters @ 20 °C. Notice that Silicon is treated as isotropic. Numbers marked with '$^{[a]}$' originates from [28], those with '$^{[b]}$' is from [29] and the one with '$^{[c]}$' is from [30]. Unmarked values are calculated from the marked ones.

Chapter 2

Periodic motion in incompressible liquids

When describing microfluidic systems containing a water-like liquid, we usually assume that the liquid is incompressible. However, if the liquid is incompressible, sound waves can not be propagated. Our attempt to calculate the acoustic radiation force and acoustic streaming, are therefore limited by our choice of compressibility. In this chapter we investigate the basic properties of an oscillating boundary and its effects on an incompressible liquid. Perhaps the motion of the boundary is enough to account for the experimentally observed phenomenons. In Chapter 3 we look at compressible liquids.

2.1 Dimensionless equations

We consider the half-space $z > 0$ bounded by the xy plane at $z = 0$ and otherwise unbounded. The oscillating motion is assumed generated by applying an AC-voltage of angular frequency ω to an infinite array of equidistant interdigitated, flat electrodes spaced by $\lambda = 2\pi/k$ on top of a piezo-electric crystal. This setup is modeled by the standing-wave slip-boundary condition at $z = 0$ and no-slip at $z = \infty$,

$$\mathbf{u}(x, y, z, t) = (u\,\mathbf{e}_x,\ v\,\mathbf{e}_y,\ w\,\mathbf{e}_z) \tag{2.1a}$$

$$\mathbf{u}(x, y, 0, t) = \mathrm{u}_0 \cos(kx)\, e^{i\omega t}\, \mathbf{e}_x, \tag{2.1b}$$

$$\mathbf{u}(x, y, \infty, t) = \mathbf{0}, \tag{2.1c}$$

where we have used complex notation for the time dependence. Given these boundary conditions, the goal of this chapter is to solve the Navier–Stokes equation (Eq. (2.2)) for an incompressible liquid

$$\rho\big[\partial_t \mathbf{u} + (\mathbf{u}\cdot\boldsymbol{\nabla})\mathbf{u}\big] = \eta\nabla^2\mathbf{u} - \boldsymbol{\nabla}p, \tag{2.2}$$

where $p = p(x, y, z, t)$ is the pressure field.

The system can be characterized by two dimensionless parameters, the Péclet number P_e and the Reynolds number Re, given by

$$P_e \equiv \frac{\rho\omega}{k^2\eta}, \tag{2.3a}$$

$$Re \equiv \frac{\rho \mathrm{u}_0}{k\eta}. \tag{2.3b}$$

If we furthermore introduce the following dimensionless variables denoted by a underline,

$$\mathbf{r} = \frac{1}{k}\underline{\mathbf{r}}, \quad \mathbf{u} = \mathrm{u}_0\underline{\mathbf{u}}, \quad p = (k\eta \mathrm{u}_0)\underline{p}, \quad t = \frac{1}{\omega}\underline{t}, \tag{2.4}$$

the problem, including the incompressible continuity equation, takes the following dimensionless form,

$$P_e\partial_t\mathbf{u} + Re\,(\mathbf{u}\cdot\boldsymbol{\nabla})\mathbf{u} = \nabla^2\mathbf{u} - \boldsymbol{\nabla}p, \tag{2.5a}$$

$$\boldsymbol{\nabla}\cdot\mathbf{u} = 0, \tag{2.5b}$$

$$\mathbf{u}(x, y, 0, t) = \cos(x)\, e^{it}\, \mathbf{e}_x, \tag{2.5c}$$

$$\mathbf{u}(x, y, \infty, t) = \mathbf{0}. \tag{2.5d}$$

Here we have already dropped the underline as we only will use dimensionless variables in the rest of this chapter.

Finally, if we utilize that the translation invariance along the y-axis results in the simple 2D velocity field $\mathbf{u}(\mathbf{r}, t) = \big(u(x, z, t), w(x, z, t)\big)$ we arrive at the final formulation of our problem:

$$\Big[P_e\partial_t + Re\,(u\partial_x + w\partial_z)\Big]\begin{pmatrix} u \\ w \end{pmatrix} = (\partial_x^2 + \partial_z^2)\begin{pmatrix} u \\ w \end{pmatrix} - \begin{pmatrix} \partial_x p \\ \partial_z p \end{pmatrix}, \tag{2.6a}$$

$$\partial_x u + \partial_z w = 0, \tag{2.6b}$$

$$\begin{pmatrix} u(x, 0, t) \\ w(x, 0, t) \end{pmatrix} = \begin{pmatrix} \cos(x)\, e^{it} \\ 0 \end{pmatrix}, \tag{2.6c}$$

$$\begin{pmatrix} u(x, \infty, t) \\ w(x, \infty, t) \end{pmatrix} = \begin{pmatrix} 0 \\ 0 \end{pmatrix}. \tag{2.6d}$$

2.2 Perturbation in P_e for $Re = 0$

2.2.1 Quasi-stationary Stokes flow; $P_e = 0$

The limit of quasi-stationary Stokes flow is particularly simple to solve, as both P_e and Re are zero, and Eq. (2.6a) becomes

$$(\partial_x^2 + \partial_z^2)\begin{pmatrix} u \\ w \end{pmatrix} = \begin{pmatrix} \partial_x p \\ \partial_z p \end{pmatrix}. \tag{2.7}$$

By employing the so-called stream function $\psi(x, z, t)$, related to the velocity field by the expression

$$\begin{pmatrix} u \\ w \end{pmatrix} \equiv \begin{pmatrix} +\partial_z\psi \\ -\partial_x\psi \end{pmatrix}, \tag{2.8}$$

the incompressibility condition $\partial_x u + \partial_z w = 0$ is automatically fulfilled. We also note by taking the divergence of the Stokes equation and utilizing $\boldsymbol{\nabla} \cdot \mathbf{u} = 0$ we find that the pressure fulfills the Laplace equation

$$(\partial_x^2 + \partial_z^2) p = 0. \tag{2.9}$$

To find the solution $\mathbf{u}$ to our problem, we begin by noting that $u(x, 0) = \cos(x)$. This periodic behavior must also be reflected in the pressure, but as p must fulfill the Laplace equation, we are led to guess the following solution $p \propto f(x)\, e^{-z}$. This exponential fall-off, on the other hand, must be reflected back to the behavior of the velocity field away from $z = 0$. Thus, it is reasonable to guess that the stream function must be of the form $\psi_{\text{qua}} \propto \cos(x) e^{-z}$, but to ensure a vanishing z-component of the velocity, we throw in an extra factor z and arrive at

$$\psi_{\text{qua}} = \cos(x)\, z\, e^{-z}. \tag{2.10}$$

Using the definition from Eq. (2.8) we get:

$$\mathbf{u} = \mathbf{u}_{\text{qua}} = \begin{pmatrix} u \\ w \end{pmatrix} = \begin{pmatrix} \cos(x)\,[1 - z]\, e^{-z} \\ \sin(x)\, z\, e^{-z} \end{pmatrix}, \tag{2.11}$$

and also

$$\nabla^2 \mathbf{u}_{\text{qua}} = \begin{pmatrix} 2\, \cos(x)\, e^{-z} \\ -2\, \sin(x)\, e^{-z} \end{pmatrix} = \boldsymbol{\nabla} p. \tag{2.12}$$

From this it can be seen that

$$p = p_{\text{qua}} = 2\, \sin(x)\, e^{-z}. \tag{2.13}$$

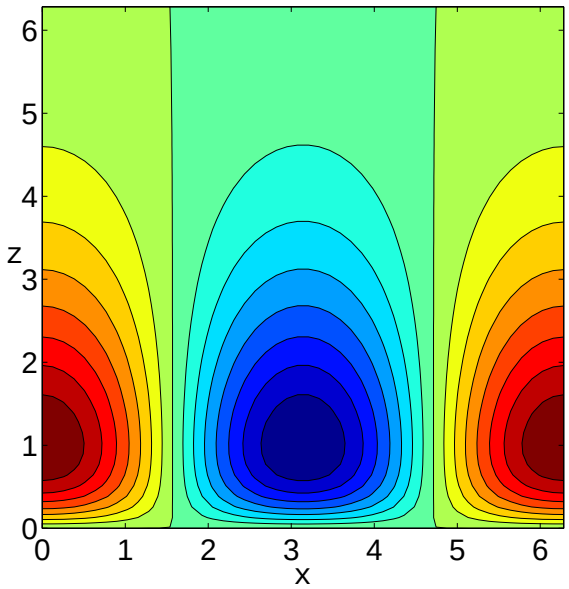

Figure 2.1: Contour plot of ψ_{qua}. It can be seen that a row of rolls are located along the actuating boundary(x=0). We notice that the rolls only stretch $\approx \lambda$ into the liquid. We can see from the gradient of ψ_{qua} that the velocity is highest at the wall.

2.2.2 Stokes flow; $P_e \neq 0$

To solve the problem with $Re = 0$ and $P_e \neq 0$ we use a perturbation method. Because of the oscillating boundary condition both pressure and velocity is expected to be oscillating. Hence, each term in p and $\mathbf{u}$ must be of the form:

$$p(x, z, t) = p(x, z)e^{it} = \tilde{p}\, e^{it}, \tag{2.14a}$$
$$\mathbf{u}(x, z, t) = \mathbf{u}(x, z)e^{it} = \tilde{\mathbf{u}}\, e^{it}, \tag{2.14b}$$

by differentiating $\mathbf{u}$ with time, removing all e^{it}-factors by division Eq. (2.6a) becomes

$$\Big[\big(\partial_x^2 + \partial_z^2\big) - i\, P_e\Big]\tilde{\mathbf{u}} = \boldsymbol{\nabla}\tilde{p}, \tag{2.15}$$

$\tilde{\mathbf{u}}$ and $\tilde{p}$ are spilt up in terms of different order of P_e:

$$\tilde{\mathbf{u}} = \tilde{\mathbf{u}}_0 + P_e\tilde{\mathbf{u}}_1 + P_e^2\tilde{\mathbf{u}}_2 + P_e^3\tilde{\mathbf{u}}_3 + \ldots, \tag{2.16a}$$
$$\tilde{p} = \tilde{p}_0 + P_e\tilde{p}_1 + P_e^2\tilde{p}_2 + P_e^3\tilde{p}_3 + \ldots, \tag{2.16b}$$

and hence, the governing equation becomes

$$\big[\big(\partial_x^2 + \partial_z^2\big) - i\, P_e\big]\Big(\tilde{\mathbf{u}}_0 + P_e\tilde{\mathbf{u}}_1 + P_e^2\tilde{\mathbf{u}}_2 + P_e^3\tilde{\mathbf{u}}_3 + \ldots\Big) = \boldsymbol{\nabla}\Big(\tilde{p}_0 + P_e\tilde{p}_1 + P_e^2\tilde{p}_2 + P_e^3\tilde{p}_3 + \ldots\Big). \tag{2.17}$$

To solve this the equation, it is split into terms of different order of P_e:

$$\mathcal{O}(P_e^0): \quad \nabla^2\tilde{\mathbf{u}}_0 = \boldsymbol{\nabla}\tilde{p}_0, \tag{2.18a}$$
$$\mathcal{O}(P_e^1): \quad \nabla^2\tilde{\mathbf{u}}_1 - i\,\tilde{\mathbf{u}}_0 = \boldsymbol{\nabla}\,\tilde{p}_1, \tag{2.18b}$$
$$\mathcal{O}(P_e^2): \quad \nabla^2\tilde{\mathbf{u}}_2 - i\,\tilde{\mathbf{u}}_1 = \boldsymbol{\nabla}\tilde{p}_2, \tag{2.18c}$$
$$\mathcal{O}(P_e^3): \quad \ldots. \tag{2.18d}$$

These equations can be solved by inserting the results from the first in the second, and so on. The first equation has already been solved in Section 2.2.1. We see that

$$\tilde{\mathbf{u}}_0 = \tilde{\mathbf{u}}_{0,\mathrm{sto}} = \mathbf{u}_{\mathrm{qua}}. \tag{2.19}$$

$$\tilde{p}_0 = \tilde{p}_{0,\mathrm{sto}} = p_{\mathrm{qua}}. \tag{2.20}$$

To find $\tilde{\mathbf{u}}_1$ in the $\mathcal{O}(P_e^1)$ equation, we must first guess a streamfunction. To aid our guess we look at the boundary condition $u(x, 0) = \cos(x)$. Since $u_0(x, 0) = \cos(x)$ then $u_n(x, 0) = 0$. Notice the difference between the zeroth-order velocity in the x-direction, $u_0(x, t)$, and the velocity amplitude of the boundary, u_0. This lead to the streamfunction guess:

$$\psi_n = \cos(x)\, z^{n+1}\, e^{-z}. \tag{2.21}$$

By modifying the definition of the streamfunction to:

$$\begin{pmatrix} \tilde{u}_n \\ \tilde{w}_n \end{pmatrix} \equiv c_n \begin{pmatrix} +\partial_z\psi_n \\ -\partial_x\psi_n \end{pmatrix} \equiv c_n\tilde{\mathbf{v}}_n, \tag{2.22}$$

we get:

$$\tilde{\mathbf{u}}_1 = c_1 \begin{pmatrix} \cos(x)\, e^{-z}\, [2z - z^2] \\ \sin(x)\, e^{-z}\, z^2 \end{pmatrix} = c_1 \tilde{\mathbf{v}}_1. \tag{2.23}$$

Since $\nabla^2 \tilde{\mathbf{u}}_1 = c_1\, \nabla^2 \tilde{\mathbf{v}}_1$, Eq. (2.18b) becomes

$$c_1 \nabla^2 \tilde{\mathbf{v}}_1 - i\, \tilde{\mathbf{u}}_0 = \boldsymbol{\nabla}\, \tilde{p}_1, \tag{2.24}$$

where

$$\nabla^2 \tilde{\mathbf{v}}_1 = \begin{pmatrix} \cos(x)\, e^{-z}\, [4z - 6] \\ \sin(x)\, e^{-z}\, [2 - 4z] \end{pmatrix} = -\boldsymbol{\nabla} \tilde{p}_0 - 4\tilde{\mathbf{u}}_0. \tag{2.25}$$

Hence

$$c_1 \big(\boldsymbol{\nabla} \tilde{p}_0 - 4\tilde{\mathbf{u}}_0\big) - i\, \tilde{\mathbf{u}}_0 = \boldsymbol{\nabla}\, \tilde{p}_1. \tag{2.26}$$

This equation can be fulfilled by setting $c_1 = \frac{-i}{4}$ and $\tilde{p}_1 = c_1\, \tilde{p}_0$. This results in

$$\tilde{\mathbf{u}}_1 = \tilde{\mathbf{u}}_{1,\text{sto}} = \frac{-i}{4} \begin{pmatrix} \cos(x)\, e^{-z}\, [2z - z^2] \\ \sin(x)\, e^{-z}\, z^2 \end{pmatrix}, \tag{2.27a}$$

$$\tilde{p}_1 = \tilde{p}_{1,\text{sto}} = \Big(\frac{-i}{4}\Big) 2\, \sin(x)\, e^{-z}. \tag{2.27b}$$

Next we solve the $\mathcal{O}(P_e^2)$ equation: $\nabla^2 \tilde{\mathbf{u}}_2 - i\, \tilde{\mathbf{u}}_1 = \boldsymbol{\nabla} \tilde{p}_2$. By combining Eq. (2.21) and Eq. (2.22) we get

$$\tilde{\mathbf{u}}_2 = c_2 \begin{pmatrix} \cos(x)\, e^{-z}\, [3z^2 - z^3] \\ \sin(x)\, e^{-z}\, z^3 \end{pmatrix} = c_2 \tilde{\mathbf{v}}_2. \tag{2.28}$$

Since $\nabla^2 \tilde{\mathbf{u}}_2 = c_2\, \nabla^2 \tilde{\mathbf{v}}_2$, Eq. (2.18c) becomes

$$c_2 \nabla^2 \tilde{\mathbf{v}}_2 - i\, \tilde{\mathbf{u}}_1 = \boldsymbol{\nabla}\, \tilde{p}_2. \tag{2.29}$$

We start by looking at $\nabla^2 \tilde{\mathbf{v}}_2$:

$$\nabla^2 \tilde{\mathbf{v}}_2 = \begin{pmatrix} \cos(x)\, e^{-z}\, [6 - 18z + 6z^2] \\ \sin(x)\, e^{-z}\, [6z - 6z^2] \end{pmatrix} = 6\tilde{\mathbf{u}}_0 - 6\tilde{\mathbf{v}}_1 = 6\tilde{\mathbf{u}}_0 - i\, 24\, \tilde{\mathbf{u}}_1, \tag{2.30}$$

so that

$$-i\, 16\, \tilde{\mathbf{u}}_1 = \frac{2}{3} \nabla^2 \tilde{\mathbf{v}}_2 - 4\, \tilde{\mathbf{u}}_0. \tag{2.31}$$

Substituting $4\, \tilde{\mathbf{u}}_0$ using the relation in Eq. (2.25) we get

$$\frac{-i}{4} \boldsymbol{\nabla}\, \tilde{p}_1 = \nabla^2 \Big[-\frac{1}{24} \tilde{\mathbf{v}}_2 - \frac{i}{4} \tilde{\mathbf{u}}_1 \Big] - i\, \tilde{\mathbf{u}}_1. \tag{2.32a}$$

Hence if

$$\tilde{\mathbf{u}}_2 = \tilde{\mathbf{u}}_{2,\text{sto}} = -\frac{1}{24} \tilde{\mathbf{v}}_2 - \frac{i}{4} \tilde{\mathbf{u}}_1, \tag{2.33a}$$

$$\tilde{p}_2 = \tilde{p}_{2,\text{sto}} = \frac{-i}{4}\, \tilde{p}_1 = \frac{1}{16}\, \tilde{p}_0, \tag{2.33b}$$

the equation is fulfilled. So for $Re = 0$ we get the approximate solution

$$\begin{aligned} \tilde{\mathbf{u}}_{\text{sto}} &\approx \tilde{\mathbf{u}}_{0,\text{sto}} + P_e \tilde{\mathbf{u}}_{1,\text{sto}} + P_e^2 \tilde{\mathbf{u}}_{2,\text{sto}} + \mathcal{O}(P_e^3) \\ &\approx e^{-z} \begin{pmatrix} \cos(x) \big[(1 - z) - i \frac{P_e}{4} (2z - z^2) - \frac{P_e^2}{48} (6z + 3z^2 - 2z^3)\big] \\ \sin(x) \big[z - i \frac{P_e}{4} z^2 - \frac{P_e^2}{48} (3z^2 + 2z^3)\big] \end{pmatrix} + \mathcal{O}(P_e^3). \end{aligned} \tag{2.34}$$

2.2.3 Finding the full solution for $Re = 0$; $P_e \neq 0$

The differential equation in Eq. (2.15) can also be solved by guessing the right solution. From the results in Section 2.2.2, we guess that $\tilde{p} = A\,\tilde{p}_0 = 2\,A\,\sin(x)\,e^{-z}$ and that $\psi(x,z) = \cos(x)\,h(z)\,e^{-z}$. Where $h(z)$ is a function to be guessed. By differentiating the streamfunction, ψ we get the velocity

$$\tilde{\mathbf{u}} = \begin{pmatrix} \partial_z\psi \\ -\partial_x\psi \end{pmatrix} = \begin{pmatrix} \cos(x)\,e^{-z}\,[h'(z) - h(z)] \\ \sin(x)\,e^{-z}\,h(z) \end{pmatrix}. \tag{2.35}$$

Inserting $\tilde{\mathbf{u}}$ and $\tilde{p}$ into Eq. (2.15) yields:

$$\begin{gathered} \left[\nabla^2 - iP_e\right]\begin{pmatrix} \cos(x)\,e^{-z}\,[h' - h] \\ \sin(x)\,e^{-z}\,h \end{pmatrix} = \boldsymbol{\nabla}\left[2\,A\,\sin(x)\,e^{-z}\right], \\ \begin{pmatrix} \cos(x)\,e^{-z}\,[2h' - 3h'' + h'''] \\ \sin(x)\,e^{-z}\,[h'' - 2h'] \end{pmatrix} - iP_e\begin{pmatrix} \cos(x)\,e^{-z}\,[h' - h] \\ \sin(x)\,e^{-z}\,h \end{pmatrix} = \begin{pmatrix} 2A\,\cos(x)\,e^{-z} \\ -2A\,\sin(x)\,e^{-z} \end{pmatrix}. \end{gathered} \tag{2.36}$$

This leaves us with the following two equations:

$$2h' - 3h'' + h''' - i\,P_e\,h' + i\,P_e\,h = 2\,A, \tag{2.37a}$$

$$h'' - 2\,h' - i\,P_e\,h = -2\,A. \tag{2.37b}$$

Adding the two equations together gives a third:

$$-2h'' + h''' - i\,P_e\,h' = 0. \tag{2.38}$$

From Eq. (2.38) we can see that one solution could be $h(z) = B$, where B is a constant. However, to fulfill the boundary conditions for $h(z)$, which are found from Eq. (2.6c), Eq. (2.6d) and Eq. (2.35) to be

$$h(0) = 0, \tag{2.39a}$$

$$h'(0) = 1, \tag{2.39b}$$

$$h(\infty) = 0, \tag{2.39c}$$

we guess:

$$h(z) = B(1 - e^{\alpha\,z}). \tag{2.40}$$

Inserting $h(z)$ into Eq. (2.38) gives

$$-[-2\,\alpha^2 + \alpha^3 - i\,P_e\,\alpha]\,B\,e^{\alpha\,z} = 0. \tag{2.41}$$

$B\,e^{\alpha\,z}$ is divided out and the resulting quadratic equation in α has the two solutions

$$\alpha_{\mp} = 1 \mp \sqrt{1 + i\,P_e}. \tag{2.42}$$

using $h(\infty) = 0$ we get $\alpha = \alpha_-$, and from $h'(0) = 1$ we get

$$B = \frac{-1}{\alpha} = \frac{1}{\sqrt{1 + i\,P_e} - 1}. \tag{2.43}$$

All that remain is to determine A. This is done by inserting $h(z)$ into Eq. (2.37b) and solving for A

$$A = \frac{-i\,P_e}{2\alpha} = \frac{i\,P_e}{2(\sqrt{1+i\,P_e}-1)}. \tag{2.44}$$

To summarize we got:

$$\psi_{\text{sto}} = \cos(x)\,e^{-z}\frac{1}{\sqrt{1+iP_e}-1}(1-e^{z-z\sqrt{1+iP_e}}), \tag{2.45a}$$

$$\tilde{\mathbf{u}}_{\text{sto}} = \begin{pmatrix} \cos(x)\frac{\sqrt{1+iP_e}\,e^{-z\sqrt{1+iP_e}}-e^{-z}}{\sqrt{1+iP_e}-1} \\ \sin(x)\frac{e^{-z\sqrt{1+iP_e}}-e^{-z}}{1-\sqrt{1+iP_e}} \end{pmatrix}, \tag{2.45b}$$

$$\tilde{p}_{\text{sto}} = \frac{i\,P_e\,\sin(x)\,e^{-z}}{\sqrt{1+i\,P_e}-1}. \tag{2.45c}$$

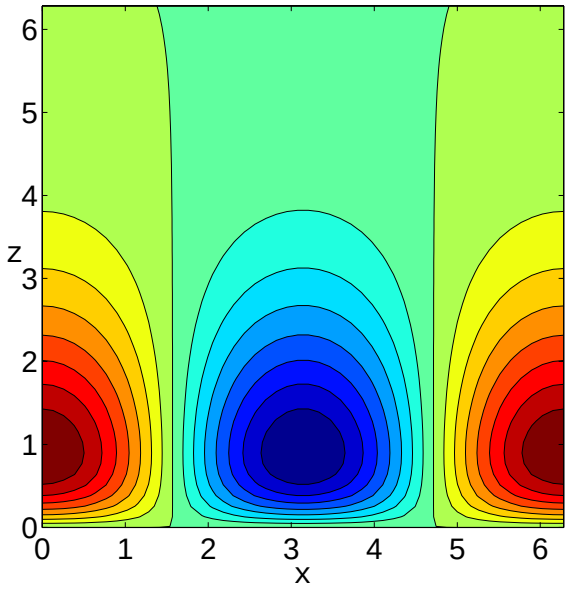

Figure 2.2: Contour plot of ψ_{sto}, where $P_e = 1$. It can be seen that the row of rolls does not stretch as far into the liquid as in the quasi-stationary case.

2.3 Perturbation in Re

To solve Eq. (2.5a) for $P_e \neq 0$ and $Re \neq 0$ we once more use a perturbation method. We begin by rewriting Eq. (2.5a) to

$$\Big[\nabla^2 - P_e\,\partial_t - Re(\mathbf{u}\cdot\boldsymbol{\nabla})\Big]\mathbf{u} = \boldsymbol{\nabla}p, \tag{2.46}$$

where

$$\mathbf{u} = \mathbf{u}_0 + Re\,\mathbf{u}_1 + Re^2\,\mathbf{u}_2 + Re^3\,\mathbf{u}_3 + \ldots, \tag{2.47a}$$

$$\widehat{p} = p_0 + Re\, p_1 + Re^2\, p_2 + Re^3\, p_3 + \dots. \tag{2.47b}$$

Splitting Eq. (2.46) into terms of different order of Re yields

$$\mathcal{O}(Re^0): \quad \left[\nabla^2 - P_e\partial_t\right]\mathbf{u}_0 - \boldsymbol{\nabla} p_0 = 0 \tag{2.48a}$$
$$\mathcal{O}(Re^1): \quad \left[\nabla^2 - P_e\partial_t\right]\mathbf{u}_1 - \boldsymbol{\nabla} p_1 = (\mathbf{u}_0\cdot\boldsymbol{\nabla})\mathbf{u}_0, \tag{2.48b}$$
$$\mathcal{O}(Re^2): \quad \left[\nabla^2 - P_e\partial_t\right]\mathbf{u}_2 - \boldsymbol{\nabla} p_2 = (\mathbf{u}_1\cdot\boldsymbol{\nabla})\mathbf{u}_0 + (\mathbf{u}_0\cdot\boldsymbol{\nabla})\mathbf{u}_1, \tag{2.48c}$$
$$\mathcal{O}(Re^3): \quad \dots. \tag{2.48d}$$

It is recognized that for $P_e \neq 0$ Eq. (2.48a) is the same as Eq. (2.15). Hence we got

$$\tilde{\mathbf{u}}_0 = \tilde{\mathbf{u}}_{\text{sto}} = \begin{pmatrix} \cos(x)\frac{\sqrt{1+iP_e}\, e^{-z\sqrt{1+iP_e}} - e^{-z}}{\sqrt{1+iP_e}-1} \\ \sin(x)\frac{e^{-z\sqrt{1+iP_e}} - e^{-z}}{1-\sqrt{1+iP_e}} \end{pmatrix}, \tag{2.49a}$$

$$\tilde{p}_0 = \tilde{p}_{\text{sto}} = \frac{i\, P_e\, \sin(x)\, e^{-z}}{\sqrt{1+i\, P_e}-1}, \tag{2.49b}$$

and for $P_e = 0$ Eq. (2.48a) is the same as Eq. (2.7), hence,

$$\tilde{\mathbf{u}}_0 = \tilde{\mathbf{u}}_{\text{qua}} = \begin{pmatrix} \cos(x)\,[1-z]\, e^{-z} \\ \sin(x)\, z\, e^{-z} \end{pmatrix}, \tag{2.50a}$$

$$\tilde{p}_0 = \tilde{p}_{\text{qua}} = 2\, \sin(x)\, e^{-z}. \tag{2.50b}$$

2.3.1 The quasi-stationary case, $P_e = 0$

First we solve the equation in $\mathcal{O}(Re^1)$, for $P_e = 0$. Eq. (2.48b) becomes

$$\nabla^2\mathbf{u}_1 - \boldsymbol{\nabla} p_1 = (\mathbf{u}_0\cdot\boldsymbol{\nabla})\mathbf{u}_0, \qquad \text{where } \mathbf{u}_0 = \mathbf{u}_{\text{qua}}. \tag{2.51}$$

Since we assume the system is to be used at high frequencies($\approx$ 1 MHz), we are not interested in the velocities at small time scales and hence, we look at the time-averaged problem, where

$$\langle \dots \rangle_t = \frac{1}{T}\int_0^T \dots \mathrm{d}t. \tag{2.52}$$

$$\langle\nabla^2\mathbf{u}_1\rangle_t - \langle\boldsymbol{\nabla} p_1\rangle_t = \langle(\mathbf{u}_{\text{qua}}\cdot\boldsymbol{\nabla})\mathbf{u}_{\text{qua}}\rangle_t. \tag{2.53}$$

To get rid of artificial real terms, originating from imaginary cross-products, we only use the real part of $\mathbf{u}_{\text{qua}}$, since it appears in a nonlinear term

$$\mathbf{u}_{\text{qua}} \equiv \mathrm{Re}[\tilde{\mathbf{u}}_{\text{qua}} e^{it}] \equiv \mathrm{Re}[\tilde{\mathbf{u}}_{\text{qua}}]\cos(t) - \mathrm{Im}[\tilde{\mathbf{u}}_{\text{qua}}]\sin(t). \tag{2.54}$$

Hence, we got

$$\begin{aligned}(\mathbf{u}_{\text{qua}}\cdot\boldsymbol{\nabla})\mathbf{u}_{\text{qua}} = &\Big(\Big[\mathrm{Re}[\tilde{\mathbf{u}}_{\text{qua}}]\cos(t) - \mathrm{Im}[\tilde{\mathbf{u}}_{\text{qua}}]\sin(t)\Big]\cdot\boldsymbol{\nabla}\Big) \\ &\times \Big[\mathrm{Re}[\tilde{\mathbf{u}}_{\text{qua}}]\cos(t) - \mathrm{Im}[\tilde{\mathbf{u}}_{\text{qua}}]\sin(t)\Big]\end{aligned}$$

$$
\begin{aligned}
&= + (\mathrm{Re}[\tilde{\mathbf{u}}_{\mathrm{qua}}]\cos(t)\cdot\boldsymbol{\nabla})\mathrm{Re}[\tilde{\mathbf{u}}_{\mathrm{qua}}]\cos(t)\\
&\quad - (\mathrm{Re}[\tilde{\mathbf{u}}_{\mathrm{qua}}]\cos(t)\cdot\boldsymbol{\nabla})\mathrm{Im}[\tilde{\mathbf{u}}_{\mathrm{qua}}]\sin(t)\\
&\quad - (\mathrm{Im}[\tilde{\mathbf{u}}_{\mathrm{qua}}]\sin(t)\cdot\boldsymbol{\nabla})\mathrm{Re}[\tilde{\mathbf{u}}_{\mathrm{qua}}]\cos(t)\\
&\quad + (\mathrm{Im}[\tilde{\mathbf{u}}_{\mathrm{qua}}]\sin(t)\cdot\boldsymbol{\nabla})\mathrm{Im}[\tilde{\mathbf{u}}_{\mathrm{qua}}]\sin(t)\\
&= + \cos^2(t)(\mathrm{Re}[\tilde{\mathbf{u}}_{\mathrm{qua}}]\cdot\boldsymbol{\nabla})\mathrm{Re}[\tilde{\mathbf{u}}_{\mathrm{qua}}]\\
&\quad - \cos(t)\sin(t)(\mathrm{Re}[\tilde{\mathbf{u}}_{\mathrm{qua}}]\cdot\boldsymbol{\nabla})\mathrm{Im}[\tilde{\mathbf{u}}_{\mathrm{qua}}]\\
&\quad - \sin(t)\cos(t)(\mathrm{Im}[\tilde{\mathbf{u}}_{\mathrm{qua}}]\cdot\boldsymbol{\nabla})\mathrm{Re}[\tilde{\mathbf{u}}_{\mathrm{qua}}]\\
&\quad + \sin^2(t)(\mathrm{Im}[\tilde{\mathbf{u}}_{\mathrm{qua}}]\cdot\boldsymbol{\nabla})\mathrm{Im}[\tilde{\mathbf{u}}_{\mathrm{qua}}]\\
&= + \frac{\cos(2t)}{2}(\mathrm{Re}[\tilde{\mathbf{u}}_{\mathrm{qua}}]\cdot\boldsymbol{\nabla})\mathrm{Re}[\tilde{\mathbf{u}}_{\mathrm{qua}}]\\
&\quad - \frac{\sin(2t)}{2}(\mathrm{Re}[\tilde{\mathbf{u}}_{\mathrm{qua}}]\cdot\boldsymbol{\nabla})\mathrm{Im}[\tilde{\mathbf{u}}_{\mathrm{qua}}]\\
&\quad - \frac{\sin(2t)}{2}(\mathrm{Im}[\tilde{\mathbf{u}}_{\mathrm{qua}}]\cdot\boldsymbol{\nabla})\mathrm{Re}[\tilde{\mathbf{u}}_{\mathrm{qua}}]\\
&\quad - \frac{\cos(2t)}{2}(\mathrm{Im}[\tilde{\mathbf{u}}_{\mathrm{qua}}]\cdot\boldsymbol{\nabla})\mathrm{Im}[\tilde{\mathbf{u}}_{\mathrm{qua}}]\\
&\quad + \frac{1}{2}(\mathrm{Re}[\tilde{\mathbf{u}}_{\mathrm{qua}}]\cdot\boldsymbol{\nabla})\mathrm{Re}[\tilde{\mathbf{u}}_{\mathrm{qua}}]\\
&\quad + \frac{1}{2}(\mathrm{Im}[\tilde{\mathbf{u}}_{\mathrm{qua}}]\cdot\boldsymbol{\nabla})\mathrm{Im}[\tilde{\mathbf{u}}_{\mathrm{qua}}]
\end{aligned}
\tag{2.55}
$$

when time averaging this we find that

$$
\langle(\mathbf{u}_{\mathrm{qua}}\cdot\boldsymbol{\nabla})\mathbf{u}_{\mathrm{qua}}\rangle_t = \frac{1}{2}\Big[\mathrm{Re}[\tilde{\mathbf{u}}_{\mathrm{qua}}]\cdot\boldsymbol{\nabla}\mathrm{Re}[\tilde{\mathbf{u}}_{\mathrm{qua}}] + \mathrm{Im}[\tilde{\mathbf{u}}_{\mathrm{qua}}]\cdot\boldsymbol{\nabla}\mathrm{Im}[\tilde{\mathbf{u}}_{\mathrm{qua}}]\Big] = \frac{1}{2}\mathrm{Re}\left[(\tilde{\mathbf{u}}_{\mathrm{qua}}\cdot\boldsymbol{\nabla})\tilde{\mathbf{u}}^*_{\mathrm{qua}}\right], \tag{2.56}
$$

where $\tilde{\mathbf{u}}^*_{\mathrm{qua}}$ is the complex conjugate of $\tilde{\mathbf{u}}_{\mathrm{qua}}$.

We assume that the velocity, $\mathbf{u}_1$ and the pressure, p_1 has the following form:

$$
\mathbf{u}_1 = \mathbf{u}_1^{DC} + \sum_{n=1}^{\infty}\mathbf{u}_{1n}, \qquad \text{where } \mathbf{u}_{1n} = \mathbf{a}_{1n}\cos(nt) + \mathbf{b}_{1n}\sin(nt), \tag{2.57a}
$$

$$
p_1 = p_1^{DC} + \sum_{n=1}^{\infty}p_{1n}, \qquad \text{where } p_{1n} = c_{1n}\cos(nt) + d_{1n}\sin(nt). \tag{2.57b}
$$

where the 'DC' indicates a term is independent of time, and can be a source of direct current.

Inserting $\mathbf{u}_1$ and p_1 into Eq. (2.53) it becomes

$$
\nabla^2\mathbf{u}_1^{DC} - \boldsymbol{\nabla}p_1^{DC} = \frac{1}{2}\Big[\mathrm{Re}[\tilde{\mathbf{u}}_{\mathrm{qua}}]\cdot\boldsymbol{\nabla}\mathrm{Re}[\tilde{\mathbf{u}}_{\mathrm{qua}}] + \mathrm{Im}[\tilde{\mathbf{u}}_{\mathrm{qua}}]\cdot\boldsymbol{\nabla}\mathrm{Im}[\tilde{\mathbf{u}}_{\mathrm{qua}}]\Big]. \tag{2.58}
$$

From Eq. (2.11) we se that $\mathrm{Im}[\tilde{\mathbf{u}}_{\mathrm{qua}}] = 0$. Hence we have

$$
\nabla^2\mathbf{u}_1^{DC} - \boldsymbol{\nabla}p_1^{DC} = \frac{1}{2}\Big[(\mathrm{Re}[\tilde{\mathbf{u}}_{\mathrm{qua}}]\cdot\boldsymbol{\nabla})\mathrm{Re}[\tilde{\mathbf{u}}_{\mathrm{qua}}]\Big]. \tag{2.59}
$$

Inserting $\tilde{\mathbf{u}}_0$ from Eq. (2.50a) gives

$$\nabla^2 \mathbf{u}_1^{DC} - \boldsymbol{\nabla} p_1^{DC} = \frac{1}{2}\left[\big(\cos(x) e^{-z}[1-z]\partial_x + \sin(x) e^{-z} z \partial_z \big) \begin{pmatrix} \cos(x)\,[1-z]\,e^{-z} \\ \sin(x)\,z\,e^{-z} \end{pmatrix} \right],$$

$$\nabla^2 \mathbf{u}_1^{DC} - \boldsymbol{\nabla} p_1^{DC} = -\frac{1}{4}\left[\begin{pmatrix} \sin(2x)\,e^{-2z} \\ 2\,[z^2 - z]\,e^{-2z} \end{pmatrix} \right]. \tag{2.60}$$

To solve this equation we guess the form of the streamfunction, ψ and pressure to be a combination of a trigonometric function, an exponential and a polynomial in z.

$$\psi = \sin(2x)\, e^{-2z}\, [A + Bz + Cz^2], \tag{2.61a}$$

$$p_1^{DC} = e^{-2z}\Big[\cos(2x)[D + Fz] + [G + Hz + Jz^2] \Big]. \tag{2.61b}$$

Using the definition of the streamfunction given in Eq. (2.8) gives

$$\mathbf{u}_1^{DC} = \begin{pmatrix} -\,e^{-z} \sin(2x)[2A + 2Cz(z-1) + B(2z-1)] \\ -2\,e^{-z} \cos(2x)[A + Bz + Cz^2] \end{pmatrix} \tag{2.62}$$

From the boundary conditions

$$u_1^{DC}(x, 0) = 0, \tag{2.63a}$$

$$w_1^{DC}(x, 0) = 0. \tag{2.63b}$$

we immediately see that $A = 0$ and $B = 0$. $\mathbf{u}_1^{DC}$ is therefore reduced to

$$\mathbf{u}_1^{DC} = \begin{pmatrix} -\,e^{-z} \sin(2x)[2Cz(z-1)] \\ -2\,e^{-z} \cos(2x)[Cz^2] \end{pmatrix}. \tag{2.64}$$

Inserting $\mathbf{u}_1^{DC}$ and p_1^{DC} into Eq. (2.60) gives the following two equations

$$\frac{1}{4} - 12C + 16Cz = -2D - 2Fz, \tag{2.65a}$$

$$4C - z\left(\frac{1}{2} + 16C\right) + \frac{1}{2}z^2 + \cos^2(x)\big[-8C + z(32C) \big] =$$
$$2D - F - 2G + H + z(2F - 2H + 2J) - 2Jz^2 + \cos^2(x)\big[-4D + 2F - 4Fz \big]. \tag{2.65b}$$

Which can be split into seven new equations:

$$\frac{1}{4} - 12C = -2D \tag{2.66a}$$

$$16C = -2F \tag{2.66b}$$

$$4C = 2D - F - 2G + H \tag{2.66c}$$

$$-\frac{1}{2} - 16C = 2F - 2H + 2J \tag{2.66d}$$

$$\frac{1}{2} = -2J \tag{2.66e}$$

$$-8C = -4D + 2F \tag{2.66f}$$
$$32C = -4F. \tag{2.66g}$$

From these equations we find

$$J = -\frac{1}{4}, \quad C = \frac{1}{64}, \quad F = -\frac{1}{8}, \quad D = -\frac{1}{32}, \quad H = 0, \quad G = 0, \tag{2.67}$$

and hence, we got

$$\psi = \psi_{P_e=0} = \frac{z^2}{64}\sin(2x)\, e^{-2z}, \tag{2.68a}$$
$$\mathbf{u}_1^{DC} = \mathbf{u}_{1,P_e=0}^{DC} = \begin{pmatrix} \sin(2x)\left[\frac{z}{32} - \frac{z^2}{32}\right] \\ -\cos(2x)\,\frac{z^2}{32} \end{pmatrix} e^{-z}, \tag{2.68b}$$
$$p_1^{DC} = p_{P_e=0}^{DC} = -\left[\cos(2x)\left(\frac{1}{32} + \frac{z}{8}\right) + \frac{z^2}{4}\right] e^{-2z}. \tag{2.68c}$$

it is checked that $\mathbf{u}_{1,P_e=0}^{DC}$ and $p_{P_e=0}^{DC}$ given by Eq. (2.68b) and Eq. (2.68c) fulfills Eq. (2.60).

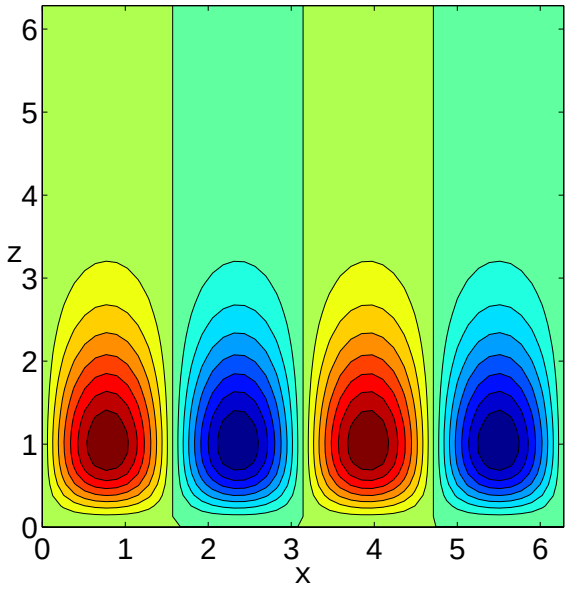

Figure 2.3: Contour plot of $\psi_{P_e=0}$. It can be seen that the number of rolls have doubled. Maximum- and minimum values are only about one percent of those from the quasi stationary and stokes case (≈ 0.01 u_0). We notice that $\partial_z\psi(z=0) = 0$.

2.3.2 The Navier-Stokes case; $P_e \neq 0$

Next we solve Eq. (2.48b) for $P_e \neq 0$. This time we substitute $\mathbf{u}_0$ with $\mathbf{u}_{\text{sto}}$ given by Eq. (2.34). Assuming $\mathbf{u}_1$ and p_1 can be expressed as in Eq. (2.57a) and Eq. (2.57b), and time-averaging the equation we got

$$\nabla^2\mathbf{u}_1^{DC} - \boldsymbol{\nabla} p_1^{DC} = \frac{1}{2}\Big(\text{Re}[\mathbf{u}_{\text{sto}}]\cdot\boldsymbol{\nabla}\text{Re}[\mathbf{u}_{\text{sto}}] + \text{Im}[\mathbf{u}_{\text{sto}}]\cdot\boldsymbol{\nabla}\text{Im}[\mathbf{u}_{\text{sto}}]\Big), \tag{2.69a}$$

$$\nabla^2 \mathbf{u}_1^{DC} - \boldsymbol{\nabla} p_1^{DC} = -\begin{pmatrix} \frac{1}{4}\sin(2x)\, e^{-2z}[1 + \frac{P_e^2}{8}(z^2 - z)] \\ \frac{1}{2}e^{-2z}[(z^2 - z) - \frac{P_e^2}{48}(-9z^2 + 4z^3 + z^4)] \end{pmatrix}, \tag{2.69b}$$

where $\langle P_e \partial_t \mathbf{u} \rangle_t = 0$

When guessing the form of ψ and p_1^{DC}, we try adding a fourth order polynomial to all terms in Eq. (2.68a) and Eq. (2.68c).

$$\psi = \sin(2x)\, e^{-2z}\Big[\frac{z^2}{64} + P_e^2(A_1 + B_1 z + C_1 z^2 + D_1 z^3 + E_1 z^4)\Big], \tag{2.70a}$$

$$\begin{aligned} p_1^{DC} = e^{-2z}\Big[&- \frac{z^2}{4} + P_e^2(A_2 + B_2 z + C_2 z^2 + D_2 z^3 + E_2 z^4) \\ &+ \cos(2x)\Big(- \frac{1}{32} - \frac{z}{8} + P_e^2(A_3 + B_3 z + C_3 z^2 + D_3 z^3 + E_3 z^4)\Big)\Big]. \end{aligned} \tag{2.70b}$$

We find that

$$\psi = \sin(2x)\, e^{-2z}\Big[\frac{z^2}{64} + \frac{P_e^2}{12288}(4z^4 - 8z^3 - 3z^2)\Big], \tag{2.71a}$$

$$p_1^{DC} = e^{-2z}\left[- \frac{z^2}{4} + \frac{P_e^2}{192}(6z^3 + z^4) + \cos(2x)\left(- \frac{1}{32} - \frac{z}{8} + P_e^2\Big[\frac{1}{2048} + \frac{z}{512} + \frac{z^2}{256} - \frac{z^3}{192}\Big]\right)\right]. \tag{2.71b}$$

$$\mathbf{u}_1^{DC} = -e^{-2z}\begin{pmatrix} \sin(2x)\Big[\frac{1}{32}(z^2 - z) + \frac{P_e^2}{6144}(4z^4 - 16z^3 + 9z^2 + 3z)\Big] \\ \cos(2x)\, z^2\Big[\frac{1}{32} + \frac{P_e^2}{6144}(4z^2 - 8z - 3)\Big] \end{pmatrix} + \mathcal{O}(P_e^3) + \mathcal{O}(Re^2). \tag{2.71c}$$

solves Eq. (2.69b).

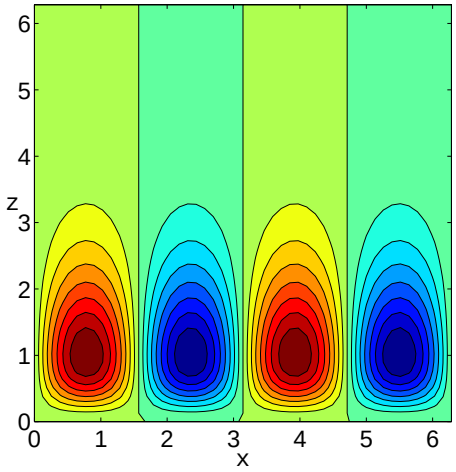

Figure 2.4: Contour plot of ψ, where $P_e = 1$ and $Re = 1$. also here we see that the number of rolls have doubled. Maximum- and minimum values are only about one percent of those from the quasi stationary and stokes case (≈ 0.01 u_0). We notice that $\partial_z \psi(z = 0) = 0$.

2.3.3 Solution for $\mathcal{O}(P_e^n)$ and $\mathcal{O}(Re^1)$

From the results in the two previous subsections we see that a solution to the time averaged Eq. (2.48b)

$$\langle \nabla^2 \mathbf{u}_1 \rangle_t - \langle \boldsymbol{\nabla} p_1 \rangle_t = \langle (\mathbf{u}_0 \cdot \boldsymbol{\nabla}) \mathbf{u}_0 \rangle_t. \tag{2.72}$$

can be found by time averaging

$$\nabla^2 \mathbf{u}_1^{DC} - \boldsymbol{\nabla} p_1^{DC} = \frac{1}{2} \Big(\mathrm{Re}[\tilde{\mathbf{u}}_0] \cdot \boldsymbol{\nabla} \mathrm{Re}[\tilde{\mathbf{u}}_0] + \mathrm{Im}[\tilde{\mathbf{u}}_0] \cdot \boldsymbol{\nabla} \mathrm{Im}[\tilde{\mathbf{u}}_0] \Big). \tag{2.73}$$

and substituting $\tilde{\mathbf{u}}_0$ by an $\mathcal{O}(P_e^n)$ expansion of $\tilde{\mathbf{u}}_{\mathrm{sto}}$ in P_e

$$\tilde{\mathbf{u}}_{\mathrm{sto}} = \begin{pmatrix} \cos(x) \frac{\sqrt{1+iP_e}\, e^{-z\sqrt{1+iP_e}} - e^{-z}}{\sqrt{1+iP_e}-1} \\ \sin(x) \frac{e^{-z\sqrt{1+iP_e}} - e^{-z}}{1-\sqrt{1+iP_e}} \end{pmatrix}, \tag{2.74}$$

and then guessing

$$\mathbf{u}_1^{DC} = \begin{pmatrix} +\partial_x \psi_n \\ -\partial_z \psi_n \end{pmatrix}, \qquad \psi_n = \sin(2x)\, e^{-2z} \sum_{k=0,2,4\ldots}^{n} \Big(P_e^k \sum_{m=2\ldots}^{k+2} \Big[a_{km}\, z^m \Big] \Big) \tag{2.75a}$$

$$p_1^{DC} = e^{-2z} \Bigg[b\, z^2 + \sum_{k=2,4\ldots}^{n} \Big(P_e^k \sum_{l=3\ldots}^{k+2} \Big[c_{kl}\, z^l \Big] \Big) + \cos(2x) \sum_{k=0,2,4\ldots}^{n} \Big(P_e^k \sum_{h=0\ldots}^{k+1} \Big[d_{kh}\, z^h \Big] \Big) \Bigg]. \tag{2.75b}$$

If these guesses are inserted into Eq. (2.73), we get two equations with a total of 4, 13, 28, 49, 76, 109 unknown constants for n=0, 2, 4, 6, 8, 10, respectively .

2.4 Comparing analytical and numerical solutions

When comparing solutions, we need to establish a specific property which we want to compare. In this section we have chosen to look at the average value of the absolute velocity, computed in an square area adjacent to the channel wall with the same width as the pitch between the piezo elements. The numerical calculation is performed with dimensions and the following values:

symbol	value	unit	description
P_π	$2\pi \times 10^{-6}$	m	Piezo pitch
ρ	1000	$\mathrm{kg\,m^{-3}}$	Fluid density
η	1×10^{-3}	Pa s	Fluid viscosity
P_e	to be chosen	–	Péclet number
s	to be chosen, $s > 1$	–	Constant
Re	$s \times P_e$	–	Reynolds number
ω	$P_e \times 10^6$	$\mathrm{s^{-1}}$	Angular frequency
u_0	$s \times P_e$	$\mathrm{m\,s^{-1}}$	Slip velocity

Table 2.1: The values used for the numerical simulation(see Appendix A).

By defining our values like this, we can choose any value of P_e and Re and we still fulfill the definitions from Eq. (2.3a) and Eq. (2.3b). In order to justify our time averaging method we must require that $Re > P_e$. Hence, we set $Re = s \times P_e$, where s is a constant larger than 1. For different values of P_e we then compute the Average Absolute Velocity, AAV

$$AAV = \frac{\int_\Omega |\mathbf{u}| \, \mathrm{d}x \, \mathrm{d}z}{P_\pi^2} \tag{2.76}$$

In Fig. 2.5 and Fig. 2.7 the AAV is plotted for increasing values of P_e for different $\mathcal{O}(P_e^n)$-expansions. To estimate how well these expansions correspond to the numeric result, we define the error,

$$Error = \frac{|AAV_{\mathcal{O}(P_e^n)} - AAV_{num}|}{AAV_{num}} \times 100\,\% \tag{2.77}$$

The error is plotted in Fig. 2.6 and Fig. 2.8.

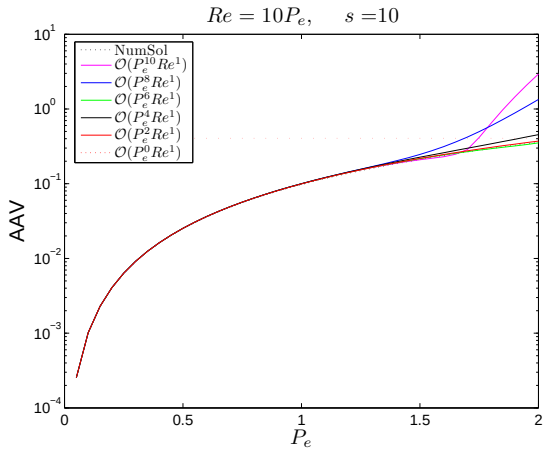

Figure 2.5: A plot of the Average Absolute Velocity, AAV. Plotted for different expansions. For $P_e < 1.5$ the analytical results is very close to the numerical Solution(NumSol).

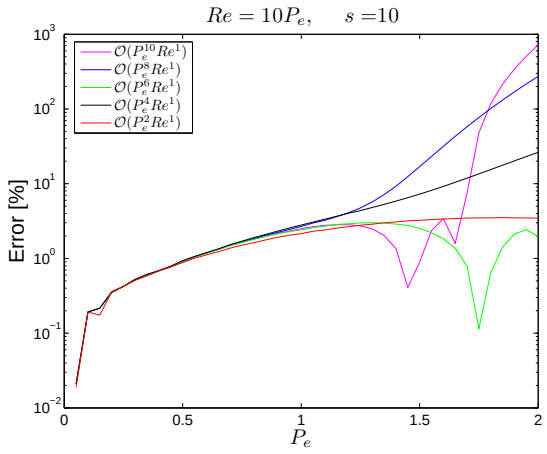

Figure 2.6: A plot of the error. Plotted for different expansions. The fluctuations for $\mathcal{O}(P_e^6 Re^1)$ and $\mathcal{O}(P_e^{10} Re^1)$ are caused by the sign change in the difference.

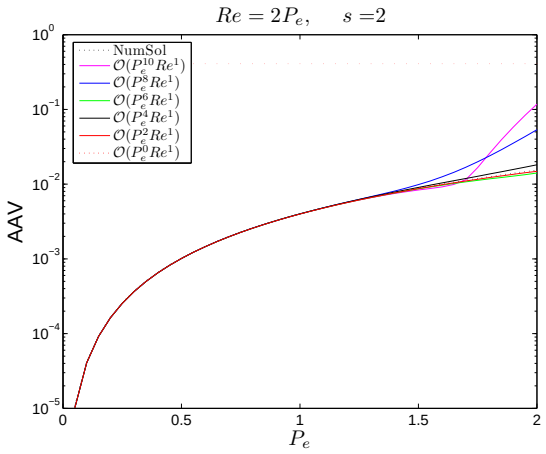

Figure 2.7: A plot of the Average Absolute Velocity, AAV. Plotted for different expansions. Again we see that for $P_e < 1.5$ the analytical results is very close to the numerical Solution(NumSol). Notice that NumSol-values under 10^{-4} are uncertain, since the simulations were conducted with a absolute tolerance of 10^{-4}.

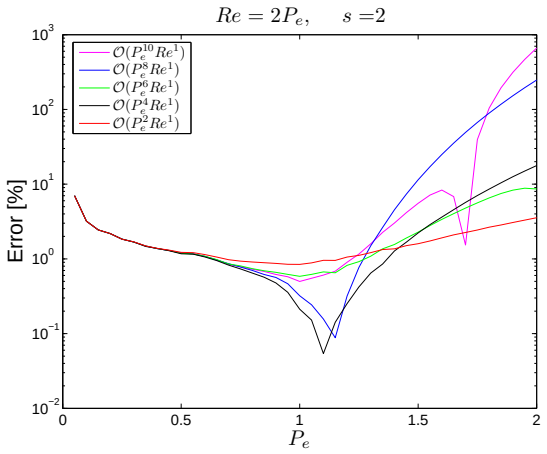

Figure 2.8: A plot of the error. Plotted for different expansions. It can be seen that the error is especially large for small values of P_e, this is a result of comparing very small unprecise numbers.

From Fig. 2.6 and Fig. 2.8 it can be seen that all the analytic solutions are valid for $P_e < 1.2$. For $P_e > 1.2$ it is only $\mathcal{O}(P_e^2 Re^1)$ and $\mathcal{O}(P_e^6 Re^1)$ that are accurate, and still these are only accurate until $P_e \approx 2$. This show, as expected, that the perturbation theory becomes invalid, for large parameters. Increased accuracy might be achieved by calculating higher orders in Re. We attempt to do so in the following section.

2.5 High-order terms

Before we can calculate the second-order terms, we must first calculate the remaining first-order terms.

2.5.1 Determination of $\mathbf{u}_{1n}$ and p_{1n}

To find $\mathbf{u}_{1n}$ and p_{1n} we insert Eq. (2.57a) into Eq. (2.48b)

$$\left[\nabla^2 - P_e\partial_t\right]\left(\mathbf{u}_1^{DC} + \sum_{n=1}^{\infty}\mathbf{u}_{1n}\right) - \boldsymbol{\nabla}\left(p_1^{DC} + \sum_{n=1}^{\infty}p_{1n}\right) = (\mathbf{u}_0\cdot\boldsymbol{\nabla})\mathbf{u}_0, \tag{2.78}$$

After separating known terms from unknown we get:

$$\left[\nabla^2 - P_e\partial_t\right]\sum_{n=1}^{\infty}\mathbf{u}_{1n} - \boldsymbol{\nabla}\sum_{n=1}^{\infty}p_{1n} = (\mathbf{u}_0\cdot\boldsymbol{\nabla})\mathbf{u}_0 + \boldsymbol{\nabla}p_1^{DC} - \boldsymbol{\nabla}^2\mathbf{u}_1^{DC}. \tag{2.79}$$

Inserting $\mathbf{u}_0$, $\mathbf{u}_1^{DC}$ and p_1^{DC} of order $\mathcal{O}(P_e^2)$ we get:

$$\big[\nabla^2 - P_e\partial_t\big]\sum_{n=1}^{\infty}\mathbf{u}_{1n} - \boldsymbol{\nabla}\sum_{n=1}^{\infty}p_{1n} = \begin{pmatrix} K_x \\ K_z \end{pmatrix} \tag{2.80}$$

where

$$K_x = -\frac{e^{-2z}\sin(2x)}{1536}\left(\Big[384 - 48P_e^2 z(1+z)\Big]\cos(2t) + 192P_e z\sin(2t)\right) \tag{2.81a}$$

$$K_z = -\frac{e^{-2z}}{4608}\left(\Big[-2304z + 144(16z^2 + 3z^2P_e^2) + 384P_e^2z^3 - 336P_e^2z^4\Big]\cos(2t) - 48P_e(36z^2 - 24z^3)\sin(2t)\right) \tag{2.81b}$$

When looking at the terms in Eq. (2.81a) and Eq. (2.81b) we immediately see that there are only terms proportional to $\sin(2t)$ or $\cos(2t)$. Since all operators on the left hand side of Eq. (2.80) are linear with respect to time, t, we can conclude that

$$\sum_{n=1}^{\infty}\mathbf{u}_{1n} = \mathbf{u}_{12}, \qquad \sum_{n=1}^{\infty}p_{1n} = p_{12}. \tag{2.82}$$

Hence, the equation to be solved becomes

$$\big[\nabla^2 - P_e\partial_t\big]\mathbf{u}_{12} - \boldsymbol{\nabla}p_{12} = \begin{pmatrix} K_x \\ K_z \end{pmatrix} \tag{2.83}$$

we find that

$$\psi_{12} = e^{-2z}\sin(2x)\left(P_e\left[\frac{z^2}{512} + \frac{z^3}{192}\right]\sin(2t) + \left[\frac{z^2}{64} + P_e^2\left(-\frac{z^2}{2048} - \frac{5z^3}{3072} - \frac{z^4}{1024}\right)\right]\cos(2t)\right) \tag{2.84}$$

$$u_{12} = \frac{e^{-2z}}{3072}\left[\Big[96(z-z^2) - P_e^2(3z + 12z^2 + 2z^3 - 6z^4)\Big]\cos(2t) + 4\,P_e(3z + 9z^2 - 8z^3)\sin(2t)\right]\sin(2x) \tag{2.85}$$

$$w_{12} = \frac{e^{-2z}}{3072}\left[\big[-96z^2 + P_e^2z^2(3 + 10z + 6z^2)\big]\cos(2t) - 4\,P_ez^2(3+8z)\sin(2t)\right]\cos(2x) \tag{2.86}$$

$$p_{12} = e^{-2z}\left(\left[-\frac{z^2}{4} + P_e^2\left(\frac{z^3}{32} + \frac{7z^4}{192}\right)\right.\right.$$

$$+\left[-\frac{1}{32}-\frac{z}{8}+P_e^2\left(\frac{1}{512}+\frac{3z}{512}+\frac{3z^2}{256}+\frac{z^3}{192}\right)\right]\cos(2x)\Bigg]\cos(2t)$$
$$+\left[-\frac{P_e\,z^3}{8}-P_e\left(\frac{1}{253}+\frac{z}{64}+\frac{z^2}{32}\right)\cos(2x)\right]\sin(2t)\Bigg) \tag{2.87}$$

solves Eq. (2.83)

2.5.2 Re to second order

After finding the full solution to $\mathbf{u}_1$ and p_1 we can begin to look at the second order equation Eq. (2.48c). To find $\mathbf{u}_2^{DC}$ we start with Eq. (2.48c)

$$\mathcal{O}(Re^2): \quad \left[\nabla^2 - P_e\partial_t\right]\mathbf{u}_2 - \boldsymbol{\nabla}p_2 = (\mathbf{u}_1\cdot\boldsymbol{\nabla})\mathbf{u}_0 + (\mathbf{u}_0\cdot\boldsymbol{\nabla})\mathbf{u}_1. \tag{2.88}$$

We start by looking at the term $(\mathbf{u}_1\cdot\boldsymbol{\nabla})\mathbf{u}_0$

$$(\mathbf{u}_1\cdot\boldsymbol{\nabla})\mathbf{u}_0 = \sum_{n=0}^{\infty}\left(u_{1n}\partial_x + w_{1n}\partial_z\right)\left(\mathrm{Re}[\tilde{\mathbf{u}}_0]\cos(t) - \mathrm{Im}[\tilde{\mathbf{u}}_0]\sin(t)\right). \tag{2.89}$$

When time averaging these terms we get

$$\begin{aligned}
&n=0, && \langle(\mathbf{u}_1^{DC}\cdot\boldsymbol{\nabla})\mathbf{u}_0\rangle_t = 0\\
&n=1, && \langle(\mathbf{u}_{11}\cdot\boldsymbol{\nabla})\mathbf{u}_0\rangle_t = \frac{1}{2}\Big(a_{11x}\partial_x\mathrm{Re}[\tilde{\mathbf{u}}_0] + a_{11z}\partial_z\mathrm{Re}[\tilde{\mathbf{u}}_0]\Big) - \frac{1}{2}\Big(b_{11x}\partial_x\mathrm{Im}[\tilde{\mathbf{u}}_0] + b_{11z}\partial_z\mathrm{Im}[\tilde{\mathbf{u}}_0]\Big) = 0\\
&n>1, && \langle(\mathbf{u}_{1n}\cdot\boldsymbol{\nabla})\mathbf{u}_0\rangle_t = 0.
\end{aligned} \tag{2.90}$$

Since $\mathbf{a}_1 = 0$ and $\mathbf{b}_1 = 0$ according to Eq. (2.82)

Hence $\langle(\mathbf{u}_1\cdot\boldsymbol{\nabla})\mathbf{u}_0\rangle_t = 0$. Next we look at the term $(\mathbf{u}_0\cdot\boldsymbol{\nabla})\mathbf{u}_1$

$$(\mathbf{u}_0\cdot\boldsymbol{\nabla})\mathbf{u}_1 = \left(\mathrm{Re}[\tilde{u}_0]\cos(t)\partial_x - \mathrm{Im}[\tilde{u}_0]\sin(t)\partial_x + \mathrm{Re}[\tilde{w}_0]\cos(t)\partial_z - \mathrm{Im}[\tilde{w}_0]\sin(t)\partial_z\right)\sum_{n=0}^{\infty}\mathbf{u}_{1n} \tag{2.91}$$

When time averaging these terms we get

$$\begin{aligned}
&n=0, && \langle(\mathbf{u}_0\cdot\boldsymbol{\nabla})\mathbf{u}_1^{DC}\rangle_t = 0\\
&n=1, && \langle(\mathbf{u}_0\cdot\boldsymbol{\nabla})\mathbf{u}_{11}\rangle_t = \frac{1}{2}\Big(\mathrm{Re}[\tilde{u}_0]\partial_x\mathbf{a}_{11} + \mathrm{Re}[\tilde{w}_0]\partial_z\mathbf{a}_{11}\Big) - \frac{1}{2}\Big(\mathrm{Im}[\tilde{u}_0]\partial_x\mathbf{b}_{11} + \mathrm{Im}[\tilde{w}_0]\partial_z\mathbf{b}_{11}\Big) = 0\\
&n>1, && \langle(\mathbf{u}_0\cdot\boldsymbol{\nabla})\mathbf{u}_{1n}\rangle_t = 0.
\end{aligned} \tag{2.92}$$

Hence $(\mathbf{u}_0\cdot\boldsymbol{\nabla})\mathbf{u}_1 = 0$. Finally we look at the time average of the entire equation.

$$\langle\mathcal{O}(Re^2)\rangle_t = \nabla^2\mathbf{u}_2^{DC} - \boldsymbol{\nabla}p_2^{DC} = 0 \tag{2.93}$$

It is obvious that $\mathbf{u}_2^{DC} = \mathbf{0}$ and $p_2^{DC} = \mathbf{0}$ fulfill Eq. (2.93). However, this result does not help to increase the precision of $\mathbf{u}^{DC}$. Hence, we must attempt to calculate $\mathbf{u}_3^{DC}$

2.5.3 Determination of $\mathbf{v}_3^{DC}$

Before we can calculate $\mathbf{u}_3^{DC}$, we need to find $\mathbf{u}_{2n}$ and p_{2n}. We use the same approach as in Section 2.5.1, we insert the Fourier series for $\mathbf{u}_2$ and p_2

$$\left[\nabla^2 - P_e\partial_t\right]\left(\mathbf{u}_2^{DC} + \sum_{n=1}^{\infty}\mathbf{u}_{2n}\right) - \boldsymbol{\nabla}\left(p_2^{DC} + \sum_{n=1}^{\infty}p_{2n}\right) = (\mathbf{u}_1\cdot\boldsymbol{\nabla})\mathbf{u}_0 + (\mathbf{u}_0\cdot\boldsymbol{\nabla})\mathbf{u}_1, \tag{2.94}$$

Inserting $\mathbf{u}_0$, $\mathbf{u}_1$ of order $\mathcal{O}(P_e^2)$ and removing terms with $\mathbf{u}_2^{DC}$ and p_2^{DC} we get:

$$\left[\nabla^2 - P_e\partial_t\right]\sum_{n=1}^{\infty}\mathbf{u}_{2n} - \boldsymbol{\nabla}\sum_{n=1}^{\infty}p_{2n} = \begin{pmatrix} G_x \\ G_z \end{pmatrix} \tag{2.95}$$

where

$$\begin{aligned}
G_x = -\frac{e^{-3z}z}{6144}\Big(&\cos(t)\Big[\big(-288+576z-288z^2+P_e^2[6+36z-95z^2+34z^3+6z^4]\big)\cos(x)\\
&\quad+\big[-288+P_e^2(6+36z-7z^2-9z^3)\big]\cos(3x)\Big]\\
&+\sin(t)\Big[P_e(-12-60z+128z^2-56z^3)\cos(x)\\
&\quad+P_e(-12-60z+4z^2)\cos(3x)\Big]\\
&+\cos(3t)\Big[\big(-96+192z-96z^2+P_e^2[3+21z-7z^2-34z^3+18z^4]\big)\cos(x)\\
&\quad+\big[-96+P_e^2(3+21z+18z^2-3z^3)\big]\cos(3x)\Big]\\
&+\sin(3t)\Big[P_e(-12-60z+128z^2-56z^3)\cos(x)\\
&\quad+P_e(-12-60z+4z^2)\cos(3x)\Big]\Big)
\end{aligned} \tag{2.96a}$$

$$\begin{aligned}
G_z = -\frac{e^{-3z}z^2}{6144}\Big(&\cos(t)\Big[\big(864-864z+P_e^2[-18-117z+60z^2+18z^3]\big)\sin(x)\\
&\quad+P_e^2(-3z-9z^2)\sin(3x)\Big]\\
&+\sin(t)\Big[P_e(36+192z-168z^2)\sin(x)\\
&\quad+4\,P_e z\sin(3x)\Big]\\
&+\cos(3t)\Big[\big(288-288z+P_e^2[-9-69z-36z^2+54z^3]\big)\sin(x)\\
&\quad+P_e^2(-2z-3z^2)\sin(3x)\Big]\\
&+\sin(3t)\Big[P_e(36+192z-168z^2)\sin(x)\\
&\quad+4\,P_e z\sin(3x)\Big]\Big)
\end{aligned} \tag{2.96b}$$

When looking at the terms in Eq. (2.96a) and Eq. (2.96b) we immediately see that there are only terms proportional to $\cos(t)$, $\sin(t)$, $\cos(3t)$ and $\sin(3t)$. Hence, we conclude that

$$\sum_{n=1}^{\infty} \mathbf{u}_{2n} = \mathbf{u}_{21} + \mathbf{u}_{23}, \qquad \sum_{n=1}^{\infty} p_{2n} = p_{21} + p_{23}. \tag{2.97}$$

Hence, the equation to be solved becomes

$$\left[\nabla^2 - P_e\partial_t\right](\mathbf{u}_{21} + \mathbf{u}_{23}) - \boldsymbol{\nabla}(p_{21} + p_{23}) = \begin{pmatrix} G_x \\ G_z \end{pmatrix}. \tag{2.98}$$

Fortunately this equation can be split up into two simpler equations

$$\left[\nabla^2 - P_e\partial_t\right]\mathbf{u}_{21} - \boldsymbol{\nabla}p_{21} = \begin{pmatrix} G_x \propto \left[\sin(t) \vee \cos(t)\right] \\ G_z \propto \left[\sin(t) \vee \cos(t)\right] \end{pmatrix}, \tag{2.99a}$$

$$\left[\nabla^2 - P_e\partial_t\right]\mathbf{u}_{23} - \boldsymbol{\nabla}p_{23} = \begin{pmatrix} G_x \propto \left[\sin(3t) \vee \cos(3t)\right] \\ G_z \propto \left[\sin(3t) \vee \cos(3t)\right] \end{pmatrix}. \tag{2.99b}$$

where $G_x \propto \left[\sin(t) \vee \cos(t)\right]$ means the terms in G_x which depends on either $\sin(t)$ or $\cos(t)$. Unfortunately these two equations becomes rather cumbersome and since the contribution from $\mathbf{u}_3^{DC}$ to $\mathbf{u}^{DC}$ is very small we will not attempt to solve them. In a real physical setup we cannot choose the value of u_0 as freely as done in Section 2.4. u_0 will be given by the product of the frequency and the amplitude of the piezo oscillations, A_π. Hence, if the frequency is 1 MHz and A_π is 1 nm, then $\mathrm{u}_0 = 1 \times 10^{-3}$ m/s. This means that for a water filled system with $k = \frac{2\pi}{10\,\mu\mathrm{m}}$ we have a Reynolds number, $Re = 0.01$. Remembering the pre-factor to $\mathbf{u}_3^{DC}$ is $Re^3 = 10^{-6}$, it is clear that $\mathbf{u}_3^{DC}$ is of less importance. Therefore we must settle with the results from Section 2.4.

2.6 Concluding remarks

Even though the results from Section 2.4 becomes unprecise for large parameters(as the perturbation-method breaks down), they are sufficient to reveal that an oscillating boundary alone, only effects the very nearest part of the incompressible liquid and that the induced motion dies very rapidly as the distance to the wall becomes larger. Hence, we can not explain the acoustic radiation force and acoustic streaming patterns far from the boundary. We are forced to discard the incompressible-liquid-model.

Chapter 3

Sound absorption in compressible liquids

As it has been shown in Chapter 2 we cannot explain the effects of streaming and focusing, simply by an incompressible liquid surrounded by oscillating walls. So in our next attempt we will treat the liquid as compressible, and under the influence of sound waves.

3.1 Acoustic perturbation theory

To describe the absorption of sound in a compressible liquid in the domain Ω, we need the three fundamental equations; the continuity equation (Eq. (3.1)), the Navier-Stokes equation (Eq. (3.2)), and an equation of state (Eq. (3.3)).

$$\partial_t \rho + \boldsymbol{\nabla}\cdot(\rho \mathbf{u}) = 0, \qquad \mathbf{u} \equiv (u\mathbf{e}_x,\ v\mathbf{e}_y,\ w\mathbf{e}_z) \tag{3.1}$$

$$\rho\big[\partial_t \mathbf{u} + (\mathbf{u}\cdot\boldsymbol{\nabla})\mathbf{u}\big] = -\boldsymbol{\nabla} p + \eta\nabla^2\mathbf{u} + \beta\eta\boldsymbol{\nabla}\Big(\boldsymbol{\nabla}\cdot\mathbf{u}\Big), \tag{3.2}$$

$$p = f(\rho). \tag{3.3}$$

where

$$\beta \equiv \frac{1}{3} + \frac{\zeta}{\eta}. \tag{3.4}$$

According to Stoke's viscosity relation $\zeta = 4\eta/3$ [31], the numerical value of β is therefore $\beta = 5/3$. We notice that for compressible fluids the normal no-slip boundary condition changes from velocity $\mathbf{u}(\partial\Omega)$ to flux $\mathbf{J}(\partial\Omega)$

$$\mathbf{u}(\partial\Omega, t) = \mathbf{0} \qquad \Longrightarrow \qquad \mathbf{J}(\partial\Omega, t) = \mathbf{0}. \tag{3.5}$$

Since velocities and fluctuations are expected to be small we assume the following approximations to be valid.

$$p = p_0 + p_1 + p_2 + \ \ldots, \tag{3.6a}$$
$$\rho = \rho_0 + \rho_1 + \rho_2 + \ \ldots, \tag{3.6b}$$
$$\mathbf{u} = 0 \ + \mathbf{u}_1 + \mathbf{u}_2 + \ldots\ . \tag{3.6c}$$

Where the subscript indicates the order of the term. The EOS is found from the expansion

$$p(\rho_0 + [\rho_1 + \rho_2]) = p(\rho_0) + \frac{\partial p}{\partial \rho}(\rho_1 + \rho_2) + \frac{\partial^2 p}{\partial \rho^2}(\rho_1 + \rho_2)^2 \dots \tag{3.7}$$

where

$$c_0^2 \equiv \frac{\partial p}{\partial \rho} \tag{3.8}$$

and to reduce the complexity of the equations, we assume that

$$\frac{\partial^2 p}{\partial \rho^2} = 0. \tag{3.9}$$

3.2 The non-viscous case

To reduce the complexity of the equations we assume that $\eta = 0$ and $\zeta = 0$.

3.2.1 Zeroth-order perturbation

The zeroth-order equations becomes

$$\partial_t \rho_0 = 0, \tag{3.10}$$

$$\boldsymbol{\nabla} p_0 = 0, \tag{3.11}$$

$$p_0 = p(\rho_0). \tag{3.12}$$

From Eq. (3.12) we see that p_0 is a function of ρ_0. Hence from Eqs. (3.10) and (3.11) it can be seen that ρ_0 as well as p_0 is constant in both time and space. ρ_0 and p_0 can be thought of as the equilibrium or background density and pressure when no sound field is present. Notice, we have in Eq. (3.6c) already assumed the velocity to be zero when no sound field is present.

3.2.2 First-order perturbation

The first-order equations becomes

$$\partial_t \rho_1 + \boldsymbol{\nabla} \cdot (\rho_0 \mathbf{u}_1) = 0, \tag{3.13}$$

$$\rho_0 \partial_t \mathbf{u}_1 = -\boldsymbol{\nabla} p_1, \tag{3.14}$$

$$p_1 = c_0^2 \rho_1. \tag{3.15}$$

Taking the divergence of Eq. (3.14) and inserting Eq. (3.13) and Eq. (3.15) we get

$$\partial_t^2 \rho_1 = c_0^2 \nabla^2 \rho_1. \tag{3.16}$$

Taking the time derivative of Eq. (3.13) and inserting Eq. (3.14) and Eq. (3.15) we get

$$\partial_t^2 p_1 = c_0^2 \nabla^2 p_1. \tag{3.17}$$

By inserting Eq. (3.15) into Eq. (3.14) and taking the time derivative, and then inserting Eq. (3.13) we get

$$\partial_t^2 \mathbf{u}_1 = c_0^2 \boldsymbol{\nabla}(\boldsymbol{\nabla}\cdot\mathbf{u}_1). \tag{3.18}$$

However, as $\eta = 0$ we may assume that $\mathbf{u}_1$ is irrotational and can therefore be defined by a scalar potential

$$\mathbf{u}_1 = \boldsymbol{\nabla}\varphi_1. \tag{3.19}$$

since $\mathbf{u}_1$ is irrotational ($\partial_i u_j = \partial_j u_i$), we make use of $\boldsymbol{\nabla}(\boldsymbol{\nabla}\cdot\mathbf{u}) = \boldsymbol{\nabla}\cdot(\boldsymbol{\nabla}\mathbf{u}) = \nabla^2\mathbf{u}$

$$\boldsymbol{\nabla}(\boldsymbol{\nabla}\cdot\mathbf{u}) = \partial_i\partial_j u_j = \partial_j\partial_i u_j = \partial_j\partial_j u_i = \nabla^2\mathbf{u}, \tag{3.20}$$

$$\boldsymbol{\nabla}\cdot(\boldsymbol{\nabla}\mathbf{u}) = \partial_i\partial_i u_j = \nabla^2\mathbf{u}, \tag{3.21}$$

to rewrite Eq. (3.18) to a wave equation. Hence, we got

$$\partial_t^2 \mathbf{u}_1 = c_0^2 \nabla^2 \mathbf{u}_1. \tag{3.22}$$

Since Eqs. (3.16 - 3.17) and Eq. (3.22) all are standard wave equations, they have solutions consisting of linear combinations of traveling waves ($Ae^{i[k_0 x-\omega t]} + Be^{i[-k_0 x-\omega t]}$ in the 1D case). This indicates that the sound wave propagating in the liquid is described by the first order terms ($\mathbf{u}_1$, p_1, ρ_1).

By inserting Eq. (3.19) and Eq. (3.15) into Eq. (3.14) and removing $\partial_x, \partial_y, \partial_z$ by means of integration, we can express ρ_1 by φ_1

$$\rho_1 = -\frac{\rho_0}{c_0^2}\partial_t\varphi_1. \tag{3.23}$$

By inserting Eq. (3.23) into Eq. (3.15) we get

$$p_1 = -\rho_0\partial_t\varphi_1. \tag{3.24}$$

By inserting Eq. (3.19) and Eq. (3.23) into Eq. (3.13) we immediately see that φ_1 also follows the wave equation

$$\partial_t^2\varphi_1 = c_0^2\nabla^2\varphi_1. \tag{3.25}$$

By inserting a plane harmonic wave, $\rho_1 = \widehat{\rho}_1 e^{i(k_0 x-\omega t)}$, $k_0 = \omega/c_0$ into Eq. (3.23) or Eq. (3.24) and combining with Eq. (3.19) we can find $\mathbf{u}_1(\rho_1)$ or $\mathbf{u}_1(p_1)$

$$\mathbf{u}_1 = \frac{c_0}{\rho_0}\rho_1\mathbf{e}_x = \frac{c_0^2}{Z}\rho_1\mathbf{e}_x, \tag{3.26}$$

$$\mathbf{u}_1 = \frac{1}{c_0\rho_0}p_1\mathbf{e}_x = \frac{1}{Z}p_1\mathbf{e}_x, \tag{3.27}$$

where $Z = \rho_0 c_0$ is the acoustic impedance.

3.2.3 Second-order perturbation

The governing equations to second order becomes,

$$\partial_t \rho_2 + \boldsymbol{\nabla}\cdot(\rho_0 \mathbf{u}_2) + \boldsymbol{\nabla}\cdot(\rho_1 \mathbf{u}_1) = 0, \tag{3.28}$$

$$\rho_0 \partial_t \mathbf{u}_2 + \rho_1 \partial_t \mathbf{u}_1 + \rho_0(\mathbf{u}_1\cdot\boldsymbol{\nabla})\mathbf{u}_1 = -\boldsymbol{\nabla} p_2, \tag{3.29}$$

$$p_2 = c_0^2 \rho_2. \tag{3.30}$$

Introducing the mass-flux

$$\mathbf{J}_2 \equiv \rho_0 \mathbf{u}_2 + \rho_1 \mathbf{u}_1, \tag{3.31}$$

we can write Eq. (3.28) as

$$\partial_t \rho_2 + \boldsymbol{\nabla}\cdot\mathbf{J}_2 = 0. \tag{3.32}$$

Inserting both Eq. (3.31) and Eq. (3.30) into Eq. (3.29) we get

$$\partial_t \mathbf{J}_2 = -\mathbf{F} - c_0^2 \boldsymbol{\nabla}\rho_2, \tag{3.33}$$

where

$$\mathbf{F} \equiv \rho_0(\mathbf{u}_1\cdot\boldsymbol{\nabla})\mathbf{u}_1 + \rho_0 \mathbf{u}_1(\boldsymbol{\nabla}\cdot\mathbf{u}_1). \tag{3.34}$$

In the definition of $\mathbf{F}$, we have used Eq. (3.13) to rewrite $\mathbf{u}_1\partial_t\rho_1 = -\mathbf{u}_1\boldsymbol{\nabla}\cdot(\rho_0\mathbf{u}_1)$. Taking the time average of Eq. (3.32) and Eq. (3.33) we get

$$\boldsymbol{\nabla}\cdot\mathbf{J}_2'' = 0 \qquad \Rightarrow \qquad \boldsymbol{\nabla}\cdot\mathbf{u}_2'' = -\frac{1}{\rho_0}\boldsymbol{\nabla}\cdot\langle\rho_1\mathbf{u}_1\rangle_t. \tag{3.35}$$

$$\boldsymbol{\nabla}\rho_2'' = -\frac{1}{c_0^2}\mathbf{F}'', \tag{3.36}$$

where $\mathbf{J}_2'' = \langle\mathbf{J}_2\rangle_t$ and

$$\langle\rho_1\mathbf{u}_1\rangle_t = \frac{1}{2}\left(\mathrm{Re}[\tilde{\rho}_1]\mathrm{Re}[\tilde{\mathbf{u}}_1] + \mathrm{Im}[\tilde{\rho}_1]\mathrm{Im}[\tilde{\mathbf{u}}_1]\right) = \frac{1}{2}\mathrm{Re}\,[\tilde{\rho}_1\tilde{\mathbf{u}}^*], \tag{3.37}$$

$$\begin{aligned}\mathbf{F}'' &= \frac{1}{2}\rho_0\Big[\Big(\mathrm{Re}\big[\tilde{\mathbf{u}}_1\big]\cdot\boldsymbol{\nabla}\Big)\mathrm{Re}\big[\tilde{\mathbf{u}}_1\big] + \Big(\mathrm{Im}\big[\tilde{\mathbf{u}}_1\big]\cdot\boldsymbol{\nabla}\Big)\mathrm{Im}\big[\tilde{\mathbf{u}}_1\big]\Big] \\ &\quad + \frac{1}{2}\rho_0\Big[\mathrm{Re}\big[\tilde{\mathbf{u}}_1\big]\Big(\boldsymbol{\nabla}\cdot\mathrm{Re}\big[\tilde{\mathbf{u}}_1\big]\Big) + \mathrm{Im}\big[\tilde{\mathbf{u}}_1\big]\Big(\boldsymbol{\nabla}\cdot\mathrm{Im}\big[\tilde{\mathbf{u}}_1\big]\Big)\Big] \\ &= \frac{1}{2}\rho_0\mathrm{Re}\big[(\tilde{\mathbf{u}}_1\cdot\boldsymbol{\nabla})\tilde{\mathbf{u}}_1^*\big] + \frac{1}{2}\rho_0\mathrm{Re}\big[\tilde{\mathbf{u}}_1(\boldsymbol{\nabla}\cdot\tilde{\mathbf{u}}_1^*\big].\end{aligned} \tag{3.38}$$

From these equations we see to our surprise that Eq. (3.35) and Eq. (3.36) no longer predicts a relation between $\mathbf{u}_2''$ and ρ_2''. Hence they cannot be solved for a general case. This shows us that the approximation of neglecting the viscosity is a far to rough approximation. We can therefore conclude that viscosity must be included.

3.3 The viscous case

In this section we assume that $\eta \neq 0$ and $\zeta \neq 0$.

3.3.1 Zeroth-order perturbation

Same as without viscosity. Again ρ_0 and p_0 are constant in time and space, and $\mathbf{u}_0 = 0$.

3.3.2 First-order perturbation

The first order equations becomes

$$-\partial_t \rho_1 = \boldsymbol{\nabla}\cdot(\rho_0 \mathbf{u}_1) = \rho_0(\boldsymbol{\nabla}\cdot\mathbf{u}_1), \tag{3.39}$$

$$\rho_0 \partial_t \mathbf{u}_1 = -\boldsymbol{\nabla} p_1 + \eta\nabla^2\mathbf{u}_1 + \beta\eta\boldsymbol{\nabla}\Big(\boldsymbol{\nabla}\cdot\mathbf{u}_1\Big), \tag{3.40}$$

$$p_1 = c_0^2 \rho_1. \tag{3.41}$$

Taking the divergence of Eq. (3.40) and inserting the left hand side of Eq. (3.39) we find

$$\partial_t^2 \rho_1 = c_0^2\nabla^2\rho_1 + (\beta+1)\frac{\eta}{\rho_0}\nabla^2\partial_t\rho_1 \tag{3.42}$$

by insertion of Eq. (3.41) we get

$$\partial_t^2 p_1 = c_0^2\nabla^2 p_1 + (\beta+1)\frac{\eta}{\rho_0}\nabla^2\partial_t p_1. \tag{3.43}$$

In the non-stationary steady state, we may assume that ρ_1, p_1 and $\mathbf{u}_1$ are oscillating harmonically in time, since the system is driven by a harmonic force, $\mathbf{f}(\mathbf{r},t) = \mathbf{f}(\mathbf{r})e^{-i\omega t}$. Hence, we introduce

$$\rho_1 = \tilde{\rho}_1 e^{-i\omega t}, \qquad p_1 = \tilde{p}_1 e^{-i\omega t}, \qquad \mathbf{u}_1 = \tilde{\mathbf{u}}_1 e^{-i\omega t}. \tag{3.44}$$

which allows us to substitute

$$\partial_t = -i\omega \quad \text{and} \quad \partial_t^2 = -\omega^2 \tag{3.45}$$

into Eq. (3.43), which yields

$$\left[1 - i\frac{\omega\eta(\beta+1)}{\rho_0 c_0^2}\right]\nabla^2\tilde{p_1} + \frac{\omega^2}{c_0^2}\tilde{p_1} = 0. \tag{3.46}$$

Furthermore we find the relation between p_1 and $\mathbf{u}_1$ by inserting Eq. (3.39) into Eq. (3.40) and then substitute the time derivatives as defined.

$$\nabla^2\tilde{\mathbf{u}}_1 = -i\frac{\omega\rho_0}{\eta}\tilde{\mathbf{u}}_1 + \Big[1 - i\frac{\omega\beta\eta}{\rho_0 c_0^2}\Big]\frac{1}{\eta}\boldsymbol{\nabla}\tilde{p}_1 \tag{3.47}$$

These are the equations describing the first-order pressure field and particle velocity. Notice that the particle velocity is the velocity at which a particle oscillates and not at which the wave travels.

We can extract further information from Eq. (3.46), if we rewrite it using the first order Taylor expansion, $(1-x)^p \approx 1 - px$

$$\nabla^2 \tilde{p}_1 = -\frac{\omega^2}{c_0^2}\left[1 + i\frac{\omega\eta(\beta+1)}{\rho_0 c_0^2}\right]\tilde{p}_1. \tag{3.48}$$

The term $\frac{(\beta+1)\omega\eta}{2\rho_0 c_0^2}$ has a typical numerical value of

$$\gamma \equiv \frac{(\beta+1)\omega\eta}{2\rho_0 c_0^2} \approx \frac{10^6\ \mathrm{s}^{-1} \times 10^{-3}\ \mathrm{Pa\,s}}{10^3\ \mathrm{kg\ m}^{-3} \times 10^6\ \mathrm{m}^2\ \mathrm{s}^{-2}} \approx 10^{-6}. \tag{3.49}$$

Hence, we can argue that

$$\left[1 + i\frac{\omega\eta(\beta+1)}{\rho_0 c_0^2}\right] \approx \Big[1 + i\gamma\Big]^2. \tag{3.50}$$

Our Helmholtz equation then becomes

$$\nabla^2 \tilde{p}_1 = -k_0^2\Big[1 + i\gamma\Big]^2 \tilde{p}_1 \qquad , k_0 \equiv \frac{\omega}{c_0}. \tag{3.51}$$

From simple insertion, we se that the plane attenuated wave,

$$\tilde{p}_1 = \widehat{p_1} e^{\pm i k_0 (1+i\gamma)x} = \widehat{p_1} e^{\pm k_0 (i-\gamma)x}, \tag{3.52}$$

is a solution to the Helmholtz equation.

By inserting the plane attenuated wave into Eq. (3.39), we see that

$$\boldsymbol{\nabla}\cdot\mathbf{u}_1 = -\frac{1}{\rho_0}\partial_t \rho_1 = \frac{i\omega}{\rho_0}\widehat{\rho_1} e^{k_0(i-\gamma)x - i\omega t}. \tag{3.53}$$

Hence,

$$\mathbf{u}_1 = \frac{(1-i\gamma)c_0}{\rho_0}\rho_1 \mathbf{e}_x = \frac{(1-i\gamma)c_0^2}{Z}\rho_1 \mathbf{e}_x \tag{3.54}$$

fulfills the equation. We find $\mathbf{u}_1(p_1)$ by inserting $\rho_1 = p_1/c_0^2$ into Eq. (3.54)

$$\mathbf{u}_1 = \frac{(1-i\gamma)}{c_0\rho_0}p_1 \mathbf{e}_x = \frac{(1-i\gamma)}{Z}p_1 \mathbf{e}_x \tag{3.55}$$

Notice that if $\gamma \to 0$ Eq. (3.54) and Eq. (3.55) are identical to Eq. (3.26) and Eq. (3.27).

3.3.3 Second-order perturbation

The second order equations becomes

$$\partial_t \rho_2 + \boldsymbol{\nabla}\cdot(\rho_0 \mathbf{u}_2) + \boldsymbol{\nabla}\cdot(\rho_1 \mathbf{u}_1) = 0, \tag{3.56}$$

$$\rho_0 \partial_t \mathbf{u}_2 + \rho_1 \partial_t \mathbf{u}_1 + \rho_0(\mathbf{u}_1\cdot\boldsymbol{\nabla})\mathbf{u}_1 = -\boldsymbol{\nabla} p_2 + \eta\nabla^2\mathbf{u}_2 + \beta\eta\boldsymbol{\nabla}\Big(\boldsymbol{\nabla}\cdot\mathbf{u}_2\Big), \tag{3.57}$$

$$p_2 = c_0^2 \rho_2. \tag{3.58}$$

Inserting $\mathbf{J}_2$ and $\mathbf{F}$ as previously defined we get

$$\partial_t \rho_2 + \boldsymbol{\nabla}\cdot\mathbf{J}_2 = 0, \tag{3.59}$$

$$\partial_t \mathbf{J}_2 = -\mathbf{F} - \boldsymbol{\nabla} p_2 + \eta\nabla^2\mathbf{u}_2 + \beta\eta\boldsymbol{\nabla}\Big(\boldsymbol{\nabla}\cdot\mathbf{u}_2\Big). \tag{3.60}$$

Taking the time average of Eq. (3.59) and Eq. (3.60) we find

$$\begin{aligned}
&\boldsymbol{\nabla}\cdot\mathbf{J}_2'' = 0 \\
&\boldsymbol{\nabla}\cdot\mathbf{u}_2'' = -\frac{1}{\rho_0}\boldsymbol{\nabla}\cdot\langle\rho_1\mathbf{u}_1\rangle_t = -\frac{1}{c_0^2\rho_0}\boldsymbol{\nabla}\cdot\langle p_1\mathbf{u}_1\rangle_t = -\frac{1}{2c_0^2\rho_0}\boldsymbol{\nabla}\cdot\mathrm{Re}\left[\tilde{p}_1\tilde{\mathbf{u}}_1^*\right] \\
&\boldsymbol{\nabla}\cdot\mathbf{u}_2'' = S, \qquad\qquad S = -\frac{1}{2c_0^2\rho_0}\boldsymbol{\nabla}\cdot\mathrm{Re}\left[\tilde{p}_1\tilde{\mathbf{u}}_1^*\right]
\end{aligned} \tag{3.61}$$

$$\begin{aligned}
0 =& -\mathbf{F}'' - \boldsymbol{\nabla} p_2'' + \eta\nabla^2\mathbf{u}_2'' + \beta\eta\boldsymbol{\nabla}\Big(\boldsymbol{\nabla}\cdot\mathbf{u}_2''\Big) \\
\eta\nabla^2\mathbf{u}_2'' + \beta\eta\boldsymbol{\nabla}\Big(\boldsymbol{\nabla}\cdot\mathbf{u}_2''\Big) =& \boldsymbol{\nabla} p_2'' + \mathbf{F}'',
\end{aligned} \tag{3.62}$$

We notice that $\langle\partial_t\mathbf{J}_2\rangle_t = 0$ in steady state. Hence, to find the streaming velocity, $\mathbf{u}_2''$, we need to solve a scalar equation and a vector equation where both S and $\mathbf{F}''$ consists only of known terms. We notice that if $\mathbf{u}_2''$ is solenoidal, then Eq. (3.62) is identical to that of Nyborg[26]. In Chapter 7 we shall solve these equations for three different examples. But first we will look closer at the first-order terms, which contains the acoustic waves.

Chapter 4

Planer sound waves

As shown in Section 3.2.2 the acoustic waves is introduced in the first-order equation, which show up to be ordinary wave-equations. In this chapter we shall look closer at the solutions to the wave-equation.

4.1 Wave-emission from an oscillating wall

We imagine a semi-infinite fluid next to a piezo crystal located such that the fluid-crystal interface is at $(x, y, z) = \mathbf{0}$ with the outwards pointing normal vector, $\mathbf{n}$. The crystal is set to vibrate and the position, $\mathbf{d}_w(t)$ is thus described by $\mathbf{d}_w(t) = i\ell\mathbf{n}e^{-i\omega t}$, where ℓ is the vibration amplitude. The velocity of the wall, $\mathbf{u}_w$ and the acceleration, $\mathbf{a}_w$ is found by single and double differentiation, respectively.

$$\mathbf{u}_w = \mathbf{u}_1(\mathbf{0}, t) = \ell\omega\mathbf{n}e^{-i\omega t}. \tag{4.1}$$

$$\mathbf{a}_w = \partial_t\mathbf{u}_1(\mathbf{0}, t) = -i\ell\omega^2\mathbf{n}e^{-i\omega t}. \tag{4.2}$$

Assuming the wall has vibrated long enough for a steady state to be established, we see, by using $\mathbf{u}_w$ as a boundary condition, that the first order velocity of the fluid can be described as

$$\mathbf{u}_1(\mathbf{r}, t) = \ell\omega\mathbf{n}e^{i(\mathbf{k}\cdot\mathbf{r}-\omega t)}, \tag{4.3}$$

where $\mathbf{k} = k_0\frac{\mathbf{n}}{|\mathbf{n}|}$. By requiring that $c_0 = \omega/k_0$ we ensure that $\mathbf{u}_1$ fulfills the wave equation. Using Eqs. (3.19 - 3.24) we find φ, ρ_1 and p_1

$$\varphi(\mathbf{r}, t) = -i\ell c_0 e^{i(\mathbf{k}\cdot\mathbf{r}-\omega t)}, \tag{4.4a}$$

$$\rho_1(\mathbf{r}, t) = \rho_0\ell k_0 e^{i(\mathbf{k}\cdot\mathbf{r}-\omega t)}, \tag{4.4b}$$

$$p_1(\mathbf{r}, t) = \rho_0\omega\ell c_0 e^{i(\mathbf{k}\cdot\mathbf{r}-\omega t)} = Z_0\omega\ell e^{i(\mathbf{k}\cdot\mathbf{r}-\omega t)}. \tag{4.4c}$$

where $Z_0 = \rho_0 c_0$ is the acoustic impedance of the media.

4.2 Wave propagation through a single interface

An unattenuated sound wave traveling (from left to right, hence, the subscript r) in one media(A), is eventually bound to hit the interface of another media(B). At such an interface the incoming sound wave, $\varphi_{A,r}$, will be split into a reflected, $\varphi_{A,l}$, and a transmitted, $\varphi_{B,r}$, wave. Hence, we got

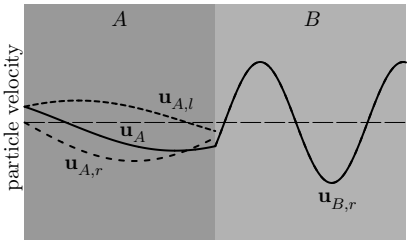

Figure 4.1: Since φ is not continues over interfaces we plot the particle velocity. The incoming wave, $u_{A,r}$ is split up into a reflected wave, $u_{A,l}$ and a transmitted wave, $u_{B,r}$.

$$\varphi_A(x,t) = A_r e^{i(k_A x-\omega t)} + A_l e^{i(-k_A x-\omega t)}, \quad (4.5a)$$

$$\varphi_B(x,t) = B_r e^{i(k_B x-\omega t)} + 0 e^{i(-k_B x-\omega t)}. \quad (4.5b)$$

To describe the amplitudes of the resulting waves, A_l and B_r, we define the reflection coefficient, $\mathcal{R}_I$ and the transmission coefficient, $\mathcal{T}_I$, so they represent the ratio between the reflected or transmitted intensity and that of the incoming wave ($I_{A,r}(L,t) = \langle Z_A(\partial_x \varphi_{A,r})^2\rangle_t$). The subscript 'I' reminds us that the coefficients apply to the intensity.

Let the interface be positioned at $x = L$, then due to conservation of energy we must require that

$$I_{A,r}(L,t) = I_{A,l}(L,t) + I_{B,r}(L,t), \quad (4.6a)$$

$$\langle Z_A(\partial_x \varphi_{A,r})^2\rangle_t = \langle Z_A(\partial_x \varphi_{A,l})^2\rangle_t + \langle Z_B(\partial_x \varphi_{B,r})^2\rangle_t, \quad (4.6b)$$

$$-\frac{1}{2} Z_A k_A^2 |A_r|^2 = -\frac{1}{2} Z_A k_A^2 |A_l|^2 - \frac{1}{2} Z_B k_B^2 |B_r|^2, \quad (4.6c)$$

$$1 = \left(\frac{|A_l|}{|A_r|}\right)^2 + \frac{\rho_B k_B}{\rho_A k_A}\left(\frac{|B_r|}{|A_r|}\right)^2, \quad (4.6d)$$

where we have used $Z_i = \rho_i c_i = \rho_i \omega / k_i$. Hence, we define

$$\mathcal{R}_I = \left(\frac{|A_l|}{|A_r|}\right)^2, \quad (4.7a)$$

$$\mathcal{T}_I = \frac{\rho_B k_B}{\rho_A k_A}\left(\frac{|B_r|}{|A_r|}\right)^2, \quad (4.7b)$$

so that $\mathcal{R}_I + \mathcal{T}_I = 1$.

To determine the the amplitudes of A_l and B_r we need two equations, which we derive from boundary conditions.

By requiring that the particle velocity, u is continues over the interface we get the boundary condition $\partial_x \varphi_A(L,t) = \partial_x \varphi_B(L,t)$. And from Newton's third law we know that the force on the interface must be equal on both sides, hence, the same must be valid for the pressure, leading us to the another boundary condition: $\rho_A \varphi_A(L,t) = \rho_B \varphi_B(L,t)$. Hence we got the two equations

$$ik_A A_r e^{i(k_A L - \omega t)} - ik_A A_l e^{i(-k_A L - \omega t)} = ik_B B_r e^{i(k_B L - \omega t)}, \tag{4.8a}$$

$$\rho_A A_r e^{i(k_A L - \omega t)} + \rho_A A_l e^{i(-k_A L - \omega t)} = \rho_B B_r e^{i(k_B L - \omega t)}, \tag{4.8b}$$

which can be reduced to

$$\frac{k_A}{k_B} A_r e^{ik_A L} - \frac{k_A}{k_B} A_l e^{-ik_A L} = B_r e^{ik_B L}, \tag{4.9a}$$

$$\frac{\rho_A}{\rho_B} A_r e^{ik_A L} + \frac{\rho_A}{\rho_B} A_l e^{-ik_A L} = B_r e^{ik_B L}, \tag{4.9b}$$

by inserting one into the other we see that

$$\frac{A_l}{A_r} = \frac{Z_B - Z_A}{Z_B + Z_A} e^{i2k_A L}. \tag{4.10}$$

Dividing Eq. (4.9b) by A_r and inserting Eq. (4.10) we get

$$\frac{B_r}{A_r} = \frac{\rho_A}{\rho_B} \left(\frac{2Z_B}{Z_B + Z_A} \right) e^{i(k_A - k_B)L}. \tag{4.11}$$

From Eq. (4.10) and Eq. (4.11) we see that

$$\mathcal{R}_I(A \to B) = \left(\frac{|A_l|}{|A_r|} \right)^2 = \left(\frac{Z_B - Z_A}{Z_B + Z_A} \right)^2, \tag{4.12a}$$

$$\mathcal{T}_I(A \to B) = \frac{\rho_B k_B}{\rho_A k_A} \left(\frac{|B_r|}{|A_r|} \right)^2 = \frac{\rho_B k_B}{\rho_A k_A} \left[\frac{\rho_A}{\rho_B} \left(\frac{2Z_B}{Z_B + Z_A} \right) \right]^2 = \frac{Z_A}{Z_B} \left(\frac{2Z_B}{Z_B + Z_A} \right)^2. \tag{4.12b}$$

To verify this result, we check that intensity is conserved

$$\begin{aligned} 1 &= \mathcal{R}_I + \mathcal{T}_I, \\ 1 &= \left(\frac{Z_B - Z_A}{Z_B + Z_A} \right)^2 + \frac{Z_A}{Z_B} \left(\frac{2Z_B}{Z_B + Z_A} \right)^2, \\ 1 &= \frac{Z_B^2 + Z_A^2 - 2Z_B Z_A}{(Z_B + Z_A)^2} + \frac{4Z_B Z_A}{(Z_B + Z_A)^2}, \\ 1 &= \frac{(Z_B + Z_A)^2}{(Z_B + Z_A)^2} = 1. \end{aligned} \tag{4.13}$$

4.3 Wave propagation through multiple interfaces

When the acoustic wave passes through several interfaces the corresponding equations gets slightly more complicated. we have four materials(A, B, C, D) divided by three interfaces at $x = L_A$, $x = L_B$ and $x = L_C$ as shown in Fig. 4.2.

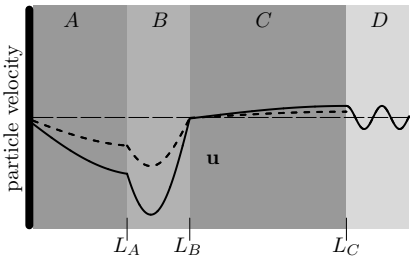

Figure 4.2: The incoming wave, u_r is propagated through several interfaces.

$$\varphi_A(x,t) = A_r e^{i(k_A x-\omega t)} + A_l e^{i(-k_A x-\omega t)}, \quad (4.14a)$$
$$\varphi_B(x,t) = B_r e^{i(k_B x-\omega t)} + B_l e^{i(-k_B x-\omega t)}, \quad (4.14b)$$
$$\varphi_C(x,t) = C_r e^{i(k_C x-\omega t)} + C_l e^{i(-k_C x-\omega t)}, \quad (4.14c)$$
$$\varphi_D(x,t) = D_r e^{i(k_D x-\omega t)} + D_l e^{i(-k_D x-\omega t)}, \quad (4.14d)$$

From the two boundary conditions

$$\partial_x \varphi_{j+1}(L_j,t) = \partial_x \varphi_j(L_j,t), \quad (4.15)$$
$$-\rho_{j+1}\partial_t \varphi_{j+1}(L_j,t) = -\rho_j \partial_t \varphi_j(L_j,t), \quad (4.16)$$

we got the two equations

$$ik_{j+1}\varphi^*_{j+1,r}e^{i(k_{j+1}L_j-\omega t)} - ik_{j+1}\varphi^*_{j+1,r}e^{i(-k_{j+1}L_j-\omega t)} = ik_j\varphi^*_{j,r}e^{i(k_jL_j-\omega t)} - ik_j\varphi^*_{j,l}e^{i(-k_jL_j-\omega t)} \quad (4.17a)$$

$$i\rho_{j+1}\omega\varphi^*_{j+1,r}e^{i(k_{j+1}L_j-\omega t)} + i\rho_{j+1}\omega\varphi^*_{j+1,r}e^{i(-k_{j+1}L_j-\omega t)} = i\rho_j\omega\varphi^*_{j,r}e^{i(k_jL_j-\omega t)} + i\rho_j\omega\varphi^*_{j,l}e^{i(-k_jL_j-\omega t)}. \quad (4.17b)$$

Which we can reduce and write as matrix equation

$$\begin{bmatrix} e^{ik_{j+1}L_j} & -e^{-ik_{j+1}L_j} \\ e^{ik_{j+1}L_j} & e^{-ik_{j+1}L_j} \end{bmatrix} \begin{pmatrix} \varphi^*_{j+1,r} \\ \varphi^*_{j+1,l} \end{pmatrix} = \begin{bmatrix} \frac{k_j}{k_{j+1}}e^{ik_jL_j} & -\frac{k_j}{k_{j+1}}e^{-ik_jL_j} \\ \frac{\rho_j}{\rho_{j+1}}e^{ik_jL_j} & \frac{\rho_j}{\rho_{j+1}}e^{-ik_jL_j} \end{bmatrix} \begin{pmatrix} \varphi^*_{j,r} \\ \varphi^*_{j,l} \end{pmatrix} \quad (4.18a)$$

We then use the relation

$$\begin{bmatrix} a & b \\ c & d \end{bmatrix}^{-1} = \frac{1}{ad-cd}\begin{bmatrix} d & -b \\ -c & a \end{bmatrix}, \quad (4.19)$$

to multiply both sides by the inverse of the left matrix.

$$\begin{pmatrix} \varphi^*_{j+1,r} \\ \varphi^*_{j+1,l} \end{pmatrix} = \frac{1}{2}\begin{bmatrix} e^{-ik_{j+1}L_j} & e^{-ik_{j+1}L_j} \\ -e^{ik_{j+1}L_j} & e^{ik_{j+1}L_j} \end{bmatrix} \begin{bmatrix} \frac{k_j}{k_{j+1}}e^{ik_jL_j} & -\frac{k_j}{k_{j+1}}e^{-ik_jL_j} \\ \frac{\rho_j}{\rho_{j+1}}e^{ik_jL_j} & \frac{\rho_j}{\rho_{j+1}}e^{-ik_jL_j} \end{bmatrix} \begin{pmatrix} \varphi^*_{j,r} \\ \varphi^*_{j,l} \end{pmatrix} \quad (4.20a)$$

$$\begin{pmatrix} \varphi^*_{j+1,r} \\ \varphi^*_{j+1,l} \end{pmatrix} = \frac{1}{2} \begin{bmatrix} \left(\frac{k_j}{k_{j+1}} + \frac{\rho_j}{\rho_{j+1}}\right) e^{i(k_j - k_{j+1})L_j} & \left(\frac{\rho_j}{\rho_{j+1}} - \frac{k_j}{k_{j+1}}\right) e^{-i(k_j + k_{j+1})L_j} \\ \left(\frac{\rho_j}{\rho_{j+1}} - \frac{k_j}{k_{j+1}}\right) e^{i(k_j + k_{j+1})L_j} & \left(\frac{k_j}{k_{j+1}} + \frac{\rho_j}{\rho_{j+1}}\right) e^{-i(k_j - k_{j+1})L_j} \end{bmatrix} \begin{pmatrix} \varphi^*_{j,r} \\ \varphi^*_{j,l} \end{pmatrix} \tag{4.20b}$$

By introducing the transmission matrix

$$T_{(j+1,j)} = \begin{bmatrix} \frac{1}{2}\left(\frac{k_j}{k_{j+1}} + \frac{\rho_j}{\rho_{j+1}}\right) e^{i(k_j - k_{j+1})L_j} & \frac{1}{2}\left(\frac{\rho_j}{\rho_{j+1}} - \frac{k_j}{k_{j+1}}\right) e^{-i(k_j + k_{j+1})L_j} \\ \frac{1}{2}\left(\frac{\rho_j}{\rho_{j+1}} - \frac{k_j}{k_{j+1}}\right) e^{i(k_j + k_{j+1})L_j} & \frac{1}{2}\left(\frac{k_j}{k_{j+1}} + \frac{\rho_j}{\rho_{j+1}}\right) e^{-i(k_j - k_{j+1})L_j} \end{bmatrix}, \tag{4.21}$$

the equation simplifies to

$$\begin{pmatrix} \varphi^*_{j+1,r} \\ \varphi^*_{j+1,l} \end{pmatrix} = T_{(j+1,j)} \begin{pmatrix} \varphi^*_{j,r} \\ \varphi^*_{j,l} \end{pmatrix}. \tag{4.22}$$

The transmission matrix can be use multiple times with changing indexes, to find φ_N

$$\begin{pmatrix} \varphi^*_{N,r} \\ \varphi^*_{N,l} \end{pmatrix} = T_{(N,N-1)} T_{(N-1,N-2)} \cdots T_{(2,1)} \begin{pmatrix} \varphi^*_{1,r} \\ \varphi^*_{1,l} \end{pmatrix} \tag{4.23}$$

Assuming a piezo electric element is located at $x = 0$ is vibrating with the angular frequency, ω, and the amplitude, ℓ. We find the particle velocity at the to be

$$u_w = \partial_x \varphi_A(0,t) = \ell\omega e^{-i\omega t}. \tag{4.24}$$

We use this equation to find a relation between A_r and A_l.

$$u_w = \partial_x \varphi_A(x,t), \qquad x = 0 \tag{4.25a}$$

$$u_w = ik_A \left(A_r e^{ik_A x} - A_l e^{-ik_A x}\right) e^{-i\omega t}, \qquad x = 0 \tag{4.25b}$$

$$A_l = A_r e^{2ik_A x} + i\ell c_A e^{ik_A x}, \qquad x = 0 \tag{4.25c}$$

Furthermore we assume the last media stretches towards infinity. Hence, no wave is ever reflected in this media. This is a quite good approximation to the several meters of air normally surrounding a micro system in the lab. In the case of four medias as in Fig. 4.2 we require

$$D_l = 0. \tag{4.26}$$

By inserting Eq. (4.25c) and Eq. (4.26) into Eq. (4.23) it becomes

$$\begin{pmatrix} D_r \\ 0 \end{pmatrix} = T_{(D,C)} T_{(C,B)} T_{(B,A)} \begin{pmatrix} A_r \\ A_r + i\ell c_A \end{pmatrix}. \tag{4.27}$$

We have now reduced the problem to two equations with two unknowns(A_r, D_r), which is straight forward to solve. Once A_r and D_r has been found, A_l is found using Eq. (4.25c).

When we know both A_r and A_l we can find B_r and B_l from

$$\begin{pmatrix} B_r \\ B_l \end{pmatrix} = T_{(B,A)} \begin{pmatrix} A_r \\ A_l \end{pmatrix}. \tag{4.28}$$

This procedure is repeated until all unknown amplitudes has been found.

We apply this calculation on the one dimensional sandwich structure from Fig. 4.2, and define domain A as consisting of silicon with a thickness of $L_A = 300\,\mu$m, and domain B as 200 μm water and domain C as 500 μm pyrex and finally domain D as normal air. The incoming wave is generated by a piezo element located adjacent to domain A. This setup is similar to the one described in Section 1.3. The piezo element is set to oscillate with an amplitude of 1 nm. Below, the pressure and particle velocity has been plotted for two different frequencies.

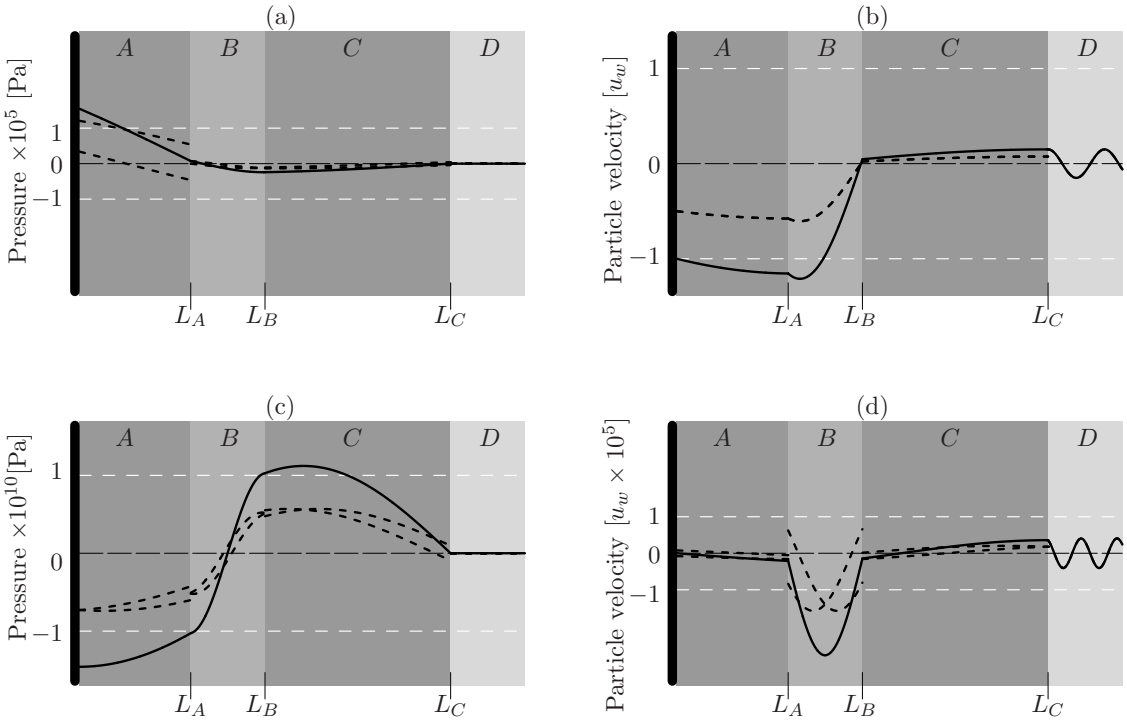

Figure 4.3: Panel (a) and (b) shows the pressure p_1 and particle velocity u_1 for the randomly picked non-resonance frequency 2.26 MHz. We notice the pressure is far to high for the perturbation method to be valid. This is due to the lack of damping. Panel (c) and (d) shows the pressure p_1 and particle velocity for the resonance frequency 3.56 MHz. We notice the amplitude for both pressure and particle velocity has increased dramatically for the resonance frequency.

Due to the resonance frequency the amplitudes of both the pressure and particle velocity has increased dramatically. If the resonance had been exactly hit, the amplitude would become infinite. We look closer into the resonance phenomenon in Section 4.4. In order to calculate the pressure distribution in more than one dimensions use a numerical tool

embedded in the commercial finite element program, COMSOL, this method is described in Chapter 5.

4.4 Acoustic Resonances

So far we have only considered one oscillating wall, and the waves induced by it. In this section we look at one-dimensional system bounded by two oscillating walls. The walls are located at $x = \pm L$ and are assumed to oscillated in opposite directions. Hence, to model the oscillating walls, we state

$$J_1(\pm L, t) = \pm \rho_0 \omega \ell e^{-i\omega t}, \tag{4.29}$$

4.4.1 Unattenuated waves

In the case of unattenuated waves, the first order velocity field, u_1 must be defined as a linear combination of two opposite travelling waves

$$u_1(x,t) = \tilde{u}_1(x)\ e^{-i\omega t}, \qquad \tilde{u}_1(x) = \widehat{u}_1 e^{-ik_0 x} + Be^{ik_0 x}. \tag{4.30}$$

However, due to the anti-symmetrically oscillating walls we must require that

$$\begin{aligned} \tilde{u}_1(x) &= -\tilde{u}_1(-x) \\ \widehat{u}_1 e^{-k_0(i-\gamma)x} + Be^{k_0(i-\gamma)x} &= -\widehat{u}_1 e^{k_0(i-\gamma)x} - Be^{-k_0(i-\gamma)x} \\ \widehat{u}_1 &= -B \end{aligned} \tag{4.31}$$

Hence, $\tilde{u}_1(x)$ gets the form

$$\tilde{u}_1(x) = \widehat{u}_1\Big(e^{-ik_0 x} - e^{ik_0 x}\Big) = -i2\widehat{u}_1 \sin(k_0 x) \tag{4.32}$$

From the antisymmetry we have the boundary conditions

$$\tilde{u}_1(-L) = -\omega\ell, \qquad \tilde{u}_1(0) = 0, \qquad \tilde{u}_1(L) = \omega\ell. \tag{4.33}$$

To tune in to a resonance frequency we choose

$$k_0 = \frac{n\pi}{L}, \qquad n = 1, 2, 3... \tag{4.34}$$

From the boundary conditions ($x = \pm L$) we get

$$\begin{aligned} -i2\widehat{u}_1 \sin(\pm n\pi) &= \pm\omega\ell \\ \widehat{u}_1 &= \frac{\pm i\omega\ell}{2\sin(\pm n\pi)} = i\infty. \end{aligned} \tag{4.35}$$

This result implies that at a resonance the unattenuated wave should have an infinitely high complex amplitude, and consequently contain an infinitely amount of energy. This is of cause non-physical, but so is the unattenuated waves. We therefore repeat the calculation with attenuated waves.

4.4.2 Attenuated waves

For attenuated waves, the first order velocity field, u_1 must be a linear combination of two opposite attenuated traveling waves

$$u_1(x,t) = \tilde{u}_1(x)\ e^{-i\omega t}, \qquad \tilde{u}_1(x) = \widehat{u}_1 e^{-k_0(i-\gamma)x} + Be^{k_0(i-\gamma)x}. \tag{4.36}$$

Again, due to the antisymmetric oscillating walls, we require that $\tilde{u}_1(x) = -\tilde{u}_1(-x)$, so $\widehat{u}_1 = -B$. Hence, $\tilde{u}_1(x)$ gets the form

$$\tilde{u}_1(x) = \widehat{u}_1\Big(e^{-k_0(i-\gamma)x} - e^{k_0(i-\gamma)x}\Big) \approx \widehat{u}_1\Big(2k_0\gamma x\cos(k_0x) - i2\sin(k_0x)\Big) \tag{4.37}$$

where we have used the fact that $\gamma \ll 1 \Rightarrow e^{\gamma x} \approx (1+\gamma x)$. It is worth noting that the small cosine wave is non-zero at boundary, while the much larger sine wave is zero and therefore contained in the specific region.

We still have the same boundary conditions and the resonance definition of k_0

$$\tilde{u}_1(-L) = -\omega\ell, \qquad \tilde{u}_1(0) = 0, \qquad \tilde{u}_1(L) = \omega\ell. \tag{4.38}$$

$$k_0 = \frac{n\pi}{L}, \qquad n = 1,2,3... \tag{4.39}$$

So to fulfil the boundary conditions ($x = \pm L$) we require

$$\widehat{u}_1\Big(\pm 2n\pi\gamma\cos(n\pi) - i2\sin(\pm n\pi)\Big) = \pm\omega\ell$$

$$\widehat{u}_1 = \frac{(-1)^n\omega\ell}{2n\pi\gamma}. \tag{4.40}$$

We notice that for attenuated waves ($\gamma > 0$) the resonance-amplitude becomes finite. However, due to the often very low value of γ, the resonance-amplitude can still be much higher than the wall oscillation amplitude. For $n = 3$ and $L = 1$ mm we find that

$$\widehat{u}_1 \approx -87 \text{ m/s}. \tag{4.41}$$

Chapter 5

Numerical simulations in COMSOL

In this chapter we will describe how the tools embedded in COMSOL has been used to simulate acoustic fields. COMSOL is a commercial software package used for numerical simulations of various physical problems. COMSOL utilizes the finite element method. In this chapter we shall first look at the embedded acoustic module, and secondly look at how equations can be entered manually.

5.1 The Acoustic module in COMSOL

In this section we examine the two different solving methods, which are embedded in the acoustic module. First we look at the eigenfrequency solver, which is used to find the different resonance frequencies, and secondly at the time harmonic solver, which can find the pressure field for any specified frequency.

5.1.1 The eigenfrequency solver

To find the eigenvalues of a system defined by a wave equation, the wave equation is reformulated to the Helmholtz equation. From Section 3.2.2 we have the first order pressure, p_1, described by a standard three dimensional wave equation Eq. (3.17).

$$\partial_t^2 p_1 = c_0^2 \nabla^2 p_1, \qquad p_1 = p_1(x, y, z, t). \tag{5.1}$$

Moving all terms to the left hand side and dividing by $\rho_0 c_0^2$,

$$-\frac{1}{\rho_0}\nabla^2 p_1 + \frac{1}{\rho_0 c_0^2}\partial_t^2 p_1 = 0. \tag{5.2}$$

Since we only care for the steady state, we require that the solution must be periodic in time. Hence, it is required that p_1 has the form,

$$p_1(x, y, z, t) = \widetilde{p_1}(x, y, z)e^{-i\omega t}. \tag{5.3}$$

Inserting this into Eq. (5.2)

$$-\frac{1}{\rho_0}\nabla^2 \widetilde{p_1} e^{-i\omega t} + \frac{1}{\rho_0 c_0^2}\partial_t^2 \widetilde{p_1} e^{-i\omega t} = 0. \tag{5.4}$$

Differentiating twice with respect to time,

$$-\frac{1}{\rho_0}\nabla^2\widetilde{p_1}e^{-i\omega t}+\frac{(-i\omega)^2}{\rho_0 c_0^2}\widetilde{p_1}e^{-i\omega t}=0. \tag{5.5}$$

Reinserting p_1, and introducing[1] $\lambda_e = \omega^2$,

$$-\frac{1}{\rho_0}\nabla^2 p_1 - \frac{\lambda_e}{\rho_0 c_0^2}p_1 = 0 \tag{5.6}$$

If substituting $\frac{\lambda_e}{\rho_0 c_0^2} = k$ this equation is called the Helmholtz equation. The Helmholtz equation can easily be solved analytically for very simple geometries[32]. For a box with the side-lengths a, b and c we get

$$\lambda_e = c_s^2\pi^2\left(\frac{n^2}{a^2}+\frac{m^2}{b^2}+\frac{l^2}{c^2}\right) \tag{5.7}$$

where

$$\begin{aligned} 0<x<a \quad &, \quad n=1,2,... \\ 0<y<b \quad &, \quad m=1,2,... \\ 0<z<c \quad &, \quad l=1,2,... \end{aligned} \tag{5.8}$$

For more complex geometries we use COMSOL to solve the problem numerically.

5.1.2 Example: Pseudo-one-dimensional

An example of a more complicated geometry could be blocks of different materials stacked together. Due to the differences in materiel parameters the solution will no longer be trivial. For further comparing, we choose to work on a pseudo one dimensional problem. By choosing a one dimensional problem, we can verify the numerical results by comparing with analytical results based on the equations from Section 4.3. The reason why we call this problem 'pseudo one dimensional' is that it really is two dimensional. But we keep one dimension so narrow that, no wave can appear here, except for very high frequencies. This mean that for relative low frequencies the model can be regarded as one dimensional. Instead of setting up the problem in the COMSOL GUI we will use scripting. The problem we are going to solve resembles the sandwich structure from Section 4.3 and Section 1.3. We start by initiating the variables we are going to use.

COMSOL

```
% Initializing
flclear fem
MF = 15;
NSOL = 4;
Lstart = 500;
```

COMSOL

[1] Notice that the definition of λ_e will vary with different versions of COMSOL, This definition is from ver. 3.2a

We notice that line 1 has been commented out, this line simply serves to remind us that this part of the script initializes the variables. The second line makes sure the variable 'fem' is empty, the 'fem' variable is used to store the entire FEM-environment. The third line sets the value of the variable 'MF', this is to be used later on when defining the mesh. 'NSOL' is the number of solutions we want COMSOL to find. 'Lstart' is the value, on which the search for eigenvalues should be centered. 'Lstart' must not be an eigenvalue itself.

Next we define the geometry. We keep the geometry to three domains, hence the surrounding air is omitted. We make the three domains 300 μm, 200 μm and 500 μm wide, but only 10 μm high. This way we keep a sufficiently high aspect ratio to treat the system as one dimensional.

COMSOL

```
6  % Geometry
7  g1 = rect2(3e-4,10e-6);
8  g2 = rect2(2e-4,10e-6,'pos',[3e-4,0]);
9  g3 = rect2(5e-4,10e-6,'pos',[5e-4,0]);
10 fem.draw.s.objs = {g1,g2,g3};
11 fem.geom = geomcsg(fem);
```

COMSOL

Line 7-9 defines the three domains. 'g2' and 'g3' are furthermore repositioned. Line 10 stores the geometry in the 'fem' variable. Line 11 analyzes the stored geometry, and saves it in 'fem.geom' if it proves valid. The resulting geometry can be seen in Fig. 5.1, notice the axes are scaled differently.

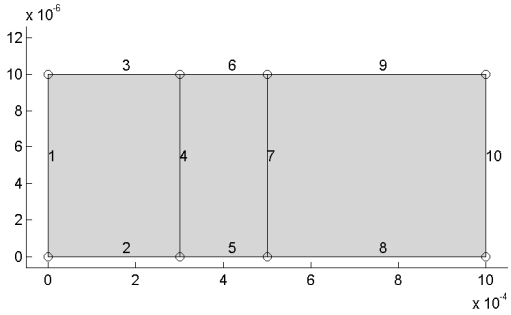

Figure 5.1: The pseudo one-dimensional geometry. Notice the axes are scaled differently. The aspect ratio is 1:100 The numbers indicate the index of the domain boundaries.

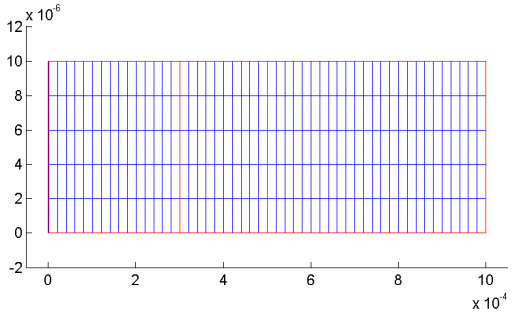

Figure 5.2: The mesh configuration. To improve visualization the mesh has been plotted for MF = 5. For accurate results MF should at least be a few times greater.

The next step is to define the mesh, in this calculation we use a rectangular mesh, we could also have used a triangular mesh.

COMSOL

```
12 % Meshing
13 fem.mesh=meshmap(fem, ...
14                  'edgelem',{2,[3*MF],3,[3*MF],...
15                             5,[2*MF],6,[2*MF],...
16                             8,[5*MF],9,[5*MF],...
17                             10,[5],1,[5]});
```

COMSOL

Actually this box only contains one real line. The three successive dots simply implies that the line is continued below. In line 13 and forth we only define the number of elements on the outer boundaries. It is important that opposite boundaries have the same number of elements, otherwise the 'meshmap()' function will not work. The syntax of the 'edgelem' part is `,'edgelem',{index,[number of elements],index,[number of elements]}`. Hence, we set the boundaries with index 2 and 3 to '`3*MF`', and the boundaries with index 5 and 6 to '`2*MF`' and so on. In Fig. 5.2 the mesh is plotted for MF=5.

After defining the mesh, the physics are added.

COMSOL

```
18 % Physics
19 fem.appl.mode.class = 'Acoustics';
20 fem.appl.prop.analysis='eigen';
21 fem.appl.equ.cs = {8490,1483,5640};
22 fem.appl.equ.rho = {2331,998.2,2230};
23 fem.appl.equ.ind = [1,2,3];
24 fem.appl.bnd.type = {'SS','SH','cont'};
25 fem.appl.bnd.ind = [2,2,2,3,2,2,3,2,2,1];
```

COMSOL

When adding the physics we need the governing equations and the boundary conditions. In line 19 the acoustics module is loaded, this module contains the necessary equations, we only have to specify them. This is done in line 20 where the type of analysis is chosen to be an eigenfrequency analysis. Hence, the governing equation in all domains becomes,

$$-\frac{1}{\rho}\nabla^2 p_1 + \frac{\lambda_e}{\rho c_s^2} p_1 = 0 \tag{5.9}$$

Which, fortunately is the exact same as Eq. (5.6) derived above. In line 21 and 22 we define the material parameters for three different domain groups, which are distributed to the three available domains in line 23.

Material	Silicon	Water	Pyrex
Group nr.	1	2	3
c_s	8490	1483	5640
ρ	2331	998.2	2230

Table 5.1: The material parameters for the three different domain groups.

Hence, the leftmost domain receives the parameters of Silicon, the middle domain becomes water, and the rightmost domain becomes pyrex. We follow the same procedure when assigning boundary conditions. First, in line 24 we define three boundary groups. Then in line 25 the groups are distributed. When doing eigenfrequency analysis, three different boundary conditions are available, the soft, the hard and the continuity condition. The soft condition imitates a soft wall, where the particles are free to oscillate back and forth. Hence, the soft boundary condition is defined as,

$$p_1 = 0. \tag{5.10}$$

To see how this relates to the particle velocity, we recall from Eq. (3.24) that for a time harmonic pressure we have $\varphi_1 = -ip_1/\rho_0\omega$. Hence, $\mathbf{u}_1 = \boldsymbol{\nabla}\varphi_1 = -i\boldsymbol{\nabla}p_1/\rho_0\omega$. The soft

condition therefore gives no constraints on $\mathbf{u}_1$. The hard condition imitates a hard wall, where the particle velocity is fixed to the steady wall. The hard boundary condition is defined as,

$$\mathbf{n}\cdot\boldsymbol{\nabla}\frac{p_1}{\rho_0} = 0. \tag{5.11}$$

This condition locks the particle velocity, but leaves no constraint on the pressure. The continuity condition simply states that both pressure and particle velocity must be continues across the boundary. The continuity condition can only be applied to internal boundaries. The question, that now remains, is how to distribute these three condition to the ten boundaries in our problem. First we notice that boundary 4 and 7 are internal boundaries. Hence, it is obvious that these should be of the continues type. Since we want to compare this system with one placed on top of a piezo element. The boundary facing the piezo is forced to move together with the piezo, hence boundary 1 should be of type hard. Since boundary 10 is supposed to be adjacent to normal air it should be free to move, and hence, be of the type soft. The remaining boundaries are all set to be of the hard type, as this makes the pressure constant across the boundaries. This mean that the system will act as one dimensional, as long as the shortest wavelength is more than twice of the height of the domains. The speed of sound is lower in water than in silicon and pyrex, so the smallest wavelengths will be in the water domain. We can therefore find the critical frequency as,

$$F_c = \frac{c_s}{2\lambda} \approx \frac{1500\,\mathrm{ms}^{-1}}{20\times10^{-6}\,\mathrm{m}} \approx 75\,\mathrm{MHz}. \tag{5.12}$$

This result is very important, as it tells us that all eigenfrequencies found to be more than 75 MHz are not valid. Line 25 distributes the boundary groups in the following way:

Boundary type	Hard (SH)	Soft (SS)	Continues (cont)
Boundary number	1, 2, 3, 5, 6, 8, 9	10	4, 7

Table 5.2: The distribution of the boundary conditions. The letters in the parenthesis are the abbreviations used in line 24.

Now the problem has been fully defined we begin to solve it. Before the actual solving step the FEM-structure must be prepared. This is done in line 27-28, where we use the functions 'multiphysics()' and 'meshextend()', which combines the defined physics applications with the defined mesh.

COMSOL

```
26 % Solving
27 fem=multiphysics(fem);
28 fem.xmesh=meshextend(fem);
29 fem.sol=femeig(fem, ...
30     'neigs',NSOL, ...
31     'shift',Lstart, ...
32     'solcomp',{'p'}, ...
33     'outcomp',{'p'});
```

COMSOL

In line 29 the eigensolver, `femeig()` is called. We use the argument 'neigs' to tell the solver how many solutions we are looking for. In this case we are looking for NSOL, which was set to four in line 4. The next argument is 'shift', which tells the solver where to begin the search for solution. Since we in this example wants the first four eigenvalues we set 'shift' to Lstart, which was set to 500 in line 5. Finally we tell the solver to solve for the specific variable , p, representing pressure. Finally we take a look at the results.

COMSOL

```
34 % Plotting
35 for j=1:length(fem.sol.lambda)
36     figure
37     postcrossplot(fem,1,[0 0.001;5e-6 5e-6], ...
38                 'lindata','p', ...
39                 'solnum',j);
40 end
41 (fem.sol.lambda.^0.5./(2*pi))'
```

COMSOL

The lines 35 and 40 starts and ends a loop, which is executed once for each found solution. The variable 'j' serves as a counter, hence, it refers to the current solution number. Line 36 creates a new figure window, to avoid the coming plots from overlapping each other. In line 37-39 we make a cross section plot of the pressure. The argument in square brackets is coordinates for the cross section. Since the simulation is supposed to be one dimensional the y-coordinates are unimportant as long as they are identical. The x-coordinates are 0 and 0.001. In line 38 we tell the plotter that it is the pressure we wish to see plotted. Line 39 makes sure we plot the j'th solution. Finally in line 41 we ask the script to compute and print the found eigenfrequencies. In Fig. 5.3 the output from the script is shown, however only the third solution-plot is shown.

Result

```
ans =

  1.0e+006 *

    0.4746
    3.5581
    5.5887
    6.7202
```

Result

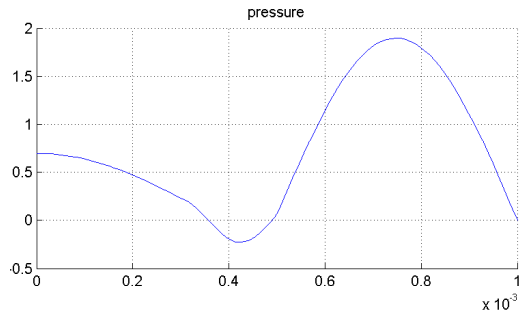

Figure 5.3: The left side of this figure shows the output of the script, while the right side shows a cross section plot of the pressure distribution corresponding to the third eigenfrequency. The four found eigenfrequencies are 0.47 MHz, 3.56 MHz, 5.59 MHz and 6.72 MHz.

When using the eigenfrequency analysis we must be aware that there might be solutions, which has not been found, and a second execution of the script may yield a different result. This problem seems only to apply to the ends of the eigenvalue list. So for any other purposes than this example the number of eigenvalues sought should be large enough to allow the exclusion of a few values at each end of the list. If the list starts at zero, as in this example, the first eigenvalues should all be found. Notice that the second eigen-

frequency corresponds to the one shown in Fig. 4.3 panel (c), while we will look at the third resonance in the next subsection.

5.1.3 The time harmonic solver

To see how the pressure will distribute in our sandwich structure for any given frequency, we must make a time harmonic analysis. For this analysis we add a new domain to the right side of the geometry from the eigenfrequency analysis. This domain represent the ambient air. The governing equations for time harmonic analysis is the same, however a few more boundary conditions are added. When loading the acoustic module, COMSOL will select the harmonic analysis by default, hence, the line `fem.appl.prop.analysis='eigen';` must be omitted. In this analysis we include two new boundary conditions, one to describe how the piezo element(not included in model) effects the adjacent boundary, and one to describe how the sound waves leak to the surroundings. To model a vibrating piezo element we use the normal acceleration boundary condition.

$$\mathbf{n}\cdot\boldsymbol{\nabla}\frac{p_1}{\rho_0} = \mathbf{a}_n. \tag{5.13}$$

Fortunately, we have already determined the inward acceleration, $\mathbf{a}_n$. From Eq. (4.2) we have $\mathbf{a}_w = -i\ell\omega^2\mathbf{n}e^{-i\omega t}$, where ℓ is the amplitude of the piezo, and ω is the angular frequency. When choosing ω we must be sure to stay below the critical frequency, since our model still is pseudo-one-dimensional. To implement the normal acceleration boundary condition the type abbreviation `'NA'` is used. The acceleration is introduced with the line `bnd.nacc = a;`. To model the leakage of sound waves, we use the impedance boundary condition

$$\mathbf{n}\cdot\boldsymbol{\nabla}\frac{p_1}{\rho_0} - \frac{i\omega p_1}{Z} = 0. \tag{5.14}$$

The origin of this equation is the same assumption as we used in Section 4.3, which was that there should be no reflected wave, $D_l = 0$. This can be seen by remembering that the wave, in domain D has the form $p_{1,D}(x,t) = D_r e^{i(k_D x-\omega t)} + D_l e^{i(-k_D x-\omega t)}$. We then perform the following manipulation,

$$\mathbf{n}\cdot\boldsymbol{\nabla}\frac{p_1}{\rho_0} - \frac{i\omega p_1}{Z} = 0, \tag{5.15}$$

$$\partial_x\left(\frac{D_r e^{i(k_D x-\omega t)}}{\rho_0} + \frac{D_l e^{i(-k_D x-\omega t)}}{\rho_0}\right) - \frac{i\omega D_r e^{i(k_D x-\omega t)}}{Z} - \frac{i\omega D_l e^{i(-k_D x-\omega t)}}{Z} = 0, \tag{5.16}$$

$$\frac{ik_D D_r e^{i(k_D x-\omega t)}}{\rho_0} - \frac{ik_D D_l e^{i(-k_D x-\omega t)}}{\rho_0} - \frac{i\omega D_r e^{i(k_D x-\omega t)}}{Z} - \frac{i\omega D_l e^{i(-k_D x-\omega t)}}{Z} = 0. \tag{5.17}$$

We then use $k = w/c$ and $Z = \rho_0 c$

$$\frac{i\omega D_r e^{i(k_D x-\omega t)}}{Z} - \frac{i\omega D_l e^{i(-k_D x-\omega t)}}{Z} - \frac{i\omega D_r e^{i(k_D x-\omega t)}}{Z} - \frac{i\omega D_l e^{i(-k_D x-\omega t)}}{Z} = 0, \tag{5.18}$$

$$-2\frac{i\omega D_l e^{i(-k_D x-\omega t)}}{Z} = 0, \tag{5.19}$$

$$D_l = 0. \qquad (5.20)$$

The impedance boundary condition has the type abbreviation `'IMP'`. The impedance is introduced by the line `bnd.Z={'343.4*1.161'};`. With this condition the pressure wave will stream away from the structure as it would from a speaker. With these new boundaries at each end, we can now numerically solve the same time harmonic system that we already have solved analytically. The frequency, `f` is defined using the line `appl.var = {'freq','f'};`. Instead of the eigensolver the linear solver, `femlin()` is used, and the arguments, `neigs` and `shift` are dropped(see Appendix B). By doing the same calculation by both analytical and numerical methods, we have the possibility of validating the numerical algorithm. In Fig. 5.4 both the numerical and analytical result for the resonance frequency 5.5887 MHz is plotted. As it can be seen from the figure the two results are very similar. In order to get a better impression of the difference between the two, the absolute difference is plotted in Fig. 5.5. The largest difference is approximately 3800 Pa, but this should be compared to values of the results, which are of the order of several billions (10^9) Pa. By comparing these numbers, we see that the error is only of the order of $\approx 10^{-6}$. The same analysis is repeated for the non-resonance frequency 5.6887 MHz. In Fig. 5.6 both results are shown. The difference between these two is shown in Fig. 5.7. This time the largest difference is approximately 1.3 Pa. This error is also $\approx 10^{-6}$. From the size of these errors, we can conclude that the numerical model is sufficiently valid. Furthermore, due to large increase in pressure amplitude, we have confirmed that the frequency 5.5887 MHz is in fact very close to a resonance, had we hit the exact resonance the amplitude would become infinite. This proves that also the eigenfrequency analysis is sufficiently correct. We now understand the basics of the acoustic module and can in Chapter 6 move on to complicated geometries, which cannot be solved analytically.

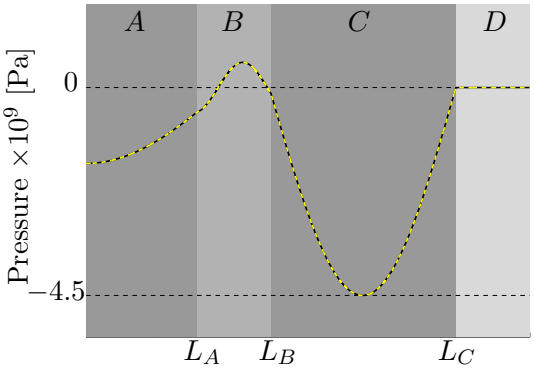

Figure 5.4: The results of a calculation performed both numerically(black) and analytically(yellow). The calculation shows the pressure distribution at the resonance frequency 5.5887 MHz.

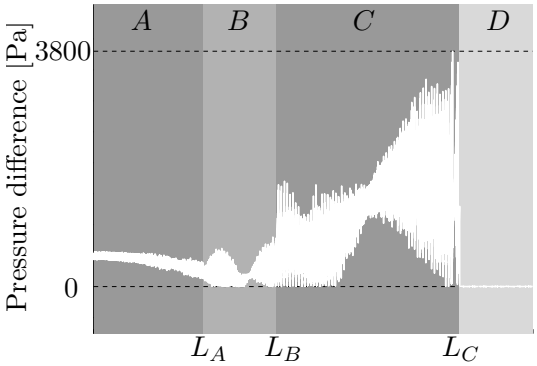

Figure 5.5: The absolute difference between the analytical and numerical results at the resonance frequency 5.5887 MHz. The error is approximately $\approx 10^{-6}$.

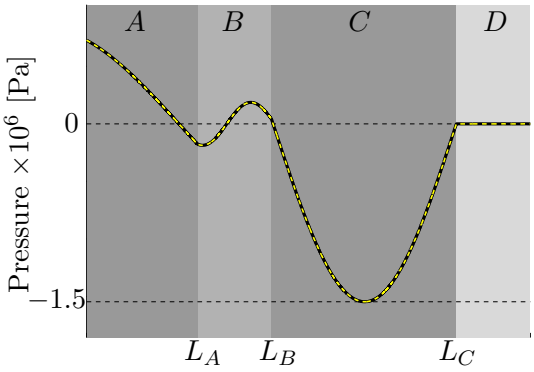

Figure 5.6: The results of a calculation performed both numerically(black) and analytically(yellow). The calculation shows the pressure distribution at the non-resonance frequency 5.6887 MHz.

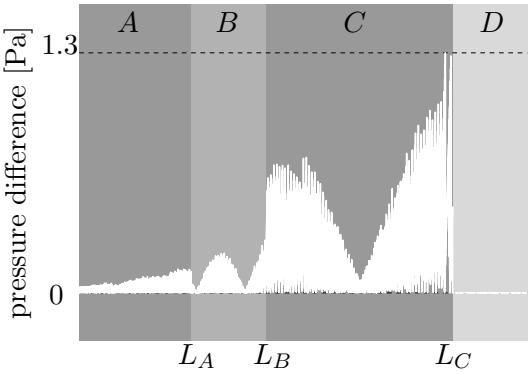

Figure 5.7: The absolute difference between the analytical and numerical results at the non-resonance frequency 5.6887 MHz. The error is approximately $\approx 10^{-6}$.

5.2 General PDE formulation for COMSOL

In Chapter 3 we derived three equations necessary for finding $\mathbf{u}_2''$. The three partial differential equations we wish to solve using COMSOL, are the compressible continuity equation Eq. (3.61)

$$\partial_x u_2'' + \partial_y v_2'' = S \tag{5.21}$$

and the x and y components of the steady-state Navier-Stokes equation Eq. (3.62)

$$\eta\nabla^2 u_2'' = \partial_x p_2'' + F_x'' - \beta\eta\partial_x\Big(\partial_x u_2'' + \partial_y v_2''\Big) \tag{5.22}$$

$$\eta\nabla^2 v_2'' = \partial_y p_2'' + F_y'' - \beta\eta\partial_y\Big(\partial_x u_2'' + \partial_y v_2''\Big) \tag{5.23}$$

where S, F_x'' and F_y'' are known functions of both x and y. These three equation each has an associated dependent variable. The continuity equation has p_2'' ($\partial_t p_2'' + \boldsymbol{\nabla}\cdot J_2'' = 0$), and the x and y component of the Navier-Stokes equation has u_2'' and v_2'', respectively. Hence, we have the three dependent variables $a = \{u_2'',\ v_2''$ or $p_2''\}$. Each of the three equations Eqs. (5.21 - 5.23) must be formulated using the general PDE formulation,

$$\boldsymbol{\nabla}\cdot\boldsymbol{\Gamma}_a = f_a. \tag{5.24}$$

where all terms containing the associated dependent variable, a, are collected in the vector $\boldsymbol{\Gamma}_a$. All other terms are listed in the scalar f_a

$$\boldsymbol{\Gamma}_{p_2''} = \begin{pmatrix} 0 \\ 0 \end{pmatrix}, \qquad f_{p_2''} = -(\partial_x u_2'' + \partial_y v_2'') + S \tag{5.25}$$

$$\boldsymbol{\Gamma}_{u_2''} = \begin{pmatrix} (\beta+1)\eta\partial_x u_2'' \\ \eta(\partial_y u_2'' + \beta\partial_x v_2'') \end{pmatrix}, \qquad f_{u_2''} = \partial_x p_2'' + F_x'' \tag{5.26}$$

$$\mathbf{\Gamma}_{v_2''} = \begin{pmatrix} \eta(\partial_x v_2'' + \beta\partial_y u_2'') \\ (\beta+1)\eta\partial_y v_2'' \end{pmatrix}, \qquad f_{v_2''} = \partial_y p_2'' + F_y'' \tag{5.27}$$

In the general PDE formulation, the boundary conditions are defined as a combination of a Dirichlet and a Neumann condition

$$-\mathbf{n}\cdot\mathbf{\Gamma}_a = G_a + \mu\Big(\partial_a R_a\Big)^T; \qquad R_a = 0, \tag{5.28}$$

where a is the dependent variable associated to $\mathbf{\Gamma}_a$, μ is the Lagrange multiplier and G_a and R_a are to be specified. $\mathbf{n}$ is normal vector of the boundary. If we define $R_a \equiv 0$, then the term $\partial_a R_a$ becomes zero, and since the Dirichlet condition $(0 = 0)$ does not contribute with any restraints, the only remaining condition is the Neumann condition

$$-\mathbf{n}\cdot\mathbf{\Gamma}_a = G_a. \tag{5.29}$$

If we instead define R_a, for instance $R_a \equiv a - 4$, so the term $\partial_a R_a$ differs from zero, then the Lagrange multiplier can be scaled to achieve any desired value. Hence the entire Neumann condition can be discarded and any definition of G_a becomes obsolete. The only remaining condition is the Dirichlet condition $a - 4 = 0$ or

$$a = 4. \tag{5.30}$$

If we define $R_a \neq 0$ such that $\partial_a R_a = 0$ we get both Dirichlet and the Neumann condition. For internal boundaries the definition is slightly different

$$-\mathbf{n}\cdot(\mathbf{\Gamma}_{a,1} - \mathbf{\Gamma}_{a,2}) = G_a + \mu\Big(\partial_a R_a\Big)^T; \qquad R_a = 0; \qquad a_1 = a_2, \tag{5.31}$$

where the numeric subscripts refer to the two adjacent domains divided by the boundary. We notice that this condition requires the dependent variable to be continues across the boundary (see Appendix D).

5.3 Executing a COMSOL-script

To execute a COMSOL-script, both Matlab and COMSOL must be installed. The programs are simultaneously initiated by the command

`C:\COMSOL32\bin\comsol.exe matlab`.

This command will most likely already exist as a shortcut in the 'programs'-folder. When the programs are up and running, the script can be entered into the Matlab-editor. Once the script has been entered, it can be executed by hitting the "F5"-button. A selected part of the script can be executed by the "F9"-button.

Chapter 6

The acoustic radiation force

6.1 The force in one dimension

When a microfluidic channel is affected by a standing acoustic wave, any suspended particles will be affected by a force called the 'acoustic radiation force', $\mathbf{F}_{ar}$. The induced force will move particles towards either pressure nodes or anti-nodes. The acoustic radiation force is commonly [16] quoted in one dimension as

$$F_{ar} = -\left(\frac{\pi \widehat{p}_1^2 V_p}{2\lambda}\right)\phi(\beta,\rho)\sin(2kd) \tag{6.1}$$

where

$$\phi(\beta,\rho) = \beta_l \frac{5\rho_p - 2\rho_l}{2\rho_p + \rho_l} - \beta_p \tag{6.2}$$

and

$\widehat{p}_1$	=	Pressure amplitude.
V_p	=	Volume of the particle.
d	=	Distance from closest pressure node(p_1).
λ	=	Wavelength of the acoustic wave.
k	=	$\frac{2\pi}{\lambda}$
β_l, β_p	=	Compressibility of either the liquid or the particle.
ρ_l, ρ_p	=	Density of either the liquid or the particle.

By looking at Eq. (6.1) it is clear that once the standing wave is achieved, several different factors has influence on the size of the force. First of all the pressure amplitude, this can somewhat be controlled by the tone generator connected to the piezo element and by ensuring that the element is properly connected to the chip, but it is mainly a matter of how perfect a resonance is achieved. The second factor is the volume of the particles, it simply implies that the larger a particle; the greater the force(more on this in Chapter 8). Note that the particles must be smaller than half of the wavelength. The third factor is the wavelength, since the force decreases as wavelength increases, higher frequencies yields higher force. The fourth factor is $\phi(\beta,\rho)$, this factor is determined by the characteristics

of the particles in use. The factor can either be positive, negative or zero. If ϕ is zero, the particles are unaffected by the acoustic waves. It is because of the sign-change in the ϕ-factor that blood cells and lipid particles moves in opposite directions[18]. See Fig. 6.1.

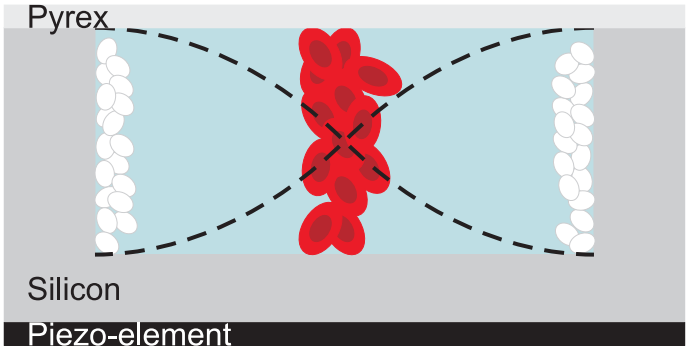

Figure 6.1: The Piezoelement creates a standing wave inside the channel. Depending on their density or compressibility, particles will either move towards the center of the channel, or towards the sidewalls. Blood cells gather in the center while lipid particles gathers at the walls.

6.2 The force in more dimensions

If the method described above should be used for non-planar waves, we can only say that particles will eventually end up in pressure nodes or anti-nodes. So by solving the Helmholtz equation Eq. (5.1) we can find the different eigenmodes and the corresponding nodes. Hence, we can (in principle) calculate where the beads will accumulate for different frequencies. How fast the particles will move in different parts of the chamber, can not be determined.

A way to predict the shape of the multi-dimensional acoustic radiation force, is to look at the elastic energy. We regard the particles as springs governed by Hooke's law ($F_h = -k_s x$). The potential energy in such systems is found as

$$E_{pot} = \frac{1}{2}k_s x^2 = \frac{1}{2}\frac{F_h^2}{k_s} = \frac{1}{2}\frac{A^2(p_2'')^2}{k_s} \tag{6.3}$$

where A is the area of the particle, and $p = p_2''$, where $p_2''(\mathbf{r}) > 0$ as other contributions are constant or has zero time average. The force acting on a particle can then be found as

$$\mathbf{F}_{ar} = -\boldsymbol{\nabla} E_{pot} = -\frac{1}{2}\frac{A^2}{k_s}\boldsymbol{\nabla}(p_2'')^2 = -\tau p_2''\boldsymbol{\nabla} p_2'' \tag{6.4}$$

where τ is constant in both space and time, but different for different types of particles. The value of τ is not straight forward to find, so in this work we simply define it as positive for blood cells. As a consequence we can still only calculate the relative acoustic radiation force. We do notice that $\tau \propto A^2 \propto r^4$, where r is the radius of the particle. Hence, particles with a radius 10 times larger, will be 10000 times more affected by the acoustic radiation force. Unfortunately the calculation of p_2'' is not straight forward. So until Chapter 8 we will stick to finding nodes for eigenmodes.

6.3 Dimensional analysis; from 3D to 2D

The obvious way to calculate the resonance pressure field, is a three dimensional eigenfrequency analysis. When trying to model the chip presented in Section 1.3.1 in three dimensions, it proved to be a complicated matter to define the mesh. Usually a mesh of isotropic tetrahedron is used. However, this is not a possibility because of the Length:width:height ratio being 47:15:1, meaning that if we wish to have 15 elements in the height, which still is a rather low resolution, we would end up with approximately $(15\times1)\times(15\times15)\times(15\times47) \approx 2.4 \times 10^6$ elements. With so many elements the calculation would require far more physical memory than is found in a standard computer. So, in order to obtain anisotropic elements we must use an extruded mesh of quadrilaterals. The extrusion, however, forces us to model each layer independently, in order to define several different domains in the z-direction. The three layers are then connected using 'Identity Boundary Conditions'. However, it quickly proved that also this combination of still many elements and the identity boundary conditions, also required far too much computational power. This meant that it would be necessary to figure out if the calculations could be made in only two dimensions.

6.3.1 Validation of the 2D approximation

Instead of doing the calculation i three dimension it is suggested, that due to the relative low frequency(or long wavelengths) we can neglect the z-direction, and perform the calculation on a two dimensional cross section of the second layer. In order to validate the results of a two dimensional approximation, a new geometry was invented(only for simulation purposes). The plan was to simplify the geometry so much that it would be possible to perform full three dimensional simulations. The results of the two- and three dimensional simulations could then be compared. The new geometry took root in the old one. The chamber was kept at $2\,\text{mm}\times2\,\text{mm}$ while the channel was shorted down, so it only extended 2.4 mm on each side of the channel. The distance from the end of the channel to the edge of the chip was shortened to 0.6 mm, giving the new chip a total length of only 8 mm. The distance from the chamber to the edge of the chip was shortened to 2 mm on each side. Hence, resulting in a total width of 6 mm. The Heights of the three layers were kept at original values. By cutting down the chip size three dimensional eigenfrequency analysis became possible, but only for a very coarse mesh. When doing finite element simulations it is very important to keep the wavelengths larger than the mesh size, otherwise the problem cannot be well defined. Hence, in order to keep the wavelengths long enough, we only calculate the first 49 eigenfrequencies. The new smaller geometry is converted into two dimensions and solved using the same coarse mesh. Since we do not expect the solutions to be in the exact same order in two and three dimensions, we calculate the first 50-two dimensional eigenfrequencies. To compare the calculated pressure fields, a cross section in the xy-plane in the middle of the chamber were visually compared. Only the 50th two-dimensional solution could not be matched. Had the three dimensional analysis reached further a matching solution might have been found. Hence, the 50th solution is discarded. In Fig. 6.2 the results from the three dimensional calculation have been plot-

ted(with a blue 'x'). In the same figure the results from the two dimensional calculation, which had a similar pressure field to one of the three dimensional solutions, have also been plotted(with a red 'o'). In Fig. 6.3 the solutions are sorted based on the two dimensional solutions. From the lack of gaps in these two figures we can conclude that for low frequencies, the same pressure fields exist for both the two and three dimensional geometries. Furthermore, the shift between two frequencies, corresponding to the same pressure field, is almost constant at 0.5 MHz.

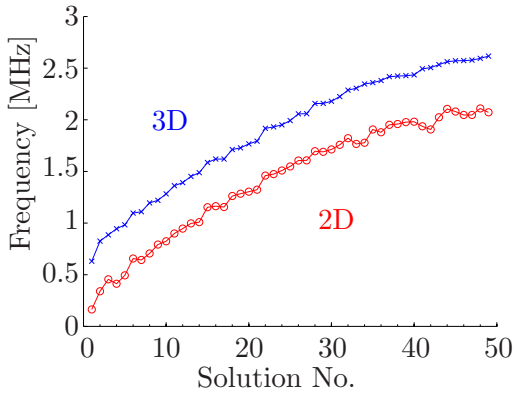

Figure 6.2: Both 2D and 3D solutions sorted based on the three-dimensional solutions. The lack of gaps in the two-dimensional solutions indicate that all calculated three-dimensional pressure fields were also found in the two dimensional calculation.

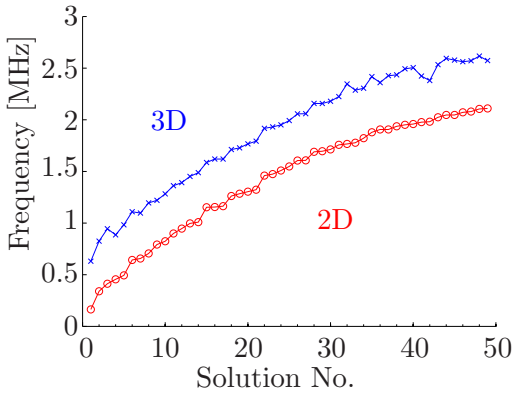

Figure 6.3: The figure show both 2D and 3D solutions sorted based on the two dimensional solutions. The lack of gaps in the three dimensional solutions indicate that all calculated two dimensional pressure fields were also found in the three dimensional calculation.

This shows us that even though there is a shift in frequency, all pressure fields can be found from the two dimensional analysis as long as the frequency is low enough to prevent waves in the z-direction.

6.3.2 Density of states

The curves in Figs. 6.2 and 6.3 can be approximated analytically by assuming we only have one domain, where the speed of sound is an average value of those otherwise present. From the analytical solution (Eq. (5.7)) we have the relation

$$\omega^2 = c_s^2 \pi^2 \left(\frac{n^2}{a^2} + \frac{m^2}{b^2} + \frac{l^2}{c^2} \right). \tag{6.5}$$

From this equation we calculate the frequency for any integer combination of n, m and l. The results are sorted in increasing order and plotted in Fig. 6.5 as 'analytical fit'. Furthermore we can approximate this by rewriting Eq. (6.5) as

$$\frac{\omega^2}{c_s^2} = \mathbf{k}^2, \tag{6.6}$$

where $\mathbf{k}$ is defined as

$$\mathbf{k} = (k_x, k_y, k_z) = \left(\frac{\pi n}{a}, \frac{\pi m}{b}, \frac{\pi l}{c} \right). \tag{6.7}$$

Hence,

$$\frac{\omega}{c_s} = |\mathbf{k}|. \tag{6.8}$$

To find the number of solutions below a given frequency, we divide the area/volume of the circle/sphere with radius $|\mathbf{k}|$, by the area/volume of a single solution. In Fig. 6.4 the two dimensional analogy is shown.

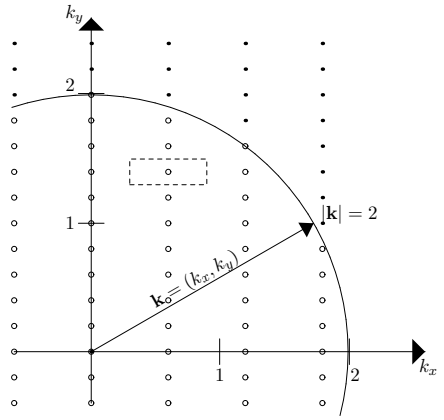

Figure 6.4: The definition of $\mathbf{k}$, which can be used to determine the density of states. For enhanced visibility only the two dimensional case is shown.

Hence, we find the number of solutions to be

$$N_{3D}(f) = \frac{V_{sphere}}{V_{sol}} = \frac{\frac{4}{3}\pi|\mathbf{k}|^3}{\frac{\pi}{a}\frac{\pi}{b}\frac{\pi}{c}} = \frac{4\ (2\pi f)^3\ a\ b\ c}{3\ c_s^3\ \pi^2}. \tag{6.9}$$

By turning this equation around we can predict the frequency of the N'th solution,

$$f_{3D}(N) = \frac{c_s}{2\pi}\sqrt[3]{\frac{3\pi^2}{4}}\sqrt[3]{\frac{N}{abc}}. \tag{6.10}$$

The same procedure is valid for two dimensional problem.

$$N_{2D}(f) = \frac{A_{circle}}{A_{sol}} = \frac{\pi|\mathbf{k}|^2}{\frac{\pi}{a}\frac{\pi}{b}} = \frac{(2\pi f)^2\ a\ b}{c_s^2\ \pi}. \tag{6.11}$$

$$f_{2D}(N) = \frac{c_s}{2\pi}\sqrt{\frac{N\pi}{ab}} \tag{6.12}$$

We then plot the frequency as a function of the solution number, for both the two and three dimensional analysis, together with the simulation results. For the analytical solutions the speed of sound have been fitted to fit the simulations. The reason for this is that there does not seem to be an obvious way to estimate the speed of sound. We could have used the sum of the speeds in each domain and divide by the number of domains. However, we must also take into account that each speed should be weighted by the relative size of

the corresponding domain. Furthermore, domains with a low speed of sound, will support more solutions, and should somehow be emphasized. From Fig. 6.5 it is seen that the shape of the analytical approximations are relatively close to the simulation results. This indicate the applied eigenfrequency solver have not skipped any solutions, nor has it found artificial solutions originating from bad meshing amongst other modeling features.

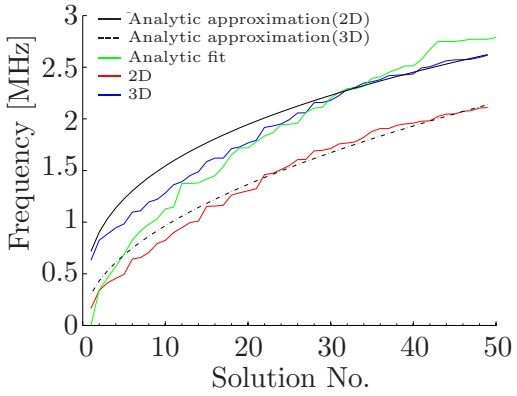

Figure 6.5: Comparison of the analytical eigenfrequencies to those from the simulations. For the 3D and 2D approximations and the analytical fit we used $c_{3D} = 8400\text{m/s}$, $c_{2D} = 7500\text{m/s}$ and $c_{Fit} = 5250\text{m/s}$

We have now shown that as long as we stick to low frequencies all pressure fields can be found using only a two dimensional analysis. Furthermore, the $f(N)$-curves follow those analytically predicted. Hence, we can generalize these conclusions to also apply for the original geometry shown in Fig. 1.1. Should this generalization be valid, we are now able to simulate the pressure fields inside the real chip.

6.4 The symmetric chamber model

In Section 6.3 we have shown that it is sufficient to perform the simulations in only two dimensions. However, the two original chips used in the experiments, were designed for easy fabrication and handling. At that time it was not considered to design the chips with a geometry, which could easily be remodeled. This meant that parts of the chips easily broke off leaving unpredictable shapes. Hence, the simulated geometries should not be considered exact replicas, but rather geometric approximations. Since the geometry will not be exact anyway, we look at the simplest working approximation. The large difference in the acoustic impedance between silicon and water,

$$\frac{Z_w}{Z_{si}} = \frac{c_w \rho_w}{c_{si} \rho_w} = \frac{1483\ \text{m s}^{-1} \times 998.2\ \text{kg m}^{-3}}{8490\ \text{m s}^{-1} \times 2331\ \text{kg m}^{-3}} = 0,075 \tag{6.13}$$

allows us to treat the water/silicon interface as a hard wall. Hence, we can discard the silicon domain and only simulate the domains containing liquid. Hence, we rather discard the silicon domain that simulate it using wrong dimensions. By this approximation the geometry simplifies to a 2 mm $\times$ 2 mm chamber, centered on a 25 mm $\times$ 0.4 mm channel

(see Fig. 6.6). The boundary conditions are set to hard wall, $\mathbf{n}\cdot\boldsymbol{\nabla}p_1 = 0$, except at the two ends of the channel were we set $p_1 = 0$ to mimic the in- and outlets. This geometry will here forth be called the symmetric chamber model.

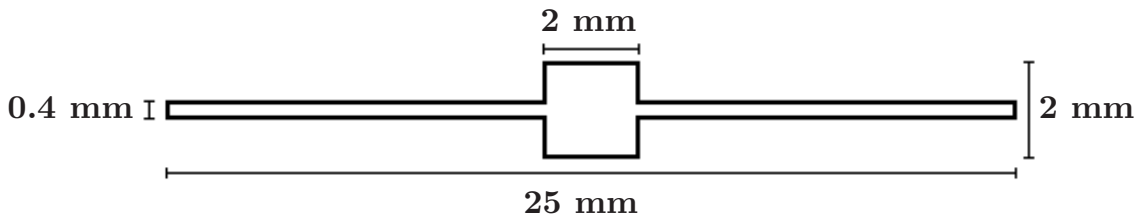

Figure 6.6: The chamber model

The system could of cause be approximated even further, by simply simulating the chamber itself, but this have proved to be too rough an approximation, as the found eigenmodes could not be experimentally confirmed.

The result of the simulations(see Appendix C) on both the square and the circular symmetric chamber model yielded several hundreds of eigenmodes in the frequency range 0.5 MHz − 3 MHz, from which only a small fraction could be experimentally verified. It is difficult to predict which of the calculated eigen-modes will be possible to determine experimentally, as the pressure field amplitude is normalized to fulfill

$$\frac{\int_\Omega p_1^2 \,\mathrm{d}x\,\mathrm{d}y}{\int_\Omega 1 \,\mathrm{d}x\,\mathrm{d}y} = 1. \tag{6.14}$$

However, if the calculation shows a much higher amplitude in the chamber than in the channel, the probability of experimentally observing this mode is greatly increased. Some of the results are shown in Fig. 6.7. Notice that the shown examples have been chosen based on their geometric differences, and not based on the quality of the frequency match.

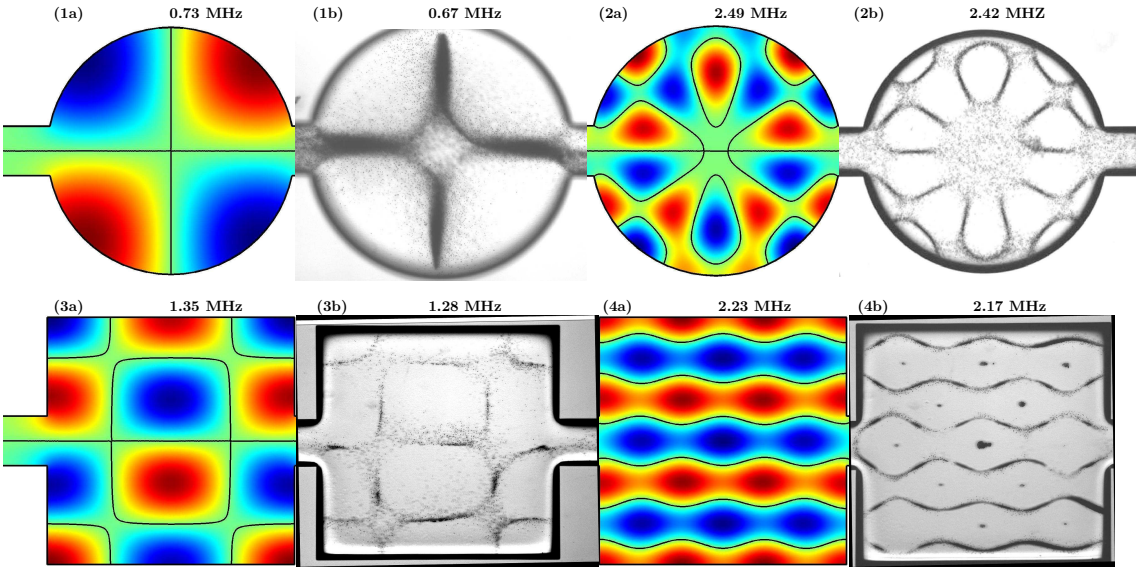

Figure 6.7: Four examples of how the simulated eigenmodes can be confirmed by experiments. The top row is from a chip with a round chamber, while the bottom row is a square chamber. We see that the simulated frequencies does not match the experimental ones completely. Panel (2b) courtesy Melker Sundin.

Fig. 6.7 compares the simulated eigenmodes with the experimental obtained bead patterns. An important lesson learned from studying these pictures, is that the beads not only accumulate at the nodal-lines, but seems to be more confined to the nodal-line the steeper the gradient of eigenmode pressure field is at that location. This is especially clear in panel (1b) and (2b) but can also be seen in panel (3b) This strongly indicates that the definition of the acoustic radiation force, $\mathbf{F}_{ar}$, should include a term dependant on the spatial derivative of p. We notice this is not the case in Eq. (6.1) but in Eq. (6.4). When looking at panel (4b) we see that some beads have accumulated at the pressure extremes. These are in fact a different kind of beads than the blood cell phantoms, and apparently these other beads have an opposite compressibility ratio than blood cells. ($\tau < 0$ in Eq. (6.4)). An important feature not revealed by Fig. 6.7 is the strength of the acoustic radiation force. In panel (1b) and (3b) the force was extremely weak, while a little stronger in panel (2b). In the final case of panel (4b) the force was many times stronger than in other eigenmodes. The pattern formed at 2.17 MHz was the only observed pattern strong enough to withstand a flow through the chamber. All other patterns were immediately washed away. We notice that there seems to be a small offset between the calculated frequencies and the corresponding experimental ones. This offset might be caused by variations in the temperature during the experiments. Despite the small deviation in frequency the simulations are very precise for describing where the beads will accumulate.

6.5 Breaking of symmetry

Since the original chips were asymmetric, some of the experimentally observed eigenmodes also were. These eigenmodes can not be explained from the symmetric chamber model,

so to ensure our understanding we must expand the model. In reality the chambers were placed off center relative to the channel on both chips. Furthermore the channel/chamber region was shifted in both x- and y-direction, also on both chips. All these shifts could of cause be implemented at once, but it proved very difficult to estimate the correct lengths of these shifts. This meant that only some of the experimentally observed eigenmodes could be found for a set of shift-length-parameters. So instead of wasting time searching for the exact values of the parameters, it was decided to just break the symmetry in a simple way. There are two obvious ways to bring asymmetry into the system (see Fig. 6.8).

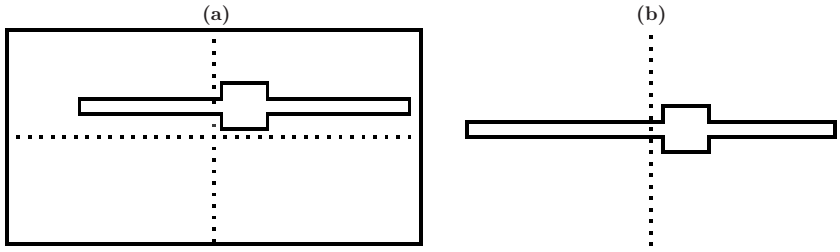

Figure 6.8: Two simple ways of introducing asymmetry to the model. In panel (a) the chamber/channel part has been shifted as a whole. This method requires that the surrounding silicon is also simulated. In panel (b) the chamber has been shifted relative to the channel. The dotted line indicate former symmetry lines.

One way is to simulate the surrounding silicon in which both the channel and chamber both has been shifted slightly, or a second and easier way is to shift the location of the chamber relative to the channel. In Fig. 6.9 we compare the experimental patterns with those achieved using the two asymmetric models. Panel (a) and (b) shows the asymmetric patterns corresponding to 2.06 MHz and 2.08 MHz, respectively. We notice how the left side appear strongest in panel (a) and the right one in panel (b). Panel (c) and (d) shows the corresponding results from simulations on the asymmetric model where silicon surrounds the liquid region. The liquid region is shifted 0.5 mm right and 0.5 mm up. The difference in frequency between panel (c) and (d) is only 1 kHz. When we compare panel (c) and (d) to panel (a) and (b), we notice how the blue(low) areas just left and right of the red(high) center peak is of different strengths. In panel (c), as well as in panel (a) we see that left side is the strongest. In panel (d) and (b) it is the other way around. Hence, the method of applying an asymmetric silicon part around the chamber is sufficient to account for the split eigenmode.

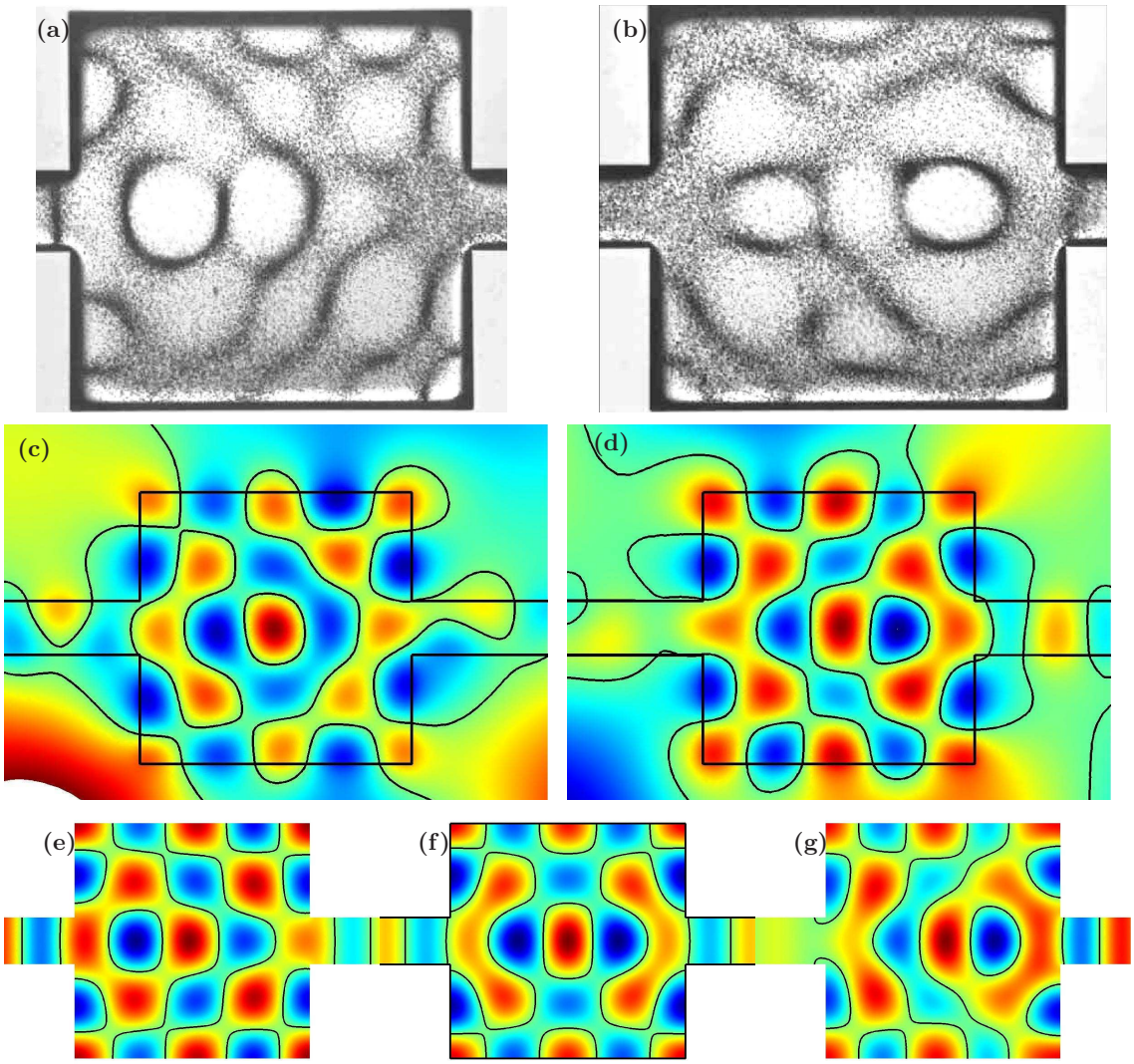

Figure 6.9: Panel (a) and (b) shows the asymmetric patterns corresponding to 2.06 MHz and 2.08 MHz, respectively. Panel (c) and (d) shows the corresponding results from simulations on the asymmetric model where silicon surrounds the liquid region. The liquid region is shifted 0.5 mm right and 0.5 mm up. The difference in frequency between panel (c) and (d) is only 1 kHz. Panel (e) and (g) shows the result of shifting the otherwise symmetric placed chamber 1 mm to the right. The frequency difference is 28 kHz. Panel (f) shows the corresponding symmetric solution. Panel (a) and (b) courtesy Melker Sundin.

Panel (e) and (g) shows the result of shifting the, otherwise symmetric placed, chamber 1 mm to the right relative to the channel. The frequency difference between panel (e) and (g) is 28 kHz. Panel (f) shows the corresponding symmetric eigenmode solution. By comparing the nodal lines(black) in panel (e) and (g) to the experimental bead patterns, we can see that this very simple approach also can explain the eigenmode splitting.

6.6 Concluding remarks

We have shown that for a relatively shallow chamber, it is sufficient to find the eigenmodes for the governing Helmholtz equation in two dimensions instead of three, as long as the wavelength is more than twice the length of the third dimension. One consequence of using the Helmholtz equation for unattenuated waves is that simulations yields far more solutions than can be experimentally verified. This can be explained by arguing that, in the laboratory, acoustic damping in the liquid and any energy dissipation will smear out the theoretically perfect peaks. Hence, some modes will entirely disappear, while others might be clouded by stronger modes. The mismatch in frequency between experimental and calculated values, can be related to geometric uncertainties and thermally induced changes to material parameters.

Furthermore it has been shown that it is not necessary to include the material surrounding the chamber and channel (silicon in this case), as long as there is a large acoustic impedance mismatch.

It has also been shown that if the symmetry is broken the eigenmodes will spilt up.

So finally it can be concluded that the chamber model is very effective, when calculating where beads will accumulate.

Chapter 7

Examples of sound absorption in liquids

In this chapter we will look at some examples of how to calculate the second-order terms from Section 3.3.3. We start with two one-dimensional systems and finally in Section 7.3 we look at a two-dimensional system. In each example we calculate the first-order terms before we can find the second-order terms.

7.1 Analytic Example 1: plane traveling wave

In the first example we study a liquid under influence of a plane harmonic traveling wave. The wave is created by a oscillating wall at $x = 0$. Where the positive half space is containing the liquid. This system can be regarded as one dimensional. $k_0 = \omega/c_0$ and γ is the viscous damping parameter.

7.1.1 First order pressure, p_1, and velocity u_1

Since we prefer to use a steady coordinate system, we model the oscillation of the wall by stating that the flux at $x = 0$ is oscillating with the angular frequency $\omega \approx 10^6$ s^{-1} and the amplitude $\ell \approx 10^{-9}$m.

$$J_1(x,t) = \rho_0 u_1 = \rho_0 \omega \ell e^{-i\omega t}. \tag{7.1}$$

Hence, we may assume the velocity field, u_1, and the pressure field p_1 has the form

$$u_1(x,t) = \omega \ell e^{\varphi(x,t)}, \tag{7.2}$$

and

$$p_1(x,t) = \frac{\widehat{p}_1}{\omega \ell} u_1(x,t) = \widehat{p}_1 e^{\varphi(x,t)}, \tag{7.3}$$

where

$$\varphi(x,t) = (i - \gamma)k_0 x - i\omega t, \tag{7.4}$$

and

$$\gamma = \frac{(\beta + 1)\omega\eta}{2\rho_0 c_0^2}. \tag{7.5}$$

We note that Eq. (7.3) already fulfills the one dimensional edition of Eq. (3.51)

$$\partial_x^2 p_1 = -k_0^2 \Big[1 + i\gamma\Big]^2 p_1. \tag{7.6}$$

To find $\widehat{p}_1(x)$, we insert u_1 and p_1 into the one dimensional edition of Eq. (3.47)

$$\partial_x^2 u_1 = -i\frac{\omega\rho_0}{\eta}u_1 + \Big[1 - i\frac{\omega\eta\beta}{\rho_0 c_0^2}\Big]\frac{1}{\eta}\partial_x p_1, \tag{7.7}$$

we find

$$\widehat{p}_1 = \big[1 + i\gamma\big]\rho_0 c_0 \omega \ell. \tag{7.8}$$

To summarize the first order terms we got

$$u_1(x,t) = \epsilon c_0 e^{\varphi(x,t)}, \tag{7.9}$$

$$p_1(x,t) = \widehat{p}_1 e^{\varphi(x,t)} = \epsilon(1 + i\gamma)\rho_0 c_0^2 e^{\varphi(x,t)}, \tag{7.10}$$

where we have introduced the perturbation parameter ϵ

$$\epsilon = \frac{\omega\ell}{c_0} \approx 10^{-6}. \tag{7.11}$$

We can now calculate the second order terms.

7.1.2 Second order pressure, p_2'', and velocity u_2''

We can now begin to solve the one dimensional editions of Eq. (3.61) and Eq. (3.62)

$$\partial_x u_2'' = -\frac{1}{2c_0^2\rho_0}\partial_x \mathrm{Re}\left[\tilde{p}_1\tilde{u}_1^*\right], \tag{7.12}$$

$$\begin{aligned}\eta\partial_x^2 u_2'' + \beta\eta\partial_x(\partial_x u_2'') &= \partial_x p_2'' + F'' \\ (\beta+1)\eta\partial_x^2 u_2'' &= \partial_x p_2'' + F''\end{aligned} \tag{7.13}$$

We insert the known first order terms into Eq. (7.12) and integrate to find u_2''

$$\begin{aligned}u_2'' &= -\frac{1}{2c_0^2\rho_0}\int\Big(\partial_x \mathrm{Re}\left[\tilde{p}_1\tilde{u}_1^*\right]\Big)\,\mathrm{d}x \\ &= -\frac{1}{2c_0^2\rho_0}\mathrm{Re}\left[\tilde{p}_1\tilde{u}_1^*\right] + C_u \\ &= -\frac{1}{2c_0^2\rho_0}c_0^3\epsilon^2\rho_0 e^{-2k_0\gamma x} + C_u \\ &= -\epsilon^2\frac{1}{2}c_0 e^{-2k_0\gamma x} + C_u.\end{aligned} \tag{7.14}$$

where C_u is an integration constant. Next we calculate F'' according to Eq. (3.38) in one dimension

$$\begin{aligned} F'' &= \frac{1}{2}\rho_0 \mathrm{Re}\big[\tilde{u}_1 \partial_x \tilde{u}_1^*\big] + \frac{1}{2}\rho_0 \mathrm{Re}\big[\tilde{u}_1 \partial_x \tilde{u}_1^*\big] \\ &= \rho_0 \mathrm{Re}\big[\tilde{u}_1 \partial_x \tilde{u}_1^*\big] \\ &= -\epsilon^2 \gamma c_0 \omega \rho_0 e^{-2k_0\gamma x}. \end{aligned} \tag{7.15}$$

We can now find p_2'' by inserting Eq. (7.14) and Eq. (7.15) into Eq. (7.13) and integrate

$$\begin{aligned} \partial_x p_2'' =& (\beta+1)\eta \partial_x^2 u_2'' - F'' \\ p_2'' =& \int \Big[(\beta+1)\eta \partial_x^2 u_2'' - F''\Big]\,\mathrm{d}x \\ p_2'' =& \epsilon^2 \gamma c_0 \omega \rho_0 \int \Big[(1-4\gamma^2)e^{-2k_0\gamma x}\Big]\,\mathrm{d}x \\ p_2'' =& -\epsilon^2 \frac{1}{2} c_0^2 \rho_0 (1-4\gamma^2) e^{-2k_0\gamma x} + C_p \end{aligned} \tag{7.16}$$

where C_p is an integration constant. Here we assume $C_p \equiv 0$.

We now calculate the time averaged flux J_2''. Keeping in mind that in a one dimensional system with one wall the time-averaged flux must be zero in steady state, otherwise some areas of the system would end up depleted.

$$J_2'' = \langle \rho_1 u_1 \rangle_t + \rho_0 u_2'' = 0. \tag{7.17}$$

We can quickly see that

$$\rho_0 u_2'' = -\epsilon^2 \frac{1}{2} c_0 \rho_0 e^{-2k_0\gamma x} + \rho_0 C_u. \tag{7.18}$$

and that

$$\begin{aligned} \langle \rho_1 u_1 \rangle_t =& \frac{1}{2}\mathrm{Re}\left[\frac{\tilde{p}_1}{c_0^2}\tilde{u}_1^*\right] \\ =& \epsilon^2 \frac{1}{2} c_0 \rho_0 e^{-2k_0\gamma x}. \end{aligned} \tag{7.19}$$

Hence, we find

$$J_2'' = -\epsilon^2 \frac{1}{2} c_0 \rho_0 e^{-2k_0\gamma x} + \epsilon^2 \frac{1}{2} c_0 \rho_0 e^{-2k_0\gamma x} + \rho_0 C_u = 0, \tag{7.20}$$

if $C_u = 0$. From Eq. (6.4) we have the acoustic radiation force

$$\begin{aligned} F_{ar} =& -\tau p_2'' \partial_x p_2'' \\ =& \frac{\epsilon^4 \gamma}{2} \tau \rho_0^2 c_0^3 (1-4\gamma^2) e^{-4k_0\gamma x} \end{aligned} \tag{7.21}$$

we notice that for all positive x values, the radiation force is also positive. Hence, the particles are repelled by the oscillating wall.

7.2 Analytic Example 2: Wave resonance, 1D

The second example concerns a liquid under influence of a cavity wave. The wave is created by two oscillating walls at $x = -L$ and $x = L$. The walls are set to oscillate asymmetrically at a resonance frequency.

7.2.1 First order pressure, p_1, and velocity u_1

Since, this system is identical to that in Section 4.4.2 we immediately see from Eq. (4.40) that

$$\widehat{u}_1 = \frac{(-1)^n \epsilon c_0}{2n\pi\gamma}, \qquad \text{where } \epsilon = \frac{\omega \ell}{c_0}, \tag{7.22}$$

fulfills the boundary conditions. To find p_1 we make the following guess

$$p_1(x,t) = -\frac{\widehat{p}_1}{\widehat{u}_1 k_0 (i-\gamma)} \partial_x u_1 = \widehat{p}_1 \Big(e^{-k_0(i-\gamma)x} + e^{k_0(i-\gamma)x} \Big) e^{-i\omega t}, \tag{7.23}$$

so that

$$\partial_x p_1(x,t) = -k_0(i-\gamma)\frac{\widehat{p}_1}{\widehat{u}_1} u_1, \tag{7.24}$$

and inserts this into the one dimensional edition of Eq. (3.47)

$$\partial_x^2 u_1 = -i\frac{\omega\rho_0}{\eta} u_1 + \Big[1 - i\frac{\omega\beta\eta}{\rho_0 c_0^2}\Big]\frac{1}{\eta}\partial_x p_1. \tag{7.25}$$

We find that

$$\widehat{p}_1 = -\rho_0 c_0 \Big[1 + i\gamma\Big]\widehat{u}_1. \tag{7.26}$$

So to summarize the first order terms we got

$$\begin{aligned} u_1(x,t) =& \frac{(-1)^n \epsilon c_0}{2n\pi\gamma}\Big(e^{-k_0(i-\gamma)x} - e^{k_0(i-\gamma)x}\Big) e^{-i\omega t} \\ \approx& \frac{(-1)^n \epsilon c_0}{n\pi}\Big(k_0 x \cos(k_0 x) - \frac{i}{\gamma}\sin(k_0 x)\Big) e^{-i\omega t}, \end{aligned} \tag{7.27}$$

$$\begin{aligned} p_1(x,t) =& -\frac{(-1)^n \epsilon[1+i\gamma]}{2n\pi\gamma}\rho_0 c_0^2 \Big(e^{-k_0(i-\gamma)x} + e^{k_0(i-\gamma)x}\Big) e^{-i\omega t}, \\ \approx& \frac{(-1)^n \epsilon}{n\pi}\rho_0 c_0^2 \Big(\frac{1}{\gamma}\cos(k_0 x) + i\Big[\cos(k_0 x) - k_0 x \sin(k_0 x)\Big]\Big) e^{-i\omega t}, \end{aligned} \tag{7.28}$$

We notice the maximum value of u_1 becomes $\frac{\epsilon c_0}{n\pi\gamma} \approx 0.35 c_0$ for $n = 1$. Hence, the validity of the perturbation method becomes questionable, since $0.35 \approx 1$. We shall however proceed anyway.

7.2.2 Second order pressure, p_2'', and velocity u_2''

We can now begin to solve the one dimensional editions of Eq. (3.61) and Eq. (3.62)

$$\partial_x u_2'' = -\frac{1}{2c_0^2\rho_0}\partial_x \mathrm{Re}\left[\tilde{p}_1\tilde{u}_1^*\right], \tag{7.29}$$

$$\begin{aligned}\eta\partial_x^2 u_2'' + \beta\eta\partial_x(\partial_x u_2'') =& \partial_x p_2'' + F''\\ (\beta+1)\eta\partial_x^2 u_2'' =& \partial_x p_2'' + F''\end{aligned} \tag{7.30}$$

We insert the known first order terms into Eq. (7.29) and integrate to find u_2''

$$\begin{aligned}u_2'' =& -\frac{1}{2c_0^2\rho_0}\int\Big(\partial_x \mathrm{Re}\left[\tilde{p}_1\tilde{u}_1^*\right]\Big)\,\mathrm{d}x = -\frac{1}{2c_0^2\rho_0}\mathrm{Re}\left[\tilde{p}_1\tilde{u}_1^*\right] + C_u\\ =& -\frac{1}{2c_0^2\rho_0}\frac{c_0^3\epsilon^2\rho_0}{4(n\pi\gamma)^2}\Big(e^{-2k_0\gamma x} - e^{2k_0\gamma x} + 2\gamma\sin(2k_0x)\Big) + C_u\\ =& -\frac{\epsilon^2}{8(n\pi\gamma)^2}c_0\Big(e^{-2k_0\gamma x} - e^{2k_0\gamma x} + 2\gamma\sin(2k_0x)\Big) + C_u.\end{aligned} \tag{7.31}$$

Next we calculate F'' according to Eq. (3.38) in one dimension

$$\begin{aligned}F'' =& \frac{1}{2}\rho_0\mathrm{Re}\big[\tilde{u}_1\partial_x\tilde{u}_1^*\big] + \frac{1}{2}\rho_0\mathrm{Re}\big[\tilde{u}_1\partial_x\tilde{u}_1^*\big] = \rho_0\mathrm{Re}\big[\tilde{u}_1\partial_x\tilde{u}_1^*\big]\\ =& \frac{\epsilon^2}{4(n\pi\gamma)^2}c_0\omega\rho_0\Big(-\gamma e^{-2k_0\gamma x} + \gamma e^{2k_0\gamma x} + 2\sin(2k_0x)\Big)\end{aligned} \tag{7.32}$$

We can now find p_2'' by inserting Eq. (7.14) and Eq. (7.15) into Eq. (7.13), integrate and expand in γ

$$\begin{aligned}p_2'' =& \frac{\epsilon^2(4\gamma^2-1)}{4(n\pi\gamma)^2}c_0\omega\rho_0\int\Big(-\gamma e^{-2k_0\gamma x} + \gamma e^{2k_0\gamma x} + 2\sin(2k_0x)\Big)\,\mathrm{d}x\\ =& \frac{\epsilon^2(4\gamma^2-1)}{8(n\pi\gamma)^2}c_0^2\rho_0\Big(e^{-2k_0\gamma x} + e^{2k_0\gamma x} - 2\cos(2k_0x)\Big) + C_p\\ \approx& -\frac{1}{2}\left(\frac{c_0\epsilon}{n\pi\gamma}\right)^2\rho_0\sin^2(k_0x) + C_p.\end{aligned} \tag{7.33}$$

In order for us to use p_2'' in the calculation of the acoustic radiation force, C_p must be defined such that $p_2''(\mathbf{r}) > 0$. Hence,

$$C_p = \frac{1}{2}\left(\frac{c_0\epsilon}{n\pi\gamma}\right)^2\rho_0. \tag{7.34}$$

We now calculate the time-averaged flux J_2''. As in Section 7.1 we must require that the flux in steady state is zero.

$$J_2'' = \langle\rho_1 u_1\rangle_t + \rho_0 u_2'' = 0. \tag{7.35}$$

We can quickly see that

$$\rho_0 u_2'' = -\frac{1}{8}\left(\frac{\epsilon}{n\pi\gamma}\right)^2 c_0\rho_0\Big(e^{-2k_0\gamma x} - e^{2k_0\gamma x} + 2\gamma\sin(2k_0 x)\Big) + \rho_0 C_u, \tag{7.36}$$

and that

$$\langle\rho_1 u_1\rangle_t = \frac{1}{2}\mathrm{Re}\left[\frac{\tilde{p}_1}{c_0^2}\tilde{u}_1^*\right] = \frac{\epsilon^2}{8(n\pi\gamma)^2}c_0\rho_0\Big(e^{-2k_0\gamma x} - e^{2k_0\gamma x} + 2\gamma\sin(2k_0 x)\Big). \tag{7.37}$$

Hence, we find

$$J_2'' = \frac{\epsilon^2(1-1)}{8(n\pi\gamma)^2}c_0\rho_0\Big(e^{-2k_0\gamma x} - e^{2k_0\gamma x} + 2\gamma\sin(2k_0 x)\Big) + \rho_0 C_u = 0. \tag{7.38}$$

if $C_u = 0$. Finally we calculate the shape of the acoustic radiation force from Eq. (6.4)

$$\begin{aligned} F_{ar} &= -\tau p_2''\partial_x p_2'' \\ &\approx -\frac{1}{2}\left(\frac{c_0\epsilon}{n\pi\gamma}\right)^4 \tau k_0\rho_0^2\cos(k_0 x)\sin^3(k_0 x) \end{aligned} \tag{7.39}$$

we notice that particles with $\tau > 0$ accumulate at p_1-nodes.

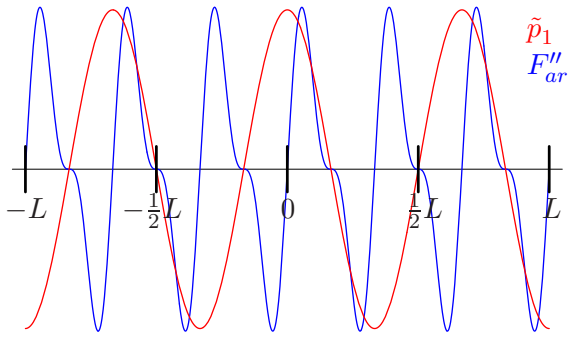

Figure 7.1: The red line shows the amplitude of the first order pressure, $\tilde{p}_1$. The blue line shows the acoustic radiation force affecting blood cell like particles. Both for $n = 3$. We notice that the force makes the particles accumulate at the $\tilde{p}_1$ nodes. Both amplitudes are shown normalized.

7.3 Numeric Example 3: Wave resonance, 2D

In this example we consider a two dimensional system with walls at $x = \pm L$ and $y = \pm L$. we assume that parallel walls oscillate antisymmetric.

7.3.1 First order pressure, p_1, and velocity u_1

To model the oscillating walls we state

$$\mathbf{J}_1 = \begin{pmatrix} J_{x,1}(\pm L, t) \\ J_{y,1}(\pm L, t) \end{pmatrix} = \begin{pmatrix} \pm\epsilon\rho_0 c_0 e^{-i\omega t} \\ \pm r e^{i\theta}\epsilon\rho_0 c_0 e^{-i\omega t} \end{pmatrix}, \tag{7.40}$$

where θ describes the phase shift and r the amplitude ratio. The first order velocity field, $\mathbf{u}_1$ must then be defined as a linear combination of two opposite traveling waves in both the $x-$ and $y-$direction

$$\mathbf{u}_1(x,y,t) = \begin{pmatrix} \tilde{u}_1(x)\, e^{-i\omega t} \\ \tilde{v}_1(y)\, e^{-i\omega t} \end{pmatrix}, \qquad \begin{pmatrix} \tilde{u}_1(x) = \widehat{u}_1\big(e^{-k_0(i-\gamma)x} - e^{k_0(i-\gamma)x}\big) \\ \tilde{v}_1(y) = \widehat{v}_1\big(e^{-k_0(i-\gamma)y} - e^{k_0(i-\gamma)y}\big) \end{pmatrix} \tag{7.41}$$

From the antisymmetry we have the boundary conditions

$$\begin{array}{ccc} \tilde{u}_1(-L) = -\omega\ell & \tilde{u}_1(0) = 0 & \tilde{u}_1(L) = \omega\ell \\ \tilde{v}_1(-L) = -re^{i\theta}\omega\ell & \tilde{v}_1(0) = 0 & \tilde{v}_1(L) = re^{i\theta}\omega\ell. \end{array} \tag{7.42}$$

We find from Section 4.4.2 that

$$\widehat{u}_1 = \frac{(-1)^n \epsilon c_0}{2n\pi\gamma}, \tag{7.43}$$

and using the same approach that

$$\widehat{v}_1 = re^{i\theta}\frac{(-1)^n \epsilon c_0}{2n\pi\gamma}, \tag{7.44}$$

which fulfills the boundary conditions. To find p_1 we make the following guess

$$\begin{aligned} p_1(x,y,t) &= -\frac{\widehat{p}_{x,1}}{\widehat{u}_1 k_0(i-\gamma)}\partial_x u_1 - \frac{\widehat{p}_{y,1}}{\widehat{v}_1 k_0(i-\gamma)}\partial_y v_1 \\ &= \left[\widehat{p}_{x,1}\Big(e^{-k_0(i-\gamma)x} + e^{k_0(i-\gamma)x}\Big) + \widehat{p}_{y,1}\Big(e^{-k_0(i-\gamma)y} + e^{k_0(i-\gamma)y}\Big)\right] e^{-i\omega t}, \end{aligned} \tag{7.45}$$

so that

$$\partial_x p_1 = -k_0(i-\gamma)\frac{\widehat{p}_{x,1}}{\widehat{u}_1}u_1 \tag{7.46}$$

$$\partial_y p_1 = -k_0(i-\gamma)\frac{\widehat{p}_{y,1}}{\widehat{v}_1}v_1 \tag{7.47}$$

this guess fulfills the Helmholtz equation Eq. (3.51). We find $\widehat{p}_1$ by inserting Eq. (7.45) into Eq. (3.47)

$$\nabla^2\mathbf{u}_1 = -i\frac{\omega\rho_0}{\eta}\mathbf{u}_1 + \Big[1 - i\frac{\omega\beta\eta}{\rho_0 c_0^2}\Big]\frac{1}{\eta}\boldsymbol{\nabla}p_1. \tag{7.48}$$

Hence, we get

$$\widehat{p}_{x,1} = -\rho_0 c_0 \Big[1 + i\gamma\Big]\widehat{u}_1. \tag{7.49}$$

$$\widehat{p}_{y,1} = -\rho_0 c_0 \Big[1 + i\gamma\Big]\widehat{v}_1. \tag{7.50}$$

To summarize the first order terms we got

$$\mathbf{u}_1(x,y,t) = \frac{(-1)^n \epsilon c_0}{2n\pi\gamma} \begin{pmatrix} e^{-k_0(i-\gamma)x} - e^{k_0(i-\gamma)x} \\ re^{i\theta}e^{-k_0(i-\gamma)y} - re^{i\theta}e^{k_0(i-\gamma)y} \end{pmatrix} e^{-i\omega t}, \tag{7.51}$$

$$p_1(x,y,t) = -\Big[1+i\gamma\Big]\frac{(-1)^n\epsilon}{2n\pi\gamma}\Big(e^{-k_0(i-\gamma)x}+e^{k_0(i-\gamma)x}+re^{i\theta}e^{-k_0(i-\gamma)y}+re^{i\theta}e^{k_0(i-\gamma)y}\Big)\rho_0 c_0^2 e^{-i\omega t}, \tag{7.52}$$

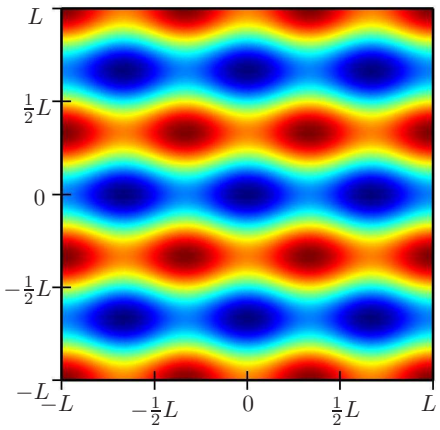

Figure 7.2: This is scalar 2D-plot, red colors mean high values, while blue colors are low. The plot shows the form of the first order pressure amplitude, $\tilde{p}_1$, at a $k_0 = \frac{3\pi}{L}$-resonance. The horizontal walls oscillate three times stronger than the verticals, $r = 3,\ \theta = 0$. Data range $\pm 10^9$ Pa.

By carefully selecting the right parameters, we have obtained a first order pressure field, which is similar to that of Fig. 6.7 panel 4b. We notice the maximum value of 10^9 Pa is far to extreme to give any physical meaning. The amplitude reaches such heights because we have chosen a resonance frequency. A real system would shatter if a pressure of 10^4 atm were induced. Hence, it becomes apparent that the derivation of $\widehat{u}_1$ in Section 4.4.2 is flawed. Somehow, the amplitude of $\mathbf{u}_1$ must be much smaller. So even though these high amplitudes ruins the perturbation method, we continue anyway as all terms in the end will depend on $\widehat{u}_1$. So, if future work can prove that $\widehat{u}_1$ is in fact much smaller, this theory will be valid. The parameters used for Fig. 7.2 will also be used in the following figures.

7.3.2 Second order pressure, p_2'', and velocity $\mathbf{u}_2''$

To find the second order terms we must solve the two second order equations Eq. (3.61) and Eq. (3.62)

$$\boldsymbol{\nabla}\cdot\mathbf{u}_2'' = -\frac{1}{2c_0^2\rho_0}\boldsymbol{\nabla}\cdot\mathrm{Re}\left[\tilde{p}_1\tilde{\mathbf{u}}_1^*\right] = S \tag{7.53}$$

$$\eta\nabla^2\mathbf{u}_2'' = \boldsymbol{\nabla}p_2'' + \mathbf{F}'' - \beta\eta\boldsymbol{\nabla}(\boldsymbol{\nabla}\cdot\mathbf{u}_2''). \tag{7.54}$$

To solve these equations, we will first have to calculate S and $\mathbf{F}$. We start by finding the two components of $\langle p_1\mathbf{u}_1\rangle_t = \frac{1}{2}\mathrm{Re}\left[\tilde{p}_1\tilde{\mathbf{u}}_1^*\right]$. We expand to the second leading order of γ and assume $\theta = 0$, as in Fig. 7.2

$$\begin{aligned}\frac{1}{2}\mathrm{Re}\left[\tilde{p}_1\tilde{u}_1^*\right] \approx \gamma\widehat{u}_1^2\rho_0 c_0\Big[&-2k_0x + \sin(2k_0x) - 2rk_0x\cos(k_0x)\cos(k_0y)\\ &- 2rk_0y\sin(k_0x)\sin(k_0y) + 2r\cos(k_0y)\sin(k_0x)\Big]\end{aligned} \tag{7.55}$$

$$\begin{aligned}\frac{1}{2}\mathrm{Re}\left[\tilde{p}_1\tilde{v}_1^*\right] \approx \gamma\widehat{u}_1^2\rho_0 c_0\Big[&-2r^2k_0y + r^2\sin(2k_0y) - 2rk_0y\cos(k_0x)\cos(k_0y)\\ &- 2rk_0x\sin(k_0x)\sin(k_0y) + 2r\cos(k_0x)\sin(k_0y)\Big]\end{aligned} \tag{7.56}$$

Eq. (7.55) and Eq. (7.56) are plotted in Fig. 7.3 panel (a) and (b), respectively.

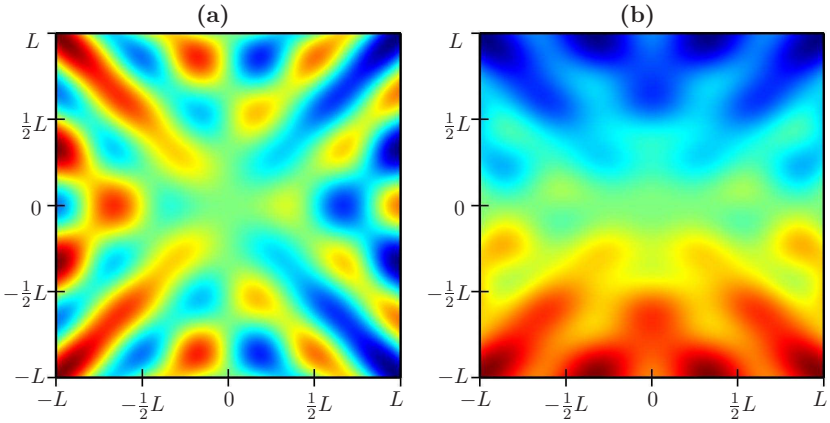

Figure 7.3: Panel (a) shows $\langle p_1u_1\rangle_t$ and panel (b) shows $\langle p_1v_1\rangle_t$, both at $k_0 = \frac{3\pi}{L}$, $r = 3$, $\theta = 0$. The data range for panel (a) is $\pm 7\times10^6$ Pa m s^{-1}, while r times larger for panel (b).

Then we can find S

$$\begin{aligned}S = \boldsymbol{\nabla}\cdot\mathbf{u}_2'' &= -\frac{1}{2c_0^2\rho_0}\boldsymbol{\nabla}\cdot\mathrm{Re}\left[\tilde{p}_1\tilde{\mathbf{u}}_1^*\right] = -\frac{1}{c_0^2\rho_0}\Big(\partial_x\frac{1}{2}\mathrm{Re}\left[\tilde{p}_1\tilde{u}_1^*\right] + \partial_y\frac{1}{2}\mathrm{Re}\left[\tilde{p}_1\tilde{v}_1^*\right]\Big)\\ &\approx \frac{2\gamma\omega\widehat{u}_1^2}{c_0^2}\Big(1 + r^2 - \cos(2k_0x) - r^2\cos(2k_0y)\Big).\end{aligned} \tag{7.57}$$

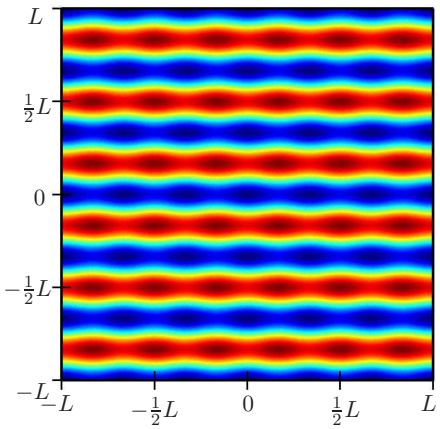

Figure 7.4: S at $k_0 = \frac{3\pi}{L},\ r = 3,\ \theta = 0$. Data range is $0 - 16\ \mathrm{s}^{-1}$

We notice that S depends on $\widehat{u}_1^2$. Hence, if $\widehat{u}_1$ is greatly reduced, we see that $S \approx 0$ for a water-like liquid. This corresponds very well to the incompressible($\boldsymbol{\nabla}\cdot\mathbf{u} = 0$) liquid normally use for microfluidic calculations.

Next we find $\mathbf{F}''$ from equation Eq. (3.38)

$$\mathbf{F}'' = \frac{1}{2}\rho_0 \mathrm{Re}\left[(\tilde{\mathbf{u}}_1\cdot\boldsymbol{\nabla})\tilde{\mathbf{u}}_1^*\right] + \frac{1}{2}\rho_0 \mathrm{Re}\left[\tilde{\mathbf{u}}_1(\boldsymbol{\nabla}\cdot\tilde{\mathbf{u}}_1^*).\right] \tag{7.58}$$

We split it into the $x-$ and $y-$component

$$\begin{aligned} F_x'' &= \frac{1}{2}\rho_0 \mathrm{Re}\left[(\tilde{u}_1\partial_x + \tilde{v}_1\partial_y)\tilde{u}_1^*\right] + \frac{1}{2}\rho_0 \mathrm{Re}\left[\tilde{u}_1(\partial_x\tilde{u}_1^* + \partial_y\tilde{v}_1^*)\right] \\ &\approx 2\widehat{u}_1^2 k_0\rho_0\Big(\sin(2k_0x) + r\cos(k_0y)\sin(k_0x)\Big), \end{aligned} \tag{7.59}$$

and

$$\begin{aligned} F_y'' &= \frac{1}{2}\rho_0 \mathrm{Re}\left[(\tilde{u}_1\partial_x + \tilde{v}_1\partial_y)\tilde{v}_1^*\right] + \frac{1}{2}\rho_0 \mathrm{Re}\left[\tilde{v}_1(\partial_x\tilde{u}_1^* + \partial_y\tilde{v}_1^*)\right] \\ &\approx 2\widehat{u}_1^2 k_0\rho_0\Big(r^2\sin(2k_0y) + r\cos(k_0x)\sin(k_0y)\Big). \end{aligned} \tag{7.60}$$

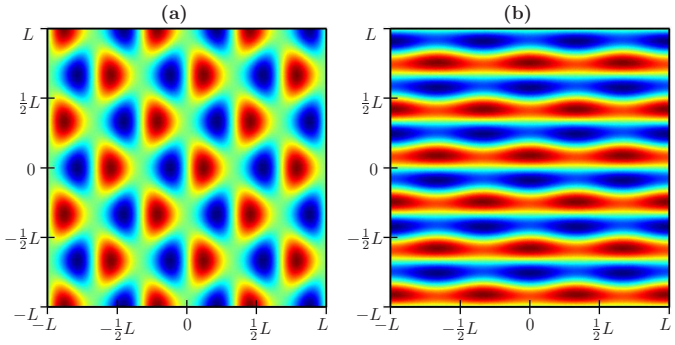

Figure 7.5: Panel (a) shows F_x'' and panel (b) shows F_y'', both at $k_0 = \frac{3\pi}{L},\ r = 3,\ \theta = 0$. The data range in panel (a) is $\pm 5 \times 10^{11}$ N m^{-3}, while 9 (r^2) times larger in panel (b)

Now that S and $\mathbf{F}''$ have been calculated, we can use COMSOL to solve the three coupled partial differential equations numerically(see Appendix D). In this model we can safely state that the flux normal to any boundary must be zero, as we have non-porous walls. On the other hand, it is not obvious what conditions we can assume parallel to the walls, as these are oscillating. But if we have a water-like liquid, we see that the characteristic length scale of momentum diffusion is $L_D = \sqrt{\frac{\eta}{\rho_0 \omega}} = 1\ \mu$m, which is much smaller than the element size, used in the numerical calculations. This means that the model should not be sensitive to small changes in the boundary conditions. Hence, we choose a neutral boundary condition; we assume the viscous stress is zero. These conditions are implemented using the method from Section 5.2 by setting

$$\begin{aligned} R =& \{R_{p_2''}, R_{u_2''}, R_{v_2''}\} = \{0,\ J_{2,x}'',\ 0\} \\ G =& \{G_{p_2''}, G_{u_2''}, G_{v_2''}\} = \{0,\ 0,\ 0\} \end{aligned} \tag{7.61}$$

for the vertical walls and

$$\begin{aligned} R =& \{R_{p_2''}, R_{u_2''}, R_{v_2''}\} = \{0,\ 0,\ J_{2,y}''\} \\ G =& \{G_{p_2''}, G_{u_2''}, G_{v_2''}\} = \{0,\ 0,\ 0\} \end{aligned} \tag{7.62}$$

for the horizontal walls.

The numerical results for u_2'', v_2'' and p_2'' are shown below.

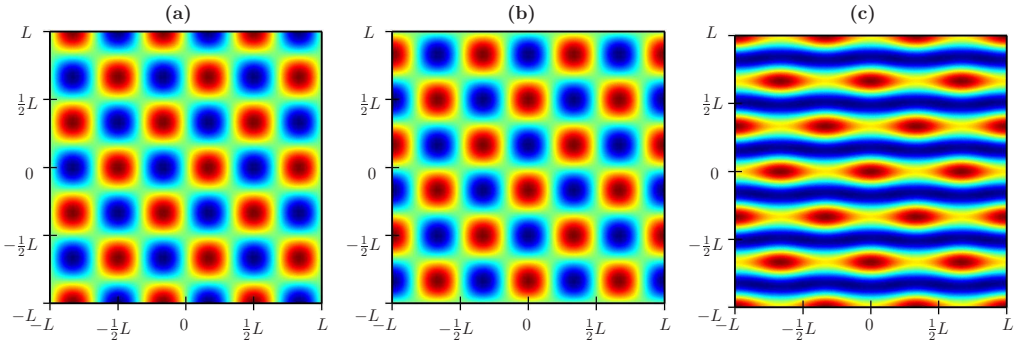

Figure 7.6: Numeric results from COMSOL for $k_0 = \frac{3\pi}{L}$, $r = 3$, $\theta = 0$. Panel (a) and (b) shows u_2'' and v_2'', respectively. Panel (c) shows p_2''. The data range in both panel (a) and (b) is $\pm 2.5 \times 10^6$ m s^{-1}. The data range for panel (c) is $0 - 5 \times 10^8$ Pa.

Again, we notice that the amplitude of several million meters per second is far to high. In Chapter 8 we shall non the less try to compare these results with those experimentally obtained.

Chapter 8

Comparing theory and experiments

As mentioned earlier, we have a huge problem regarding the amplitudes of all the fields involved in this calculation. But by normalizing the numeric results, their relative values can still be compared to those from the experiments.

8.1 Simulated streaming patterns

By plotting the numeric results for u_2'' and v_2'' in a vector plot we can still compare the resulting flow-pattern. In Fig. 8.1 panel (a) we see that a pattern of 6×6 vortices has appeared. We notice that this pattern is very similar to that obtained during the experiments, Panel (b). The frequency corresponding to the $k_0 = \frac{n\pi}{L} = \frac{3\pi}{0.001}\mathrm{m}^{-1}$ resonance is 2.2245 MHz. For the corresponding experiment (Fig. 8.1 panel (b)) the frequency was approximately 2.17 MHz. Panel (c) shows the result of a calculation performed at the $k_0 = \frac{n\pi}{L} = \frac{\pi}{0.001}\mathrm{m}^{-1}$ resonance with a frequency at 0.74 MHz. This 2×2 vortex pattern was also observed experimentally, at 0.76 MHz. Even though the experimental data shown in panel (d) does not show four complete vortices, it is so close that we assume the correct state has been found. The lack of uniformity in the experimental data, might by caused by asymmetries in the chip itself or in the entire experimental setup.

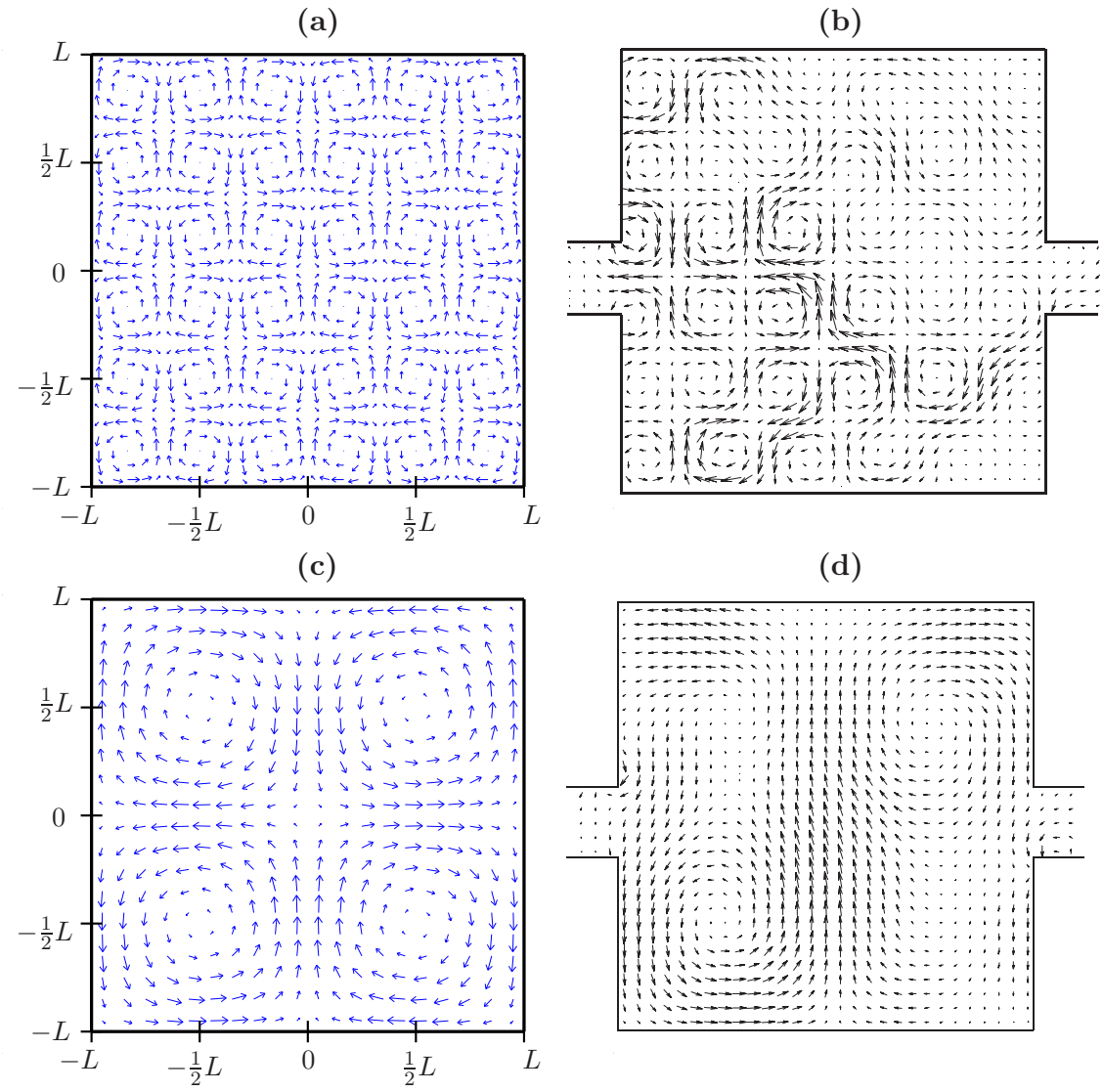

Figure 8.1: Comparison of vector-plots of the calculated velocities to the PIV-pictures of the experimental velocities of the small particles. Panel(a) shows a pattern of 6×6 vortices found at the $k_0 = 3\pi/L$ resonance(2.2 MHz). Panel (b) shows the flow-pattern found at 2.17 MHz. We notice that the predicted 6x6-vortices were indeed observed, and since the experiment were made with small particles they are not noticeably affected by the radiation force. Panel(c) shows a pattern of 2×2 vortices found at the $k_0 = \pi/L$ resonance(0.74 MHz). Panel (b) shows the flow-pattern found at 0.76 MHz for small particles. We notice that the predicted 2×2-vortices also were observed. PIV-pictures(panel (b) and (d)) courtesy Melker Sundin.

The velocity observed in the experiments corresponds to $\widehat{u}_1 \approx \omega\ell \approx 0.001$ m/s were the calculations were performed with $\widehat{u}_1 \approx 87$ m/s as predicted in Section 4.4.2.

8.2 Simulated radiation force

If we turn to look at the acoustic radiation force acting on a particle, we find the expression from Eq. (6.4)

$$\mathbf{F}''_{ar} = -\tau p''_2 \boldsymbol{\nabla} p''_2 \tag{8.1}$$

By plotting the normalized acoustic radiation force we can see that the corresponding bead pattern corresponds very well to the experimental bead pattern.

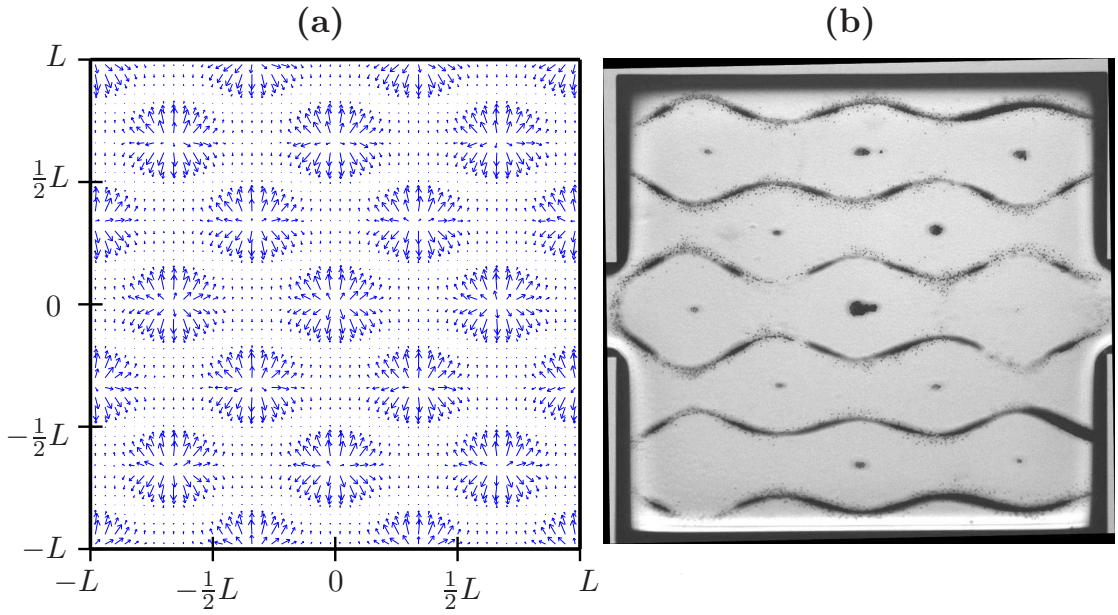

Figure 8.2: We see that the larger particles were observed to accumulate where the theory predicts.

By assuming the particle motion can be described by a quasi-stationary steady state flow, we can express the particle velocity as proportional to the acoustic radiation force. Hence, if both are normalized they become identical. Fig. 8.3 shows the experimentally measured bead velocity in the y-direction for $x = \pm L/3$. Due to symmetry the y-component of the theoretically radiation force is the same for $x = \pm L/3$. Hence, only one line represents $F_{ar,y}$

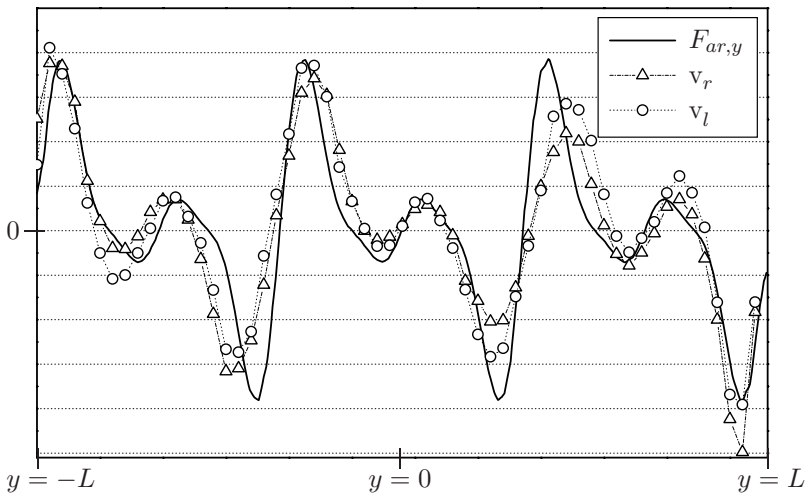

Figure 8.3: Vertical cross-sectional plots of the experimental velocity in the y-direction for $x = -L/3$ (v_l) left and $1x = L/3$ (v_r) right of the center of the chamber. $F_{ar,y}$ is the calculated force in y-direction. By assuming a quasi-stationary steady state motion of the particles, we can directly compare force to velocity. Velocity data courtesy Melker Sundin.

Taking the relatively coarse derivation of $\mathbf{F}_{ar}$ (Section 6.2) into account, the shape of the calculated acoustic radiation force is very similar to the experimental data.

Chapter 9

Conclusion

In Chapter 2 it has been shown that the assumption of oscillating walls surrounding an incompressible liquids, is not sufficient to explain how relatively strong flow patterns can exist far from the boundary. However, by comparing analytical solutions to numerical solution, we have confirmed that the perturbation method is an acceptable approach for this kind of system.

The realization that the no-slip condition actually applies to the flux and not only to the velocity of a compressible liquid, must be emphasized, as the lack of this (in the hindsight) obvious statement caused some huge problems in the early development of this work.

In Chapter 6 it is shown that the nodal-lines in solutions to a eigen-frequency analysis of the pressure-based Helmholtz equation, provide a very accurate hint to were suspended beads will eventually accumulate. If the location of the nodal-lines is combined with the gradient of the corresponding first-order pressure field, one can estimate the relative strength of acoustic radiation force. It is also shown that as long as the acoustic wavelengths are more than twice the length of a dimension, the dimension can be omitted from the eigen-frequency analysis and the result will still be reasonably accurate.

From the comparisons in Chapter 8 it can be seen that the expression derived in Section 6.2 for the acoustic radiation force is very useful. The expression can not only account for where the particles will accumulate, but it also tells where they will collect fastest, and finally it gives a reasonable argument to why small particles seems unaffected($\mathbf{F}_{ar} \propto r^4$).

However, from the apparently un-physically high amplitudes calculated, we are lead to the conclusion that the derivation of the resonance amplitudes in Section 4.4.2 is flawed. One can argue if it is the oscillation amplitude of walls that has been estimated to be too high(1 nm) or if the damping in the system is artificially low. Perhaps it is necessary to include a loss because of heating.

In Chapter 8 it can be seen the equations developed in Chapter 3 are able to explain the experimentally observed flow patterns, though again the amplitudes were far to high.

Hence, it can be concluded that the main contributions to the acoustic radiation force and to acoustic streaming have been understood, with the exception of the amplitudes at resonance-frequencies.

Chapter 10

Outlook

To improve the work presented in this thesis, it is obvious that the theory for the attenuated resonating waves most be remodeled. To validate the results in this thesis, it must be explained why the particle velocity amplitude is much lower than assumed. To support any new theory it would be a huge advantage to perform experimental measurements of some of the properties ($\mathbf{u}_1$, p_1, p_2'' etc.) on carefully designed symmetric chips. This would ease the process when comparing simulations and experiments.

Another interesting aspect to investigate, would be whether the approach used for finding flow-patterns in the square chamber, can directly be used for the round chamber.

It would also be interesting to derive the acoustic radiation force in greater detail, and hopefully find an expression for the absolute force and not only the relative.

To calculate the the flow-patterns for any given geometry and resonance frequency, it might be necessary to develop a method to extract the first order terms from the eigen-frequency analysis. By doing so it would not be necessary to guess the strength and phase-shift for each oscillating wall.

Finally the consequences of assuming that all the materials used are isotropic, when we know the that the speed of sound in silicon is highly lattice dependant, should be investigated.

Appendix A

COMSOL-script; Periodic motion in incompressible liquids

This appendix contains the COMSOL-script use to obtain the numerical solution in Section 2.4. The script is compiled for COMSOL ver. 3.2

COMSOL

```
% Cleaning up
clc;close all;clear;flclear fem

% Definig the Constants
PE = 1e-9;          % Piezo Expansion, 1nm
Pd =  2*pi*1e-6;     % Piezo distance,
qq =2*pi/Pd;        % wavenumber
ee = 1;             % Becomes Pe
w = 2*pi*1e6*ee;    % Angular frequency
frek = w/(2*pi);    % Frequency
vv0 = frek*PE;      % Slip velocity
Tp = 1/frek;        % time of one period
n = 15;             % number of cycles, endtime = n*Tp
Ntrans = 10;        % number of cycles to be discarded (transient)
nt = 100;           % number of timesteps per cycle
int =Tp/nt;         % time interval
smesh = Pd/25;      % mesh size

% Introducing the Constants to COMSOL
fem.const = {'bl',Pd,'q',qq,'eta','1e-3','rho','1e3','f',frek,'v0',vv0, ...
  'w',w,'epss','rho*w/(eta*q^2)','Re','rho*v0/(q*eta)'};

% Creating geometry
g1=square2('bl','base','corner','pos',{'0','0'},'rot','0','const',fem.const);
s.objs={g1};
s.name={'SQ1'};
s.tags={'g1'};
fem.draw=struct('s',s);
fem.geom=geomcsg(fem);

% Initialize mesh
fem.mesh=meshinit(fem,'hgrad',1.025,'hmaxedg',[2,smesh]);

% Application mode 1
```

```
clear appl
appl.mode.class = 'FlNavierStokes';
appl.gporder = {4,2};
appl.cporder = {2,1};
appl.assignsuffix = '_ns';
clear pnt
pnt.pnton = {0,1};
pnt.ind = [1,2,1,1];
appl.pnt = pnt;
clear bnd
bnd.u0 = {0,'v0*cos(q*x)*sin(w*t)',0};
bnd.type = {'noslip','uv','neutral'};
bnd.ind = [3,2,1,3];
appl.bnd = bnd;
clear equ
equ.init = {{0;0;0}};
equ.rho = 'rho';
equ.eta = 'eta';
equ.cporder = {{1;1;2}};
equ.gporder = {{1;1;2}};
equ.ind = [1];
appl.equ = equ;
fem.appl{1} = appl;
fem.border = 1;
fem.units = 'SI';

% Coupling variable elements
clear elemcpl
% Extrusion coupling variables
clear elem
elem.elem = 'elcplextr';
elem.g = {'1'};
src = cell(1,1);
clear bnd
bnd.expr = {{{},'u'},{{},'v'},{{},'p'}};
bnd.map = {'0','0','0'};
bnd.ind = {{'1','2','3'},{'4'}};
src{1} = {{},bnd,{}};
elem.src = src;
geomdim = cell(1,1);
clear bnd
bnd.map = {{{},'1'},{{},'1'},{{},'1'}};
bnd.ind = {{'2','3','4'},{'1'}};
geomdim{1} = {{},bnd,{}};
elem.geomdim = geomdim;
elem.var = {'pconstr1','pconstr2','pconstr3'};
map = cell(1,1);
clear submap
submap.type = 'linear';
submap.sg = '1';
submap.sv = {'1','2'};
submap.dg = '1';
submap.dv = {'3','4'};
%submap.dv = {'9','10'};
```

```
map{1} = submap;
elem.map = map;
elemcpl{1} = elem;
% Point constraint variables (used for periodic conditions)
clear elem
elem.elem = 'elpconstr';
elem.g = {'1'};
clear bnd
bnd.constr = {{'pconstr1-(u)','pconstr2-(v)','pconstr3-(p)'}};
bnd.cpoints = {{'2','2','1'}};
bnd.ind = {{'1'}};
elem.geomdim = {{{},bnd,{}}};
elemcpl{2} = elem;
fem.elemcpl = elemcpl;

% Solve problem
fem=multiphysics(fem);
fem.xmesh=meshextend(fem);
fem.sol=femtime(fem, ...
                'solcomp',{'u','p','v'}, ...
                'outcomp',{'u','p','v'}, ...
                'tlist',[0:int:n*Tp], ...       %Give output at these time-steps
                'atol',{'1e-10'}, ...
                'rtol',0.001, ...
                'estrat',1, ...
                'tout','tlist');

% Save parameter in fem structure
fem.tgj.n = n;
fem.tgj.Ntrans = Ntrans;
fem.tgj.nt = nt;
fem.tgj.v0 = vv0;
fem.tgj.int = int;
fem.tgj.smesh = smesh;
fem.tgj.epss=postint(fem,'epss', 'dl',[3],'edim',0);
fem.tgj.Re=postint(fem,'Re','dl',[3], 'edim',0);

% Calculating the time-averaged solution
femsolu=fem.sol.u;
SIZEU=size(femsolu);
r = SIZEU(1);
s = SIZEU(2);
U = zeros(r,1);
k =fem.tgj.Ntrans*fem.tgj.nt;
for i = k:s % Sum up solutions, without transint
    U = U + femsolu(:,i);
end
U = U./(s-k);
fem.tgj.avgU = U;

% Find Absolute Average Velocity
U = fem.tgj.avgU;
int = postint(fem,'(U_ns^2)^0.5','U',U,'dl',[1]); %use U as input (not fem)
fem.tgj.INT_ER = int/(Pd*Pd)
```

```
143
144 % Investigate the transient
145 figure
146 SIZEU = size(fem.sol.u);
147 r = SIZEU(1);
148 s = SIZEU(2);
149
150 field = 2251;
151 p = round(fem.tgj.nt);
152 for i=1:s
153    i/s
154    u(i)=postint(fem,'u','dl',[3],'solnum',i,'edim',0);
155    t(i) = fem.sol.tlist(i);
156 end
157
158 t0 = 2; % Two random timesteps
159 t1 = 8;
160 plot(t(t1:p:end),u(t1:p:end),'r-'),hold on
161 plot(t(t1:p:end),u(t1:p:end),'ro'),hold on
162 plot(t(t0:p:end),u(t0:p:end),'ro'),hold on
163 plot(t(t0:p:end),u(t0:p:end),'r-'),hold on
164
165 bc = -sin(fem.tgj.n*2*pi*(fem.sol.tlist)./fem.sol.tlist(end)')/1e6;
166
167 plot(t,bc,'k:'),hold on
168 plot(t,u,'b-'),hold on
169 plot(t,u,'bx')
170
171 % Plot Averaged solution
172 figure
173 %fem.xmesh=meshextend(fem);
174
175 postplot(fem,'tridata',{'u','cont','internal'}, ...
176          'trimap','jet(1024)', ...
177          'U',fem.tgj.avgU,...
178          'arrowdata',{'u','v'}, ...
179          'arrowxspacing',30, ...
180          'arrowyspacing',30, ...
181          'arrowtype','arrow', ...
182          'arrowstyle','proportional', ...
183          'arrowcolor',[1.0,0.0,0.0], ...
184          'solnum',1, ...
185          'title',['Time-averaged velocity - first ', num2str(10),' periods discarded'], ...
186          'refine',3);
```

COMSOL

Appendix B

COMSOL-script; Wave propagation through interfaces

This appendix contains the COMSOL-script use to obtain the numerical solution in Section 4.3. The script is compiled for COMSOL ver. 3.2

COMSOL

```
% Cleaning up
clear,flgc,clc,flclear fem

% Constants
fem.const = {'f','5.6887e6','w','2*pi*f'};

% Geometry
clear draw
g1=rect2(0,300e-6,0,10e-6);
g2=rect2(300e-6,500e-6,0,10e-6);
g3=rect2(500e-6,1000e-6,0,10e-6);
g4=rect2(1000e-6,1200e-6,0,10e-6);
draw.s.objs = {g1,g2,g3,g4};
fem.draw = draw;
fem.geom = geomcsg(fem);

% Create mapped quad mesh
MeshFactor = 30;
fem.mesh=meshmap(fem,'edgelem',{2,[3*MeshFactor],...
                               3,[3*MeshFactor],...
                               5,[2*MeshFactor],...
                               6,[2*MeshFactor],...
                               8,[5*MeshFactor],...
                               9,[5*MeshFactor],...
                               11,[2*MeshFactor],...
                               12,[2*MeshFactor]});

% Application mode 1
clear appl
appl.mode.class = 'Acoustics';
appl.assignsuffix = '_aco';
clear bnd
bnd.type = {'NA','SH','cont','IMP'};
bnd.nacc = {'-i*w^2*1e-9',0,0,0};
```

```
bnd.Z = {'0','0','0','343.4*1.161'};
bnd.ind = [1,2,2,3,2,2,3,2,2,3,2,2,4];
appl.bnd = bnd;
clear equ
equ.cs = {8490,1483,5640,343.4};
equ.rho = {2331,998.2,2230,1.161};
equ.ind = [1,2,3,4];
appl.equ = equ;
appl.var = {'freq','f'};
fem.appl{1} = appl;
fem.border = 1;
fem.units = 'SI';

% Solve problem
fem=multiphysics(fem);
fem.xmesh=meshextend(fem);
fem.sol=femlin(fem,'solcomp',{'p'}, ...
               'outcomp',{'p'});

% Plot cross-section along all domains
postcrossplot(fem,1,[0 0.0012;0 0], ...
    'lindata','p*exp(i*w*(0.6/f))', ...
    'axis',[0 1200e-6]);
```

COMSOL

Appendix C

COMSOL-script; The symmetric chamber model

This appendix contains the COMSOL-script use to obtain the numerical solution in Section 6.4. The script is compiled for COMSOL ver. 3.2

COMSOL

```
% Cleaning up
clc;close all;flclear fem

% Constants
k = 8;              %number of eigenvalues to be found
startF =2.2e6;      %where to start eigenvalue search
CorS = 1;           %0=circle-geom, 1=square-geom

% Geometry
g1=rect2('0.025','400e-6','base','center','pos',{'0','0'},'rot','0');
if CorS <=0.5
    g2=circ2('1e-3','base','center','pos',{'0','0'},'rot','0');
elseif CorS >= 0.49
    g2=square2('2e-3','base','center','pos',{'0','0'},'rot','0');
else
    k=1;
    disp('CorS - Error')
end
g3=geomcomp({g1,g2},'ns',{'g1','g2'},'sf','g1+g2','edge','none');
g4=geomdel(g3);
clear s
s.objs={g4};
s.name={'CO2'};
s.tags={'g4'};
fem.draw=struct('s',s);
fem.geom=geomcsg(fem);

% Initialize mesh
fem.mesh=meshinit(fem,'hmax',[50e-6]);

% Application mode 1
clear appl
appl.mode.class = 'Acoustics';
appl.assignsuffix = '_aco';
clear prop
prop.analysis='eigen';
```

```
appl.prop = prop;
clear bnd
bnd.type = {'SH','SS'};
if CorS <=0.5
    bnd.ind = [2,1,1,1,1,2,1,1,1,1];
elseif CorS >= 0.49
    bnd.ind = [2,1,1,1,1,1,1,1,1,1,1,2];
else
    k=1;
    disp('CorS - Error')
end
appl.bnd = bnd;
clear equ
equ.cs = 1483;
equ.rho = 998.2;
equ.ind = [1];
appl.equ = equ;
fem.appl{1} = appl;
fem.border = 1;
fem.units = 'SI';

% Solve problem
fem=multiphysics(fem);
fem.xmesh=meshextend(fem);
fem.sol=femeig(fem,'solcomp',{'p'}, ...
               'outcomp',{'p'}, ...
               'neigs',k, ...
               'shift',(2*pi*startF)^2); %Start search here

% Plot the found solutions
for i=1:k
    w=fem.sol.lambda(i);
    F = w^0.5/(2*pi);
    figure('position', [100, 100, 1201, 900])
    subplot('position', [0, 0, 1, 1])
    postplot(fem, ...
        'tridata',{'p','cont','internal'}, ...
        'trimap','jet(1024)', ...
        'tribar','off',...
        'tridlim',[-2,2], ...
        'solnum',i, ...
        'refine',3);
    axis off
    disp([i F])
end
```

COMSOL

Appendix D

COMSOL-script; Numeric Example 3

This appendix contains the COMSOL-script use to obtain the numerical solution in Section 7.3. The script is compiled for COMSOL ver. 3.2

COMSOL

```
% Cleaning up
close all,clear fem,flclear fem,flgc,clc

% GEOMETRY
L=0.001;
fem.geom = rect2(-L,L,-L,L)+point2(-L/6,-L/6);
fem.mesh = meshinit(fem);

% Mesh
sm=0.25e-4;
bm=sm;
fem.mesh=meshinit(fem,'hmaxedg',[1,bm,2,bm,3,bm,4,bm], ...
                  'hmaxsub',[1,sm]);

% Space dimension
fem.sdim = {'x' 'y'};

% Dependent variables
fem.dim = {'u' 'v' 'p'};
fem.shape = [2 2 1];

% Constants
fem.const = {'k','n*pi/L', ...
    'n','3', ...
    'c','1483', ...
    'th','0', ...                          %theta
    'r','3', ...
    'epss','w*l/c', ...
    'l','1e-9', ...
    'bl','2*L/n', ...
    'f','c/bl', ...
    'w','2*pi*f', ...
    'L',L, ...
    'rho','998.2', ...
    'ga','(beta+1)*w*eta/(2*rho*c^2)', ...  %gamma
    'beta','5/3', ...
```

```
    'eta','1e-3',...
    'uhat','-epss*c/(2*n*pi*gamma)'};

fem.expr = {
'sigmaxx' '-p+(beta+1)*eta*ux' ...
'sigmaxy' 'eta*(uy+beta*vx)' ...
'sigmayx' 'eta*(vx+beta*uy)' ...
'sigmayy' '-p+(beta+1)*eta*vy', ...
'S','(2*uhat^2*w*ga/(c^2))*(1+r^2-cos(2*k*x)-r^2*cos(2*k*y))', ...
'Fx1','(2*uhat^2*w*rho/c^2)', ...
'Fx2','(c*sin(2*k*x)+ga*r*w*y*sin(k*x)*sin(k*y)*sin(th))', ...
'Fx3','(r*cos(k*y)*(c*cos(th)*sin(k*x)+ga*(w*x*cos(k*x)-c*sin(k*x))*sin(th)))', ...
'Fx','Fx1*(Fx2+Fx3)', ...
'Fy1','(2*uhat^2*w*rho*r^2/c^2)', ...
'Fy2','(c*r*sin(2*k*y)-ga*w*x*sin(k*x)*sin(k*y)*sin(th))', ...
'Fy3','(cos(k*x)*(c*cos(th)*sin(k*y)+ga*(-w*y*cos(k*y)+c*sin(k*y))*sin(th)))', ...
'Fy','Fy1*(Fy2+Fy3)', ...
'tp1u1a','-2*ga*r*w*x*cos(k*x)*cos(k*y)*cos(th)',...
'tp1u1b','+ga*(c*sin(2*k*x)-2*w*(x+r*y*cos(th)*sin(k*x)*sin(k*y)))',...
'tp1u1','uhat^2*rho*(tp1u1a+tp1u1b+2*c*r*cos(k*y)*sin(k*x)*(ga*cos(th)+sin(th)))', ...
'tp1v1a','r*y*ga*w+w*x*ga*cos(th)*sin(k*x)*sin(k*y)-1/2*c*r*ga*sin(2*k*y)', ...
'tp1v1b','cos(k*x)*(w*y*ga*cos(k*y)*cos(th)+c*sin(k*y)*(-ga*cos(theta)+sin(th)))', ...
'tp1v1','-2*uhat^2*r*rho*(tp1v1a+tp1v1b)', ...
'J2X','rho*u+tp1u1/c^2', ...
'J2Y','rho*v+tp1v1/c^2'
};

% Governing equations
fem.form = 'general';
fem.equ.ga = {{{'sigmaxx' 'sigmaxy'} {'sigmayx' 'sigmayy'} {'0' '0'}}};
fem.equ.f = {{{'Fx'} {'Fy'} {'ux+vy-S'}}};

% Boundary conditions
fem.bnd.ind = {[1 4] [2 3]};
fem.bnd.r = {{{'J2X'} {'0'} {'0'}} {{'0'} {'J2Y'} {'0'}}};
fem.pnt.constr = {0,{0;0;'p'}};
fem.pnt.ind = [1,1,2,1,1];

% Solve problem
fem.xmesh = meshextend(fem);
fem.sol = femnlin(fem,'report','on');

% Plot solution
postplot(fem, ...
    'tridata',{'p','cont','internal'}, ...
    'trimap','jet(1024)', ...
    'refine',3);
```

COMSOL

Bibliography

[1] J. Lighthill, *Waves in Fluids* (Cambridge University Press, Cambridge, 2005), 3 edition.

[2] T. Duke and R. Austin, *'Microfabricated sieve for the continuous sorting of macromolecules'*, Physical Review Letters **80**, 1552 (1998).

[3] W. Yi-zhong and Z. Zhan, *'Biochip development and improvement based on electrophoresis separation'*, Instrument Techniques and Sensor 6–22 (2006).

[4] W. A. Mac Crehan, H. T. Rasmussen, and D. M. Northrop, *'Size-selective capillary electrophoresis (SSCE) separation of dna fragments'*, Journal of Liquid Chromatography **15**, 1063 (1992).

[5] B. Biscans and J. Bertrand, *'ELECTROPHORETIC SEPARATIONS - MODELLING OF THE TRANSIENT STATE OF THE BUFFER SOLUTION FLOW.'*, Chemical Engineering Research And Design **65**, 224 (1987).

[6] F. Aldaeus, Y. Lin, G. Amberg, and J. Roeraade, *'Multi-step dielectrophoresis for separation of particles'*, Journal of Chromatography A **1131**, 261 (2006).

[7] D. Chen, H. Du, and W. Li, *'Bioparticle separation and manipulation using dielectrophoresis'*, Sensors & Actuators: A. Physical **133**, 329 (2007).

[8] Y. Jing, L. R. Moore, P. S. Williams, J. J. Chalmers, S. S. Farag, B. Bolwell, and M. Zborowski, *'Blood progenitor cell separation from clinical leukapheresis product by magnetic nanoparticle binding and magnetophoresis'*, Biotechnology and Bioengineering **96**, 1139 (2007).

[9] N. Pamme and C. Wilhelm, *'Continuous sorting of magnetic cells via on-chip free-flow magnetophoresis'*, Lab on a Chip **6**, 974 (2006).

[10] L. King, *'Acoustic radiation pressure on circular discs: inertia and diffraction corrections'*, Proceedings of the Royal Society of London **153A** (1935).

[11] Y. K. K. Yosika, *'Acoustic Radiation Pressure On A Compressible Sphere'*, Acustica **5**, 167 (1955). Institute of Scientific and Industrial Research, Osaka University.

[12] A. Haake and J. Dual, *'Micro-manipulation of small particles by node position control of an ultrasonic standing wave'*, Ultrasonics **40**, 317 (2002).

[13] D.-H. Kim, A. Haake, Y. Sun, A. Neild, J.-E. Ihm, J. Dual, J. Hubbell, B.-K. Ju, and B. Nelson, *'High-throughput cell manipulation using ultrasound fields'*, Engineering in Medicine and Biology Society, 2004. EMBC 2004. Conference Proceedings. 26th Annual International Conference of the **1**, 2571 (2004).

[14] L. A. Kuznetsova and W. T. Coakley, *'Microparticle concentration in short path length ultrasonic resonators: Roles of radiation pressure and acoustic streaming'*, Journal of the Acoustical Society of America **116**, 1956 (2004).

[15] K. Yasuda, S.-I. Umemura, and K. Takeda, *'Concentration and fractionation of small particles in liquid by ultrasound'*, Japanese Journal of Applied Physics, Part 1 (Regular Papers and Short Notes) **34**, 2715 (1995).

[16] A. Nilsson, F. Petersson, H. Jonsson, and T. Laurell, *'Acoustic control of suspended particles in micro fluidic chips'*, Lab on a Chip **4**, 131 (2004).

[17] H. Li and T. Kenny, *'High speed particles separation using ultrasound for microTAS and lab-on-a-chip application'*, Proceeding of the 26th Annual International Conference of the IEEE EMBS **3**, 2631 (2004).

[18] H. Jonsson, C. Holm, A. Nilsson, F. Petersson, P. Johnsson, and T. Laurell, *'Particle Separation Using Ultrasound Can Radically Reduce Embolic Load to Brain After Cardiac Surgery'*, The Annals of Thoracic Surgery **78**, 1572 (2004).

[19] A. Hatch, E. Garcia, and P. Yager, *'Diffusion-based analysis of molecular interactions in microfluidic devices'*, Proceedings of the IEEE **92**, 126 (2004).

[20] F. Bottausci, C. Cardonne, C. Meinhart, and I. Mezic, *'An ultrashort mixing length micromixer: The shear superposition micromixer'*, Lab on a Chip **7**, 396 (2007).

[21] S.-Y. Jin, Y.-Z. Liu, W.-Z. Wang, Z.-M. Cao, and H. S. Koyama, *'Numerical evaluation of two-fluid mixing in a swirl micro-mixer'*, Journal of Hydrodynamics **18**, 542 (2006).

[22] C.-H. Lin, C.-H. Tsai, C.-W. Pan, and L.-M. Fu, *'Rapid circular microfluidic mixer utilizing unbalanced driving force'*, Biomedical Microdevices **9**, 43 (2007).

[23] S. Wang, H. Chen, C. Lee, C. Yu, and H. Chang, *'AC electro-osmotic mixing induced by non-contact external electrodes'*, Biosensors and Bioelectronics **22**, 563 (2006).

[24] C. Eckart, *'Vortices and streams caused by sound waves'*, Physical Review **73**, 68 (1948).

[25] J. Markham, *'Second order acoustic fields: streaming with viscosity and relaxation'*, Physical Review **86** (1952).

[26] W. Nyborg, *'Acoustic streaming due to attenuated plane waves'*, Journal of the Acoustical Society of America **25** (1953).

[27] http://www.smartbiomems.com.

[28] *Handbook of Chemistry and Physics Online* (CRC Press, 2006-2007), 87th edition. http://www.hbcpnetbase.com/

[29] *NIST - Data Gateway* (National Institute of Standards and Technology, 2004). http://srdata.nist.gov/gateway/

[30] C. Ishiyama and Y. Higo, *'Effects of humidity on Young's modulus in poly(methyl methacrylate)'*, Journal of Polymer Science, Part B: Polymer Physics **40**, 460 (2002).

[31] J. Markham, R. Beyer, and R. Lindsay, *'Absorption of sound in fluids'*, Reviews of Modern Physics **23** (1951).

[32] N. H. Asmar, *Partial Differential Equations with Fourier Series and Boundary Value Problems* (Pearson Prentice Hall, 2004), 2 edition.